Contribution to physico-chemical studies of squalenoylated nanomedicines for cancer treatment

Julie Mougin

université
PARIS-SACLAY

Contribution to physico-chemical studies of squalenoylated nanomedicines for cancer treatment

Thèse de doctorat de l'université Paris-Saclay

École doctorale n° 569, Innovation thérapeutique : du fondamental à l'appliqué (ITFA)
Spécialité de doctorat : Pharmacotechnie et Biopharmacie
Unité de recherche : Université Paris-Saclay, CNRS, Institut Galien Paris Sud, 92296, Châtenay-Malabry, France
Référent : Faculté de Pharmacie

Thèse présentée et soutenue à Châtenay-Malabry, le 28/02/2020, par

Julie MOUGIN

Composition du Jury

Elias FATTAL Professeur, Université Paris-Saclay (UMR8612)	Président
Luc LEBEAU Directeur de recherche, CNRS (UMR7199)	Rapporteur
Reiko ODA Directrice de recherche, CNRS (UMR5248)	Rapporteur
Claudie BOURGAUX Chargée de recherche, CNRS (UMR8612)	Examinatrice
Maria-Teresa PERACCHIA Global Head Drug Delivery and Product Integration, Sanofi	Examinatrice
Clément SANCHEZ Professeur, Collège de France (UMR7574)	Examinateur
Patrick COUVREUR Professeur, Université Paris-Saclay (UMR8612)	Directeur de thèse

Remerciements

Je souhaite tout d'abord remercier les membres de mon jury d'avoir accepté d'évaluer mon travail de thèse. Merci au Dr. Reiko Oda et au Dr. Luc Lebeau d'avoir accepté d'en être les rapporteurs, et merci au Dr. Claudie Bourgaux, au Dr. Maria-Teresa Peracchia, au Pr. Elias Fattal ainsi qu'au Pr. Clément Sanchez d'avoir accepté de participer en qualité d'examinateurs.

Je tiens à remercier Patrick pour son accueil au sein de l'équipe il y a déjà 9 ans, pour m'avoir poussée à faire une thèse, et l'avoir dirigée. Merci également pour votre bonne humeur et votre optimisme à toute épreuve.

Merci à nouveau à Elias pour ton accueil au sein du laboratoire, ainsi que ton soutien quotidien.

Je souhaite ensuite remercier Claudie, pour ta gentillesse et ton importante aide sur ce travail, particulièrement pour les longues heures de SAXS (notamment la session nocturne à Grenoble). Merci à Christophe et Semen pour la modélisation moléculaire et la bonne humeur franc-comtoise, me rappelant mes racines. Merci à David, Jean-Philippe, Nicolas H. et Fanny S. pour avoir tenté de décrypter avec moi les secrets de cette molécule capricieuse. Les résultats obtenus n'ont pas souvent été ceux attendus mais ce travail n'en serait pas arrivé là sans votre patience, bien plus développée que la mienne. Merci également à Sylvain, Ghislaine, Cynthia et Claire, les spécialistes de la microscopie en transmission pour les 60 Go de photos de nanoparticules accumulés au cours de ces dernières années. Bien qu'elles aient souvent amené plus de questions que de réponses, leur rôle a été fondamental. Je remercie également Didier et Arnaud pour le « recyclage » de la SQ-Dox, ainsi que la RMN. Enfin, merci à Barbara et Franco pour la synthèse de la SQ-Dox.

Un merci tout particulier à Simona et Nicolas T. pour votre disponibilité, les très, très nombreux conseils scientifiques, techniques, méthodologiques *etc.*, ainsi que l'écoute et le soutien psychologique que vous m'avez apportés durant cette thèse malgré vos emplois du temps chargés et l'encadrement de vos propres étudiants. Merci à Simona pour ta patience, le temps passé à améliorer

Sommaire

Discussion générale   113

Annexes   127

Abréviations

17-AAG	Tanespimycin
Ade	Adenosine
AFM	Atomic force microscopy
Ara-C	Cytarabine
BuSS	4-(pyridin-2-yl-disulfanyl)butyrate
CAC	Critical aggregation concentration
CaCl$_2$	Calcium chloride
CDDP	Cisplatin
Ce6	Chlorin e6
CMC	Critical micellar concentration
CP	Cisplatin prodrug
CPT	Camptothecin
CPT-COOH	Carboxylic camptothecin
CPT-NH$_2$	Camptothecin-20(*S*)-glycinate
CRB	Chlorambucil
CTAB	Cetyltrimethylammonium bromide
CTC	Critical Transition Concentration
DEX	Dexamethasone
DiC$_8$PA	1,2-dioctanoyl-sn-glycero-3-phosphatidyladenosine
DLPA	1,2-dilauroyl-sn-glycero-3-phosphatidyladenosine

DLPU	1,2-dilauroyl-sn-glycero-3-phosphatidyluridine
DMF	*N,N*-dimethylformamide
DOPE	1,2-dioleoyl-sn-glycero-3-phosphoethanolamine
DOX	Doxorubicin
DPLL	Dendritic polylysine
Eto	Etoposide
FA	Folic acid
Glu	Glucosamine
GSH	Glutathione
HCPT	10-hydroxy camptothecin
Ket	Ketoprofene
LA-Ara	Lauric acid-cytarabine
lPEI	Linear poly(ethylene imine)
MMP-2	Matrix metalloproteinase-2
MRI	Magnetic resonance imaging
MTX	Methotrexate
NaCl	Sodium chloride
NaSal	Sodium salicylate
Nb	Nabumethone
NP	Nanoparticle

OA-Ara	Oleic acid-cytarabine
P18	Purpurin18
PA-Ara	Palmitic acid-cytarabine
PAm	Paptide amphiphile
PBCL	Poly(alpha-benzyl carboxylate epsilon-caprolactone)
PCL	Poly(caprolactone)
PDLLA	Poly(DL-lactide)
PDPA	Poly(2-diisopropyl methacrylate)
PEG	Poly(ethylene glycol)
PGA	Poly(glycolide)
PHB	Poly([(R)-3-hydroxybutyrate]
PISA	Polymerization-induced self-assembly
PKA	Protein kinase A
PLA	Poly(lactide)
PLLA	Poly(L-lactide)
POEGMA-*b*-P(ST-*co*-VBA)	Poly[oligo(ethyleneglycol)methacrylate]-*block*-[poly(styrene)-*co*-poly(vinyl benzaldehyde)]
PTX	Paclitaxel
Rap	Rapamycin
SA	Succinic acid
SCB	Succinobucol
SEM	Scanning electron microscopy
SN-38	7-ethyl-10-hydroxycamptohecin
SPIO	Small Particles of Iron Oxide
SQ-Ad	Squalenoyl-adenosine

Abréviations

SQ-Dox   Squalenoyl-doxorubicin

TA   Triamcinolone acetonide

TEM   Transmission electron microscopy

TTZ   Trastazumab

Uri   Uridine

WLM   Worm-like micelles

YSV   Tyroservatide

Introduction générale

La « squalénisation » est une stratégie de transport et de vectorisation de médicaments développée dans l'équipe du Pr. Couvreur dès l'année 2006. Cette approche consiste à coupler chimiquement le squalène, un lipide biocompatible, à une molécule active. Le bioconjugué ainsi formé est alors capable de s'auto-assembler spontanément sous forme de nanoparticules dans l'eau. Celles-ci présentent généralement une forme sphérique. De manière inattendue, dans le cas des nanoparticules de doxorubicine-squalène, une forme allongée, de type "boucle-train" a été observée. L'objectif de ce travail de thèse était de comprendre le mécanisme de formation de ces structures particulières et d'en réaliser la caractérisation physico-chimique.

Ce manuscrit se divise en deux parties : le premier chapitre est une étude bibliographique dont la première partie décrit les principes de l'auto-assemblage, ainsi que les propriétés de visco-élasticité, de molécules amphiphiles sous forme de micelles cylindriques, également appelés micelles "worm-like". La seconde partie présente les principaux systèmes cylindriques auto-assemblés appliqués à la délivrance de principes actifs.

Le second chapitre de ce manuscrit correspond à la partie expérimentale de la thèse et détaille les résultats expérimentaux obtenus. Les nanoparticules de doxorubicine-squalène ont été caractérisées principalement par des techniques de microscopie électronique et de diffraction des rayons X. Les résultats obtenus ont été soutenus par des études de modélisation moléculaire. Ces travaux soulignent, entre autres, le rôle des propriétés d'empilement de la doxorubicine dans la formation des nanoparticules allongées. Ils révèlent également l'influence de la nature des sels ajoutés sur la forme des nanoparticules de doxorubicine-squalène.

Enfin, une discussion générale des résultats obtenus et un exposé des difficultés expérimentales rencontrées viennent compléter ce manuscrit. Les perspectives d'avenir de ce travail sont également discutées.

General introduction

The "Squalenoylation" is a novel drug delivery approach developed by Pr. Couvreur's team since 2006. It consists in the chemical conjugation of the squalene, a biocompatible lipid, to a pharmacologically active molecule. The resulting bioconjugate displays the unique ability to self-assemble into nanoparticles in water. Generally, the obtained nanoparticles exhibit a spherical shape. Interestingly, the squalenoyl-doxorubicin nanoparticles were characterized by an unusual elongated « loop-train » structure. The aim of this thesis was to elucidate the mechanism of formation of such structures, based on a deep physico-chemical characterization.

The manuscript is divided in two parts: the first chapter is a bibliographic review. It discusses the basics about the self-assembly of amphiphilic molecules into cylindrical micelles, also called "worm-like" micelles. It also describes their viscoelastic properties. The main self-assembled cylindrical nanosystems applied to drug delivery are also discussed.

The second chapter of the manuscript shows the experimental results obtained during the thesis. The squalenoyl-doxorubicin nanoparticles have been characterized mainly by electronic microscopy and X-ray scattering techniques. Those findings were supported by molecular dynamics simulations. The study has also highlighted the role of the π-π stacking properties of the doxorubicin moiety in the formation of the elongated nanoparticles. It also reveals the influence of the nature of the added salts on the shape of the squalenoyl-doxorubicin nanoparticles.

The manuscript concludes with a discussion of the main results obtained and the experimental difficulties are also explained. Some perspectives resulting from this study are also suggested.

Chapitre 1 : Revue bibliographique

Cylindrical self-assembled drug delivery devices: from molecular organization to therapeutic applications

Abstract

Self-assembled cylindrical aggregates made of amphiphilic molecules emerged almost 40 years ago. Due to their length up to micrometers, those particles displayed particular physico-chemical properties, such as important flexibility and high viscoelasticity, making them suitable for a wide range of industrial applications. However, a quarter of century was needed to successfully take advantage of those improvements towards therapeutic purposes. Since then, a wide diversity of biocompatible materials such as polymers, lipids or peptides, have been developed to design self-assembling elongated drug nanocarriers, suitable for therapeutic or diagnostic applications. More recently, the understanding of the main forces driving the unidirectional growth of these nanodevices allowed a translation toward the formation of pure nanodrugs to avoid the use of unnecessary side materials and the possible toxicity concerns associated.

I. Introduction

Cylindrical nanoparticles (NPs) are known under various appellations such as giant micelles, filomicelles, worm-like NPs, rod-like NPs *etc*. First evidenced in 1981 by Porte *et al.* in a solution of cetylpyridinium bromide[1], their formation and properties have been widely investigated since then. Such aggregates are the results of the self-assembly of amphiphilic compounds in aqueous media, depending on specific conditions, like the geometry of the surfactant molecules or their volume fraction in the suspension, but also the temperature, ionic strength *etc*.[2] The length of these elongated nano-objects can reach up to several micrometers, conferring them high flexibility and favoring their entanglement above critical concentration. The combination of these two properties resulted in the emergence of interesting viscoelastic properties, successfully exploited in industrial fields like oil recovery[3] or fracturing fluids[4] for example. However, it took about 25 years for those giant elongated NPs to unveil their potential as new drug delivery systems. The pioneering research initiated by Discher's group about biodegradable polymeric filomicelles highlighted impressive improvements over conventional spherical carriers like micelles, liposomes or vesicles[5,6], particularly towards cancer treatment. This new generation of nanocarriers allowed sustained blood circulation, improved biodistribution and pharmacokinetics. Those progresses have paved the way for the development, over the last decade, of a wide range of nanomaterials from drug loaded into elongated nanocarriers to pure drug forming itself the cylindrical nanomedicine.

The first section of this review will discuss the main principles concerning the self-assembly of elongated nanostructures and their physico-chemical properties, while the second part will give an overview of the recent applications and developments of cylindrical drug delivery NPs.

II. Basics of self-assembly and physico-chemical properties of worm-like micelles

1. Self-assembly mechanisms

1.1. Dilute regime

The dilute regime is generally related to solutions with surfactant concentrations below 0.1 %wt.[7] At high dilution, the number of amphiphilic molecules is much lower than the number of water molecules and the electrostatic interactions between amphiphilic molecules in water are very weak. Since their aggregation is an entropically unfavorable process, they remain in a monomeric form in solution.[8] When the concentration increases and gets closer to the solubility limit, attractive interactions between hydrophobic moieties appear, triggering the formation of aggregates. The specific concentration at which this association starts is called the critical micellar concentration (CMC). The micelle is structured by a compact liquid-like core made of the surfactant hydrophobic tails while the polar headgroups form a shell.[9] The whole system is maintained by weak non-covalent interactions, of the order of $k_B T$ per molecule. The number N of molecules into a micelle is called the aggregation number. At the CMC, its range of order is generally of 30-100 molecules. However, a minimal aggregation number N_m exists such as the formation of micelles of size $N < N_m$ is improbable. Consequently, surfactant molecules will exist either as monomers, or as components of a micelle of size $N \geq N_m$.[8,9] Moreover, the self-assembly of surfactant in water is a reversible process. Micelles are dynamic structures that constantly break and recombine, so monomers and micelles coexist in equilibrium.

The structures formed by the aggregation of surfactant molecules are the result of two opposite forces. The hydrophobic tails are subjected to attractive interactions in order to avoid the contact with water. Oppositely, the hydrophilic headgroups undergo repulsive interactions to maximize the contact with water, increasing the interfacial area per molecule.[8,9] The equilibrium between those two effects is influenced by the surfactant properties (charge, geometry,

hydrophilic/lipophilic ratio…) but also by the medium (temperature, ionic strength…). All those considerations are described by the packing parameter p defined following:

$$p = v/a_0 l_c \qquad (1)$$

where v is the amphiphile molecular volume, a_0 the optimal headgroup area at the interface and l_c the maximum chain length (**Figure 1**).[8]
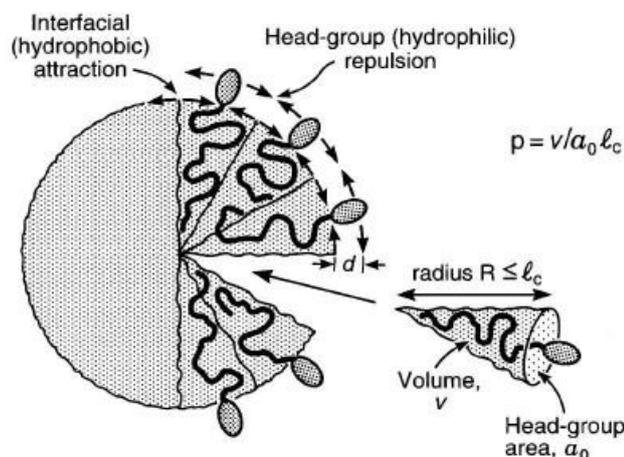
Figure 1: The surface and bulk intermolecular interactions that define the dimensionless packing parameter or average molecular 'shape factor' $v/a_0 l_c$ of amphiphiles.[8]

The packing parameter also describes the preferred shape for amphiphilic aggregates. For example, $p \leq 1/3$ is indicative of spherical micelles, while $p \approx 1/2$ is obtained in the case of cylindrical micelles. When $p > 1$, inverse structures are formed (**Figure 2**).
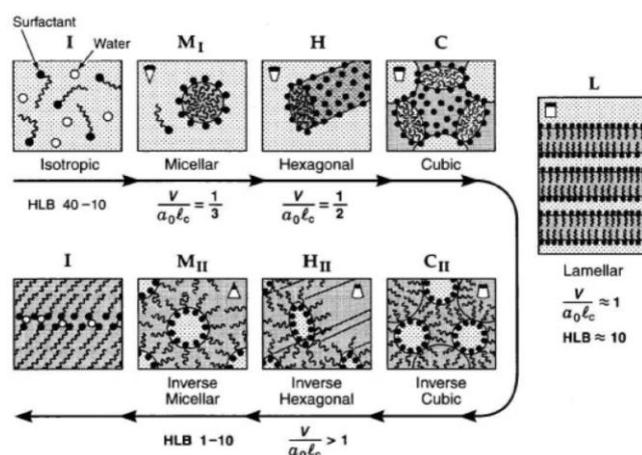
Figure 2: Generic progression of structures with increasing packing parameter (decreasing the Hydrophilic Lipophilic Balance value). Subscripts II refer to inverted structures.[8]

Interestingly, as the spherical shape is the one requiring the lowest energy, most of the amphiphiles whose packing parameter should correspond to a preferential aggregation as cylinders first assemble as spheres. Above the CMC, the further addition of amphiphiles results in an increase of the number of spherical micelles. However, at some point, the excess monomers starts incorporating into the micelle body, triggering their progressive elongation. During their growth, the cylinders preserve at their ends the hemi-spherical structures remaining from the initial spherical micelle. This transition is called the sphere-to-rod transition and is a discontinuous process, occurring when overcoming a so-called "Critical Transition Concentration" or "second CMC". This sphere-to-rod transition initiates in the different packing properties of the cylindrical body and the hemispherical endcaps of the micelles. In the micelle body, the cylindrical shape requires a low packing energy and prevents the contact between the hydrophobic chains and water. At the same time, the aggregate is submitted to repulsive interactions between the two endcaps. As a result, short cylinders micelles appear unfavorable and disappear in solution in favor of spherical micelles and long cylindrical micelles, usually called worm-like micelles (WLM).[9] The first experimental evidences of this sphere-to-rod transition have been reported by Porte *et al.* in the early 1980s with cetylpyridinium-based systems[1] and has been further extensively studied.[10–13]

In addition to the amphiphile concentration, the second CMC is dependent on several parameters. Any factor having repercussions on surfactant properties like pH, temperature *etc,* might

trigger micellar growth. In the case of ionic amphiphiles, the modification of the ionic strength evidently strongly favors this process. Indeed, the addition of counterions screens the electrostatic repulsions between polar headgroups. Consequently, the molecular area decreases and the endcap energy increases, promoting the micelles elongation.[2] This has repercussions on the packing parameter: the decrease in the molecular area results in an increase of the packing parameter from values compatible with spheres towards values in agreement with cylinders formation. The nature of the counterion plays also a role. Hydrotropic counterions like aromatic derivatives as sodium salicylate act by inserting between the headgroups, thus penetrating into the micelles.[7] But co-surfactant like short-chain alcohols can also be used.

Once the second CMC is overcome, the progressive increase of the surfactant volume fraction results in the unidirectional growth of the micelles, rather than in the formation of new ones, in an attempt to minimize the number of energetically unfavorable endcaps in the system.[8,9,14] During this process, the micelles radius generally remains constant. Short cylindrical micelles are rigid systems qualified as "rod-like micelles". Their rigidity can be described by the persistence length l_p, defined by:

$$l_p = w/k_B T \tag{2}$$

where w is the bending modulus of the micelles.[15] Usually, in the case of neutral WLM, $l_p \approx$ 400 Å and higher for charged WLM.[7] When the micelles length L is close to l_p, they can be considered as semi-flexible. And when L exceeds l_p, the micelles behave like flexible polymers.[16] In the dilute regime, the mean chain length $\overline{L}$ of neutral or highly screened micelles can be determined following:

$$\overline{L} = \Phi^{1/2} \exp [E_{sc}/2k_B T] \tag{3}$$

where Φ is the surfactant volume fraction and E_{sc} is the scission energy (energy required to form two hemispherical chain ends). For charged or highly screened micelles, E_{sc} is completed by an additional electrostatic contribution E_e, corresponding to the repulsive energy between two endcaps acting in favor of micelles shortening.[2,14,15]

An alternative way to minimize the excess endcap energy in the system is the closure of WLM into rings. But this phenomenon is uncommon as it can only occur in very specific conditions. The surfactant must generally be highly diluted and it only applies to medium micellar lengths. Due to their rigidity, the energy required to bend short rods would be prohibitively high. Oppositely, ring formation from long WLM would cause a considerable loss of configurational entropy.[9,17] Only very few systems are able to spontaneously assemble into rings as the dominant population. The first experimental evidence was reported by In *et al.* in 1999, using a cationic surfactant tetramer derived from the dodecyltrimethylammonium bromide.[18] Since, block copolymer systems have also been developed, based on polystyrene coupled to poly(vinylpyridine) or poly(acrylic acid).[19–21]

At high surfactant concentration, the endcap energy may also be lowered thanks to the formation of junctions between micelles. Even though energetically unfavorable, the increase of inter-micellar interactions with surfactant volume fraction helps the occurrence of such fusions between a micelle endcap and another one body. Interestingly, according to Cates' work, those junctions present the ability to slide along the WLM body.[22] In the case of nonionic WLM, this particular events may be promoted by a temperature rise.[23]

When the micelles length exceeds the intermicellar length, they overlap and entangle to progressively form a dense and transient network. The concentration at which this event starts is the overlapping concentration C*. The nature of the counterion and the temperature can affect C*.[14] This marks the transition from a dilute towards a semidilute regime.[16,17,22]

1.2. Semidilute regime

The semidilute regime relates to systems with amphiphile concentrations generally comprised in the 0.1-10 %wt range.[7] In such systems, the range of electrostatic interactions become smaller than the micelles size. Their growth accelerates with the increase of surfactant concentration, until they entangle to form networks. The presence of very long and flexible chains forming a multi-connected structures confers gel-like behavior to the networks.[16,23] In the semidilute regime, few large

rings might appear in solution as the result of the fragmentation of very long chains existing at low concentration. However, they remain rare as high persistence length would inhibit their closure. Assuming that no rings are present in solution, the mean chain length can be expressed as:

$$\overline{L} = \Phi^{0,6} \exp [E_{sc}/2k_B T] \qquad (4)$$

High scission energy results in an increase of the overlapping. Above a specific concentration, the network mesh size overcomes the micelles persistence length. This marks the transition point from the semidilute to the concentrated regime (Onsager domain).[23]

1.3. Concentrated regime

In the concentrated regime, generally for surfactant volume fractions above 10%, the formed networks are dense due to strong inter-micellar interactions. In this state, the mesh size is of the same range than the persistence length of WLM and micellar growth is weakly dependent on the surfactant concentration.[7]

At very high surfactant concentration, generally around 20-50%, a transition from a disordered isotropic phase towards an ordered nematic phase occurs (I-N transition). In this state, the micelles become nearly parallel and their length is drastically higher than in the isotropic phase, nearly infinite, due to the coupling of inter- and intra-micellar interactions.[9,24]

2. Viscoelastic properties of worm-like micelles

2.1. Zero-shear viscosity

Diluted systems behave like Newtonian fluids. They exhibit a very low viscosity, typical of micellar solutions, independently of the shear rate applied. As the micelles length increases, the system enters the semidilute regime. Growth and entanglement of worm-like micelles result in a drastic rise of the zero-shear viscosity η_0. This phenomenon expresses in a more important way for

cationic micelles than for anionic or nonionic ones.[14] Consequently, the sphere-to-rod transition can be experimentally evidenced by monitoring the solution viscosity depending either on the surfactant concentration (in the case of surfactant able to form worm-like micelles without any additive), the salt concentration or the ratio of both.[25–27] The maximum viscosity corresponds to the formation of the most rigid micelles. After this point, some systems present a new viscosity decrease. This has been attributed to the presence of branching points. As they are free to slide along the cylindrical micelles bodies, the relaxation of the shear-induced stress is facilitated, hence the viscosity decrease.[28,29] Clausen *et al.* have investigated the rheological behavior of a classical system composed of cetyltrimethylammonium chloride with varying amounts of sodium salicylate (NaSal) as the counterion in a sodium chloride (NaCl) solution to increase the ionic strength.[26] Later, this study was extended to a wider range of cationic surfactants with the same C_{16} tail. This helped to define the general trend for the zero-shear viscosity depending on the molar ratio of the salt to the surfactant $R = C_{salt} / C_{surf}$ (**Figure 3**). By analogy with the previously described solution of surfactant in water, characteristic values of R can be defined. For example, R_c corresponds here to the critical molar ratio at which the system enters the semi-dilute regime and the sphere-to-rod transition starts. With the increase of the amount of salt, the micelles keep growing up to the entanglement point, corresponding to the overlap ratio R^*. At R_{max}, the WLM form a dense network and further addition of salts will screen the intermicellar repulsions, allowing the apparition of branching points. As such contact points may slide along the cylinders body, the viscosity will decrease before increasing again once the equimolar ratio R_{eq} is overcome. However, the mechanism for this second viscosity rise has not been elucidated yet.[27]
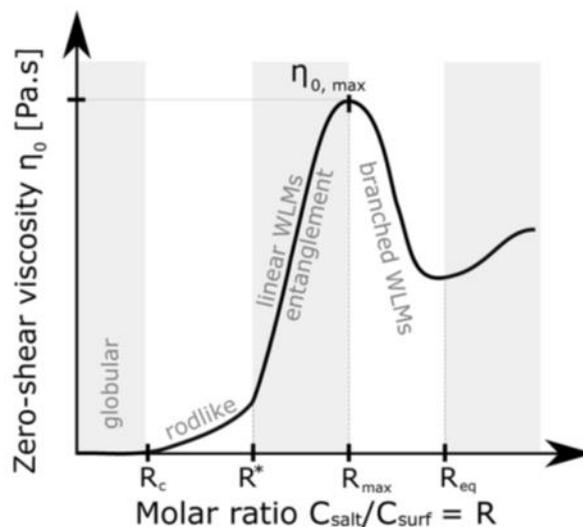
Figure 3: Schematic representation of the variation of zero-shear viscosity η_0 and morphology as a function of salt addition, that is, molar ratio R, while the surfactant concentration is maintained. Adapted from [27]

Recently, Pleines *et al.* have developed a thermodynamic model able to predict the position and amplitude of the viscosity peak for charged surfactant depending on the addition of electrolytes or hydrophobic solutes.[30] This model relies on the geometrical features of the surfactant molecules and principles of polymer physics and could constitute a new helpful screening tool for formulation optimization.

2.2. Stress relaxation mechanisms of entangled worm-like micelles

Worm-like aggregates are characterized by interesting viscoelastic properties. They usually can be described by the Maxwell model, consisting in the assimilation of the assemblies to a spring with elastic modulus G_0 coupled to a damper of viscosity η_0. When submitted to an external force, the deformed worm-like chains have to relax stress. The main model describing this event is the reptation-reaction model.

The reptation mechanism has been first described by de Gennes in 1971 in the case of flexible polymeric chains.[31] It occurs in entangled systems and consists in the progressive escape of worm-like micelles from a surrounding fictional tube constituted of neighboring chains by curvilinear

diffusion along the micelle cylindrical body (**Figure 4**). τ_{rep} is the reptation time of a chain of length L, defined by:

$$\tau_{rep} = L^2/\pi^2 D_c \qquad (5)$$

where D_c is the curvilinear diffusion constant of a chain in its tube. The reptation rate is dependent on the number of cross-links: the more, the faster the reptation.[17,32,33]
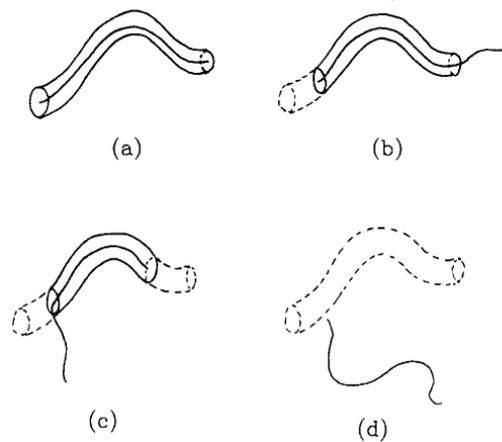
Figure 4: Reptation of a chain in its tube. The tube is defined at time t = 0 (a). Curvilinear diffusion causes parts of the tube to be lots (b, c); the new tube that is formed (not drawn) is in equilibrium and does not support stress. At $t \geq \tau_{rep}$, none of the original tube remains.[34]

Worm-like micelles are dynamic systems that constantly break and recombine, hence their comparison to "living polymers". The corresponding characteristic breaking time τ_{break} corresponds to the lifetime of a chain of length L before its spontaneous breaking into two new chains and is defined as follows:

$$\tau_{break} = 1/(kL) \qquad (6)$$

where k is the reaction rate. This process is independent of the micellar volume fraction.

The opposite reaction to chain scission is recombination. The time scale is equivalent for those two events. Consequently, recombination characteristic time is also τ_{break}.

If reversible scission is the main process for chain breaking, alternative mechanisms can be

encountered **(Figure 5)**:[22,35]

- end interchange: a reactive chain end interacts with the body of another micelle, resulting in an immediate rearrangement of the two chains involved,

- bond interchange: two entangled micellar chains fuse and split into two new chains, different from the initial ones.

a.   **b.**
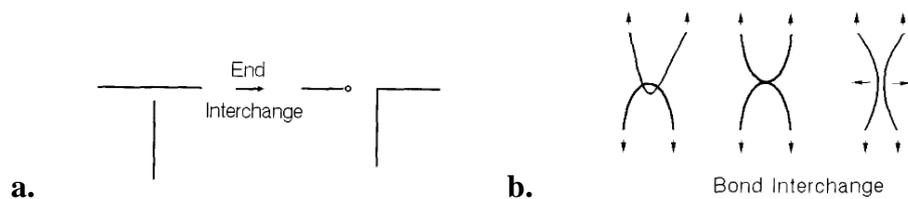
Figure 5: a. End interchange mechanism **b.** Bond interchange mechanism. The black lines represent the micelles body, open circles represent reactive chain ends.[35]

In addition to reptation and reversible breaking, the stress relaxation can occur through other less frequent processes:

- the breathing of micelles chains leading to fluctuations of its tube length,

- the appearance of Rouse-like modes, dominant relaxation mode for micellar chains shorter than the system entanglement length (distance between two entanglement points).[34,36]

Depending on the respective time scale of reptation and reversible scission processes, two different behaviors may be described for worm-like systems. When $\tau_{break} \gg \tau_{rep}$, the relaxation mechanisms do not involve the breaking of micelles chains. Consequently, they can be assimilated to reptating "dead" polymer chains. Oppositely, when $\tau_{break} \ll \tau_{rep}$, stress relaxation is driven by a competition between reptation and chain breaking. In that case, the terminal time τ for stress relaxation mays be defined as:[17,32,34]

$$\tau = (\tau_{break}\tau_{rep})^{1/2} \tag{7}$$

This stress relaxation time describes the viscoelastic behavior of worm-like micelles, as it will be described in the next part.

2.3. Linear rheology of worm-like micelles

As previously said, worm-like micelles display viscoelasticity properties. In the linear regime, they only depend on the timescale of experiments. When submitted to shear, worm-like micelles stress relaxation can be described by the stress relaxation function G(t) described by the relation:

$$G(t) = G_0 \exp(-t/\tau) \tag{8}$$

where G_0 is the elastic modulus at t = 0.[35] The Fourier transform of G(t) is the dynamical elastic moduli $G^*(\omega)$ described as:

$$G^*(\omega) = G'(\omega) + iG''(\omega) \tag{9}$$

where ω is the angular frequency. $G'(\omega)$ and $G''(\omega)$ represent the storage and the elastic moduli, respectively, and are defined by the expressions:[37]

$$G'(\omega) = G_0 \frac{\omega^2\tau^2}{1+\omega^2\tau^2} \text{ and } G''(\omega) = G_0 \frac{\omega\tau}{1+\omega^2\tau^2} \tag{10}$$

The relaxation time τ can be obtained knowing G_0 and η_0:

$$\tau = \eta_0 / G_0 \tag{11}$$

Typical curves of G' and G'' against the angular frequency are plotted in **Figure 6a**, for a mixture of cetyltrimethylammonium bromide (CTAB) and NaSal, depending on the temperature.[38] It shows that worm-like micelles exhibit a more viscous behavior at low frequencies and an elastic one at high frequencies. The extrapolation of the plateau for G' gives a value for G_0, while the G'' curve goes through a minimum G''_{min} at high oscillation frequencies. Those two parameters can be related to the length L of the micelles using:

$$\frac{G_0}{G'_{min}} \approx \frac{L}{l_e} \tag{12}$$

where l_e is the entanglement length, *i.e.* the length between adjacent entanglement sites. Consequently, Zhao *et al.* demonstrated that a raise of the temperature caused a decrease of the length

of CTAB micelles.[38] Also, the frequency corresponding to the crossing point between G' and G''

curves can be used to calculate the relaxation time following the equation[7]:

$$\tau = 1 / \omega \qquad (12)$$

To confirm the fitting between the experiment and the Maxwell model, G'' can be plotted as

a function of G' in a Cole-Cole plot (**Figure 6b**). For a Maxwell fluid with monoexponentital stress

relaxation, the experimental data is expected to fit a semicircle described by the following function[39]:

$$\left(G' - \frac{G_0}{2}\right)^2 + G''^2 = \frac{G_0^2}{4} \qquad (13)$$

However, deviations may appear for high frequencies, resulting in a separation of the

experimental and calculated curves for high G' values, as a consequence of a possible crossover

between the reptation-reaction mode and breathing or Rouse-like modes. The height of the dip is

proportional to the number of entanglements.[39] The deviations from the Maxwell model mark the

transition from linear to nonlinear rheological responses.
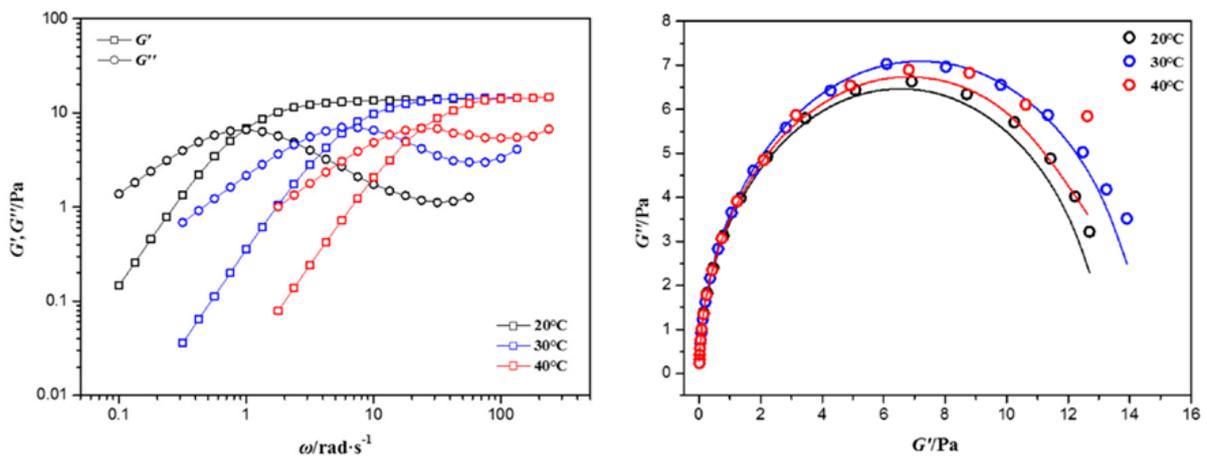
Figure 6: a. Linear viscoelastic spectrum and **b.** Cole-Cole plot of CTAB / NaSal worm-like micelles. Adapted from [38]

2.4. Nonlinear rheology of worm-like micelles

Spenley *et al.* have been the first to demonstrate that irregularities of the flow can appear above a critical shear rate for cetylpyridinium chloride/sodium salicylate worm-like micelles.[40] As a result, the system undergoes a phase separation into different macroscopic layers exhibiting different viscosities and shear rates. This event is known as shear-banding and is the main feature of the nonlinear rheology of worm-like micelles. It has been observed for worm-like micelles in the concentrated regime, slightly below the limit between isotropic and nematic phases.[7,41] At low shear rates, the shear stress increases before reaching a plateau. This point marks the beginning of the phase transition and the two phases coexist. Above a second critical shear rates, the isotropic phase disappears in favor of the nematic one and the flow becomes homogeneous again **(Figure 7)**.[42]
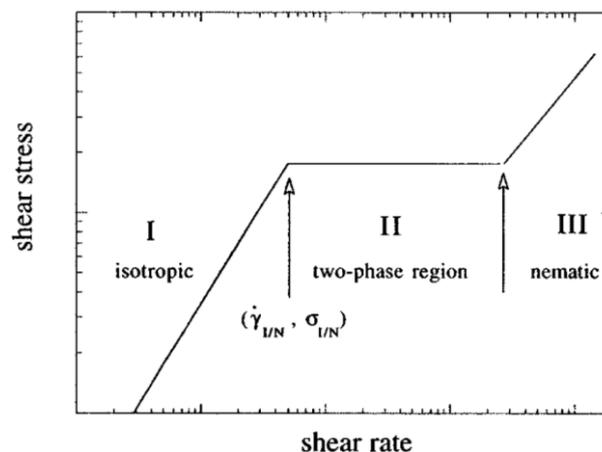
Figure 7: Schematical flow curves for worm-like micelles as obtained from mechanical-rate controlled experiments.[42]

III. Filamentous drug delivery devices

1. General properties of cylindrical nanomedicines

Cylindrical nanomedicines have raised growing interest in the drug delivery field over the last fifteen years. Discher's group paved the way by developing the first polymeric filomicelles in the mid 2000's, showing their improved therapeutic potential over their spherical counterparts.[5,6]

Following this, Mitragotri and co-workers started to investigate and to discuss about the i*n vivo* fate of nanocarriers depending on parameters such as shape, size and surface chemistry.[43,44] Cylindrical drug nanocarriers generally display diameters below 100 nm and lengths of few hundred nanometers to micrometers **(Table 1).** If the shape and diameter of such nanoassemblies could be easily determined by the means of microscopy techniques such as transmission or scanning electron microscopy (TEM or SEM, respectively) or atomic force microscopy (AFM), precise length determination remains however difficult to achieve, due to possible entanglement of nanomedicines and/or dimensions exceeding those of the picture. Such dimensions were observed to increase the blood circulation time of the nanocarriers in rodents, favoring an increased tumor accumulation *in vivo* and an improved cellular uptake *in vitro*, leading to higher cytotoxicity **(Table 2)**. This stemmed from the enhanced surface area and higher margination propensity of micro-scale non spherical particles favoring adhesion to vessel walls compared to nano-scale spherical structures. The cellular uptake was also found to be impacted by the NPs morphology, as sharp geometries at the contact point favored internalization. Nevertheless, contradictory observations may sometimes arise concerning the *in vivo* behavior of NPs with various shapes after intravenous administration, testifying of the complexity of those topics. A lot of reports have been published in an attempt to evidence general rules[45–48] yet, few studies have attempted a direct comparison of therapeutic performances between self-assembled cylindrical nanomedicines and spherical ones. One of the reasons could be the difficulty to generate different shapes based on a unique chemical composition. But in some cases, shape could be successfully tuned bringing external energy to the samples, like heating[49], high pressure[50] or ultrasonication[5], for example. And recent studies confirmed the higher cellular uptake and improved cytotoxicity of cylindrical nanomedicines in various cancer cell lines. However, no general trend still emerges as for the drug release mechanism too.

Table 1: Dimensions of the main cylindrical drug delivery systems

System	Composition	Drug	Diameter (nm)	Length (µm)	Technique	References
Polymers	PEG-PCL	PTX	20-60	2-18	(Cryo-)TEM, Fluorescence microscopy	[5,6,51]
	PEG-PCL (silica-coated)	MTX	121	~ 1	FE-SEM	[52]
	PEG-P(CL/GA)*	PTX	20	0.1-1	TEM	[51]
	PEG-PBCL	PTX		23	Fluorescence microscopy	[53]
	PGA-g-(PCL-b-PEG)	DOX	n. d.	0.23	AFM	[54]
	mPEG-b-PDPA	SCB	19.9	50-200	TEM	[55]
	PEG-PLLA*	PTX	20	~ 0.2-> 1**	TEM, AFM	[56,57]
	PEG-PLLA*	PTX ± 17-AAG ± Rap	n. d.	> 1**	AFM	[58]
	PEG-PLA / PLA-Jeff-FA*	Betulin Derivative	n. d.	~ 0.1-1**	TEM	[59]
	Folate-PEG-PLA-PEG-Acrylate / MPEG-PLA-PEG-acrylate	DOX + SPIO	23	0.1-0.2	TEM	[60]
	LPEI-GT	DNA	53	128	AFM, TEM	[61]
	lPEI-g-PEG	DNA	~ 20-60	~ 0.06-1	TEM	[62]
	P(MeOx-b-BuOx-b-MeOx)	Eto ± CP	~ 50**	~ 100**	TEM	[63]
	PEG-b-PPS	ICG	50	> 1	Cryo-TEM	[64]
	PEG-PHB-PEG	ICG	5.4	> 1**	Cryo-TEM	[65]
	PEG-PHB-PEG / PF-127	ICG	5.25	~ 0.1-1**	Cryo-TEM	[65]
Peptide amphiphiles	$(C_{16}H_{32}O_2)_2$-K(VPGAG)$_3$	PTX	12-16	0.07-1.7	TEM, AFM	[66]
	qC8-Tat	PTX	15	> 1	TEM, WAXS	[67]
	KRRASVAGK[C$_{12}$]-NH$_2$	DOX	5.1	> 1	Cryo-TEM, SAXS	[68]
	C$_{16}$-A$_4$G$_3$E$_3$	CPT	11-12.4	> 1	TEM, SAXS	[69]
	C$_{16}$V$_2$A$_2$E$_2$G ApoA1 / C$_{16}$V$_2$A$_2$E$_2$-NH$_2$	GW3965	n. d.	0.3-> 1	Cryo-TEM	[70]
	CH$_3$(CH$_2$)$_{14}$CONH-GTAGLIGQRGDS-COOH	CDDP	8-10	> 1	TEM	[71]
Polymer-drug	PGMA-b-POEGMA-b-PSt	Gd^{3+}	30	Varying with time	TEM	[72]
	PEG-TetraCPT	CPT	60	0.5	TEM, Confocal microscopy	[73]
	PEG-OctaCPT	CPT	100	1		
Lipid-drug	DLPU	Uri	~ 4.2	> 2**	SANS, SLS	[74,75]

	DLPA	Ade	~10-12	~ 0.1-> 1**	Cryo-TEM, DLS	76
	OA-Ara	Ara-C	n. d.	0.2-> 1**	TEM	77
	LA-Ara	Ara-C	~ 30	> 2**	TEM	78
	PA-Ara	Ara-C	n. d.	> 1**	TEM	79
	SQ-Dox	DOX	~ 5-6	~ 0.006-> 1**	Cryo-TEM, AFM, SAXS	80
Peptide-drug	Ket-L-VEVE	Ket	50.44	> 1**	TEM	81
	mCPT-buSS-Tau / dCPT-buSS-Tau	CPT	6.7-7.2	> 1	(Cryo-)TEM	82
	CPT-PTX-Sup35	CPT / PTX	7-8	> 1**	Cryo-TEM	83
	P18-PLGVRGRGD	P18	30	> 1**	TEM	84
	HCPT-MDP26 Cylinders	HCPT	14	~ 0.04	TEM, SAXS	85
	HCPT-MDP26 Fibers		6.8	~ 0.04		
	HCPT-MDP26-PEG		8	~ 0.05		
	DOX-KGFRWR	DOX	10.5	> 1**	TEM	86
	PTX-Tau	PTX	11.8	> 1	Cryo-TEM, AFM	87
Supramolecular hydrogels	C16V2A2E2-Nb	Nb	7	> 0.1**	TEM, SAXS	88
	DEX-SA	DEX	30	> 1	TEM	89
	PTX-SA	PTX	10-15	> 1	TEM	90
	CRB-FFE-YSV	CRB / YSV	30-40	> 1	TEM	91
	PTX-SA-NapFFKYp	PTX	29	> 1**	TEM	92
Pure nanodrugs	CPT / TTZ / DOX		100.8	0.63	SEM	93
	CPT		100-400	4-24	SEM, AFM	94
	HCPT / Ce6		135	0.36	SEM, TEM	95
	CPT-NH$_2$		~ 100	> 1	SEM, TEM	96
	SN-38		50-300	1-10	SEM, TEM	97

* Dimensions of filomicelles formed in a mixture of spheres and cylinders

** Extrapolated from pictures

Jeff: Jeffamine (O,O'-Bis-(2-aminopropyl) poly(propylene glycol)-*b*-poly(ethylene glycol)-*b*-poly(propylene glycol)); MPEG: methoxy-PEG; LPEI: Low molecular weight PEI; GT: Gelatin; MeOx: 2-methyl-2-oxazoline; BuOx: 2-butyl-2-oxazoline; PPS: poly(propylene sulfide); PF-127: Pluronic F-127; RA: Retinoic acid; SCB: Succinobucol; 17-AAG: Tanespimycin; Rap: Rapamycin; Eto: Etoposide; ICG: Indocyanine Green; GW3965: Liver X Receptor agonist; FE-SEM: Field Emission Scanning Electron Microscopy; AFM: Atomic Force Microscopy; WAXS: Wide Angle X-Rays Scattering, SAXS: Small Angle X-Ray Scattering; SANS: Small Angle Neutron Scattering; SLS; Static Light Scattering; DLS: Dynamic Light Scattering.

Table 2: Anticancer properties of cylindrical nanocarriers compared to their spherical counterparts.

Cylinder composition	Sphere composition	Drug	IC50	Cell lines	Maximum tolerated dose	Other	References
PEG-PCL	PEG-PCL	PTX	~	A549	↗ x ~ 2	~ drug release rate in buffers in DPBS (pH 7.4) and DPBS:FBS 1:1 ~ tumor apoptosis ↘ nontumor organs apoptosis ↘ A549 tumor growth	[5,6,98,99]
PGA-*g*-(PCL-*b*-PEG)	PEG-PCL	DOX	↘ / 1.6	EJ	n. d.	↗ drug release over 110 h in PBS (pH 7.4) ↗ cell uptake by HeLa and HepG2 cells	[54]
PEG-PCL (silica-coated)	PEG-PCL (silica-coated)	MTX	↘ / 1.1	MCF-7	n. d.	↘ drug release rate over 160 h in PBS (pH 7.4)	[52]
PEG-TetraCPT/DOX	PEG-DiCPT/DOX	CPT	↘ / 2 ↘ / 1.7	MCF-7 MCF-7/ADR	n. d.	↗ blood circulation time ($t_{1/2}$ ↗ x 3.6) ↗ tumor accumulation	[100]
PEG-OctaCPT/DOX	PEG-DiCPT/DOX	CPT	↘ / 1.9 ↘ / 1.7	MCF-7 MCF-7/ADR	n. d.	~ blood circulation time	[100]
POEGMA-*b*-P(ST-*co*-VBA)/DOX Worms	POEGMA-*b*-P(ST-*co*-VBA)/DOX	DOX	↘ / 7.3 (Worms) ↘ / 2.8 (Rods)	MCF-7	n. d.	↗ cell uptake ~ drug release rate over 72 h in buffers (pH 5.0 and 7.4)	[101]
HCPT / C18PMH-PEG	HCPT / C18MPH-PEG	CPT	↘ / 2 ↘ 1.7 ↘ 1.4	KB 4T1 MCF-7	↘ / ~1.6	↘ drug release rate over 70 h in PBS (pH 7.4) ↗ and faster uptake by KB cells ↗ blood circulation time ~ accumulation in 4T1 tumor ↘ 4T1 tumor growth	[49,102]
MTX-PEG-CPT	MTX-PEG-CPT	MTX / CPT	↘ / 1.9	HeLa	n. d.	~ drug release over 48 h in PBS (pH 7.4) ↗ and faster uptake by HeLa cells ↗ blood circulation time ($t_{1/2}$ ↗ x 1.8) ↗ accumulation in HeLa tumor	[103]

↗: increase; ↘: decrease; ~: comparable

FBS: Fetal Bovine Serum

Since the emergence of cylindrical drug delivery systems, three main strategies were used for their design **(Fig 8)**. The classical one consisted in the formulation of a cylindrical nanocarrier, in which the drug is physically loaded. However, this approach may require purification step to remove the non-encapsulated drug, and often leads to poor drug loading and possible burst release of drug molecules only adsorbed onto the surface of the carrier. Additionally, the encapsulation of drugs into nanocarriers could trigger variations of the hydrophobic volumes and modify the supramolecular organization with possible loss of the cylindrical shape.[104] The covalent coupling of the drug directly to the nanocarrier material to form amphiphilic bioconjugates able to self-assemble in the appropriate media allowed to overcome some of the previous limitations. Depending on the molecular weight of the carrier molecule, such so-called "chemical encapsulation" allowed higher drug loadings, while avoiding burst release. Additionally, the incorporation of stimuli-sensitive linkers between the drug and the carrier material enables precise control of the drug release. However, both physical and chemical loading rely on the use of a carrier material which can have safety concern. Therefore, recent trends have focused on the development of carrier-free pure nanodrugs. However, such nanomedicines rely on the chemical properties of the drug and have for now been successfully applied only to a very limited number of drugs.
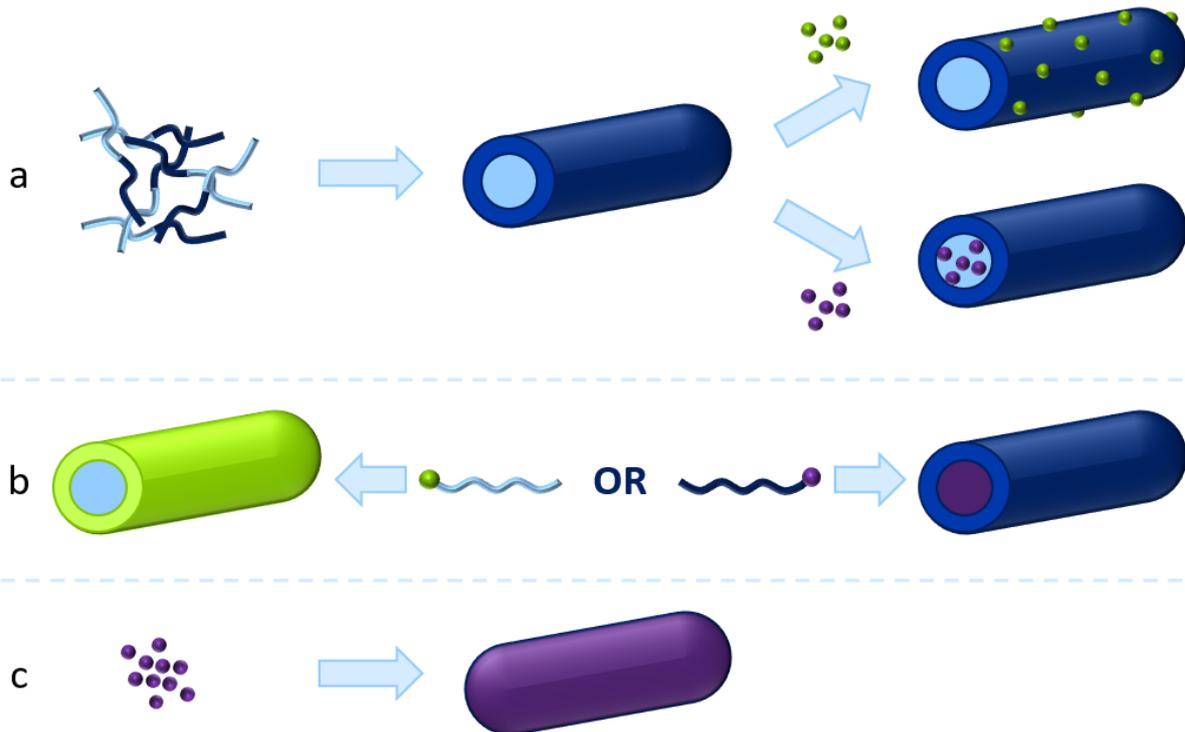
Figure 8: Drug loading into cylindrical nanomedicine. **a.** Physical encapsulation. **b.** Chemical encapsulation. **c.** Pure nanodrugs.

2. Drug-loaded nanocarriers

Drug-loaded nanocarriers consist in a drug physically entrapped in a nanocarrier, either in the core or at the surface depending of the drug hydrophilicity. The drug loading can be performed by two methods:

- the drug is solubilized either into the aqueous or the organic phase, prior to the formulation of the nanocarrier,

- or the empty nanocarrier is formulated and the drug is loaded *a posteriori*, by incubation of the nanocarrier suspension with a drug-containing solution.

However, these approaches find limitations due to poor drug contents, usually below 10 % (**Table 3**) and frequent burst release of the drug adsorbed onto the surface of the nanocarrier.

Table 3: Drug loading of polymer and peptide amphiphile nanocarriers

System	Filomicelles composition	Spheres composition	Drug	Filomicelles drug loading (%)	Compared to spheres		References
					Drug loading	Loading efficiency	
Polymers	PEG-PCL	PEG-PCL	PTX	~ 2.9-4.7*	↗ (x ~ 2)	↗ (x ~ 2)	5
	PEG-PCL	PEG-P(CL-GA)	PTX	10.6-12.4	↘ (~-2.5 %)*	↘ (~-15.1 %)*	51
	PEG-PCL (silica-coated)	PEG-PCL (silica-coated)	MTX	3.5	↗ (+ 1.4 %)*	↗ (+ 39.4 %)*	52
	PEG-PBCL	n. d.	PTX	~ 3.2*	n. d.	n. d.	53
	PGA-*g*-(PCL-*b*-PEG)	PEG-PCL	DOX	3	↘ (- 2.9 %)*	↘ (- 25 %)*	54
	mPEG-b-PDPA	n. d.	SCB	15.6	n. d.	n. d.	55
	PEG-PLLA	PEG-PDLLA	PTX	4.9-11.3	↗ (+ 1.5 %)*	↗ (+ 17.1 %)*	56,57
	PEG-PLLA	n. d.	PTX ± 17-AAG ± Rap	3.1-4.6 2.1-4.7 1.4-1.8	n. d.	n. d.	58
	PEG-PLA / PLA-Jeff-FA	n. d.	Betulin derivative	19.7-20	n. d.	n. d.	59
	FA-PEG-PLA-PEG-Acrylate / MPEG-PLA-PEG-acrylate	n. d.	DOX + SPIO	9 48	n. d.	n. d.	60
	LPEI-GT	n. d.	DNA	3.8*	n. d.	n. d.	61
	lPEI-*g*-PEG	n. d.	DNA	n. d.	n. d.	n. d.	62
	P(MeOx-b-BuOx-b-MeOx)	n. d.	Eto ± CP	16.2-~ 50 19.2-36.2	n. d.	n. d.	63
Peptide amphiphiles	qC$_8$-Tat	PTX		n. d.	~ 6.8	n. d.	n. d.	67
	C$_{16}$-A$_4$G$_3$E$_3$	CPT		n. d.	~ 1:28**	n. d.	n. d.	69

* Calculated from data

** Molar ratio drug:PAm

↗: increase; ↘: decrease; ~: comparable

2.1. Polymer-based nanocarriers

Among the variety of cylindrical nanomedicines recently developed, polymeric nanocarriers have been the most described in the literature. Indeed, tuning the chemical composition of polymers constitutes a simple mean for controlling micellar shape and functionalization.[105] The larger core volume of cylinders compared to spheres was expected to improve the drug loading capacity of the nanocarriers. Polyester-based filomicelles such as poly(ethyleneglycol)-poly(caprolactone) (PEG-PCL)[5] or poly(ethylene glycol)-poly(lactide) (PLA-PEG)[57] validated this expectation, while other studies by Shen *et al.*[106] or Zhao *et al.*[54] produced conflicting conclusions. Nevertheless, the latter was biaised by the variation of both the shape and the chemical composition of the investigated nanoassemblies. Indeed, while PEG-PCL formed here spherical micelles, the use of a poly(glycolide) (PGA) backbone grafted with pendant PEG-PCL chains was necessary to produce cylindrical NPs (NPs). And the PGA backbone has been presumed to prevent the reorganization of PEG-PCL, limiting their potential to host Doxorubicin (DOX) molecules. Simultaneously, Nair *et al.* demonstrated that the incorporation of a benzyl group to the PCL moiety (poly(alpha-benzyl carboxylate epsilon-caprolactone), PBCL) turned the core of the filomicelles more hydrophobic, hence improving their paclitaxel (PTX) loading capacity by ~ 40 % over PEG-PCL, along with a slower drug release resulting in an impressive anti-tumor efficacy..[53]. But despite those evolutions, the drug loading of filomicelles remains generally quite low, in the 5-10 % range **(Table 3)**. However, poly(2-oxazoline)-based amphiphilic polymers were shown recently to form worm-like particles with an impressive drug loading, superior to 50 % for the combination of paclitaxel (PTX) and a cisplatin prodrug (CP)[63]. This remains, to date, the filomicelle-forming polymers with the highest drug loading capacity.

Amphiphilic diblock copolymers are the most described polymer systems, due to their ability to form well-defined core-shell structures with a high thermodynamic stability.[106] In general, the hydrophobic blocks form the core of the nanoparticle while the hydrophilic segments constitute the shell. The hydrophobic block composition may be adapted to modulate the core volume and chemistry, and consequently to control the loading and the release of hydrophobic drugs.[53] The most employed hydrophilic polymer is the FDA-approved PEG due to its good biocompatibility and ability to reduce

opsonization, conferring stealthiness and long-circulating properties to the nanoassemblies.[107] The PEG weight fraction f_{EO} is a key parameter influencing the nanostructure obtained, since f_{EO} values comprised in the range 0.2-0.5 favor cylindrical shapes.[53,56,64,106,108,109] F_{EO} values above 0.5 correspond, on the contrary, to polymers with hydrophilic chains longer than hydrophobic, for which spherical morphologies are expected due to the higher surface area of spheres over cylinders. Nevertheless, Kim *et al.* reported the unexpected formation of filomicelles at $f_{EO} \sim 0.8$, using triblock polymers with poly[(R)-3-hydroxybutyrate] (PHB) as the hydrophobic block.[65] This has been attributed to the highly crystalline PHB core. Interestingly, varying the molar fraction and weight of pendant PEG chains grafted onto linear poly(ethylene imine) (lPEI) resulted in the formation of NPs of different shapes with transition towards spheres occurred for low f_{EO}, while filomicelles elongated with increasing f_{EO}[62]. The contradiction with the above discussion highlights the importance of the polymer morphology (*i.e.* linear or branched), along with the hydrophilic fraction, to determine the supramolecular organization of the resulting nanocarrier.

Discher and coworkers developed the first cylindrical filomicelles for drug delivery using chemically inert poly(ethylene glycol)-poly(ethylethylene) or biodegradable PEG-PCL.[5,6,98] The filomicelles spontaneously self-assembled after hydration of the polymers, whereas the control of the length was achieved by extrusion. The initial length of the filomicelles was a major factor influencing their persistence in the bloodstream: even if submitted to cell- and flow-induced fragmentation, the circulation time increases with the filomicelles initial length (up to one week for 8 µm-filomicelles and longer) after injection in the tail vein of rodents. Length also dictated the cellular uptake as short micelles were taken up more easily by macrophages than the longer ones. Those are extended along the blood flow, hence minimizing their interactions with phagocytic cells. Recently, PEG-PCL filomicelles loaded with methotrexate (MTX) were coated with silica. The stability of the silica coating hindered the polymer swelling and consequently improved the stability of the filomicelles allowing a better anti-cancer efficacy on MCF-7 cells, while slowing the drug release in buffer solution at pH = 7.4.[52]

Replacement of PCL block by another widely used polyester, PLA, led to the obtention of filomicelles with shape depending on the stereochemistry of the PLA block: poly(L-lactide) (PLLA) favored filomicelles or mixtures of spheres and filomicelles, while poly(DL-lactide) formed spherical micelles.[56,57] This was attributed to the higher rigidity of PLLA, favoring filomicelles, over PDLLA displaying L-lactide and D-lactide units randomly distributed along the polymer chain. Of note, Paclitaxel drug loading was comparable to that obtained for PEG-PCL filomicelles.[56] Similarly to PCL-based filomicelles, PLLA-PEG revealed a slower drug release at 71 days in buffers of various pH (~ 10, 15 and 22 % at pH 3.0, 5.5 and 7.4, respectively) compared to PDLLA-PEG spherical micelles (~ 30, 33 and 63 % at pH 3.0, 5.5 and 7.4, respectively).[57]

Polyester-based filomicelles were also successfully used for theranostic purposes. Yang *et al.* developed a multifunctional cylindrical nanovector obtained from a mixture of PEG-PLA-PEG-acrylate and folate-PEG-PLA-PEG-acrylate polymers, for the encapsulation of DOX as an anticancer drug and Small Particles of Iron Oxide (SPIO) as magnetic resonance imaging (MRI) contrast agent.[60] Folic acid (FA) allowed active cell recognition, as folate receptors are overexpressed on the cell surface of a wide range of human carcinomas[110], while acrylate groups were introduced to allow the crosslinking of the inner PEG layer, conferring enhanced stability to the nanocarrier and sustained doxorubicin delivery.

Polymers can be relatively easily functionalized to bring stimuli-responsiveness properties to the nanocarriers. As an example, 3-diethylaminopropyl[111] or poly(2-diisopropyl methacrylate) (PDPA)[55,109] were used as the hydrophobic blocks of PEG-based polymer chain. These moieties include amino groups whose protonation at acidic pH will turn them hydrophobic to hydrophilic, causing the degradation of the filomicelles, hence triggering the drug release. This feature is particularly interesting regarding cancer therapy, since the pH in the extracellular environment of solid tumors is slightly lower than in healthy tissues.

2.2. Peptide amphiphiles

Peptide amphiphiles (PAm) are basically constituted of a biologically active hydrophilic peptide chemically coupled to one or several alkyl chains. Alkyl chain and peptide must be carefully chosen to optimize the properties of the formed nanofibers. Due to their hydrophobic nature, the alkyl tails tend to aggregate in water, forming the nanofibers core to restrict contact with the aqueous environment. This is the driving force of the self-assembly process. Simultaneously, the nature and conformation of the peptide headgroup influences the size and shape of the nanoassemblies: peptides in α-helixes or random coil conformation may form either spherical or cylindrical micelles, while peptides forming β-sheets will exclusively form nanofibers.[112] The β-sheet role in the formation of elongated structures was investigated in detail by Paramonov *et al.*[113] After screening 26 amphiphilic peptides composed of a palmitic C_{16} chain linked to the peptide headgroup *via* a glycine-based linker, they highlighted the necessity for the four amino acids located the closest to the nanoparticle core to be able to form β-sheet hydrogen bonds with neighboring peptides to allow the formation of nanofibers.[113] To go further, Tirrell group focused few years later on the self-assembly mechanism of worm-like PAm through the example of a conjugate made of a C_{16} alkyl chain linked to three tryptophan and one lysine units (C16-W3K). Notably, they highlighted the possibility to initiate a transition from sphere to rod by triggering a transition in the peptide conformation from α-helixes to β-sheets after heating. The growth mechanism was shown to occur through the attachment of transient spherical micelles to the end of the growing cylindrical micelles upon heating **(Fig 9a)**.[114,115] With successive developments, additional structural region can be added to the initial alkyl core and β-sheet-forming moieties, like a third segment composed of a sequence of amino acids designed to allow structural modifications (improve water solubility, trigger gelation…) and possibly a fourth domain consisting in a sequence incorporating a bioactive signal, like cell adhesion for example or therapeutic molecule. **(Fig 9b, c)**.[116,117]
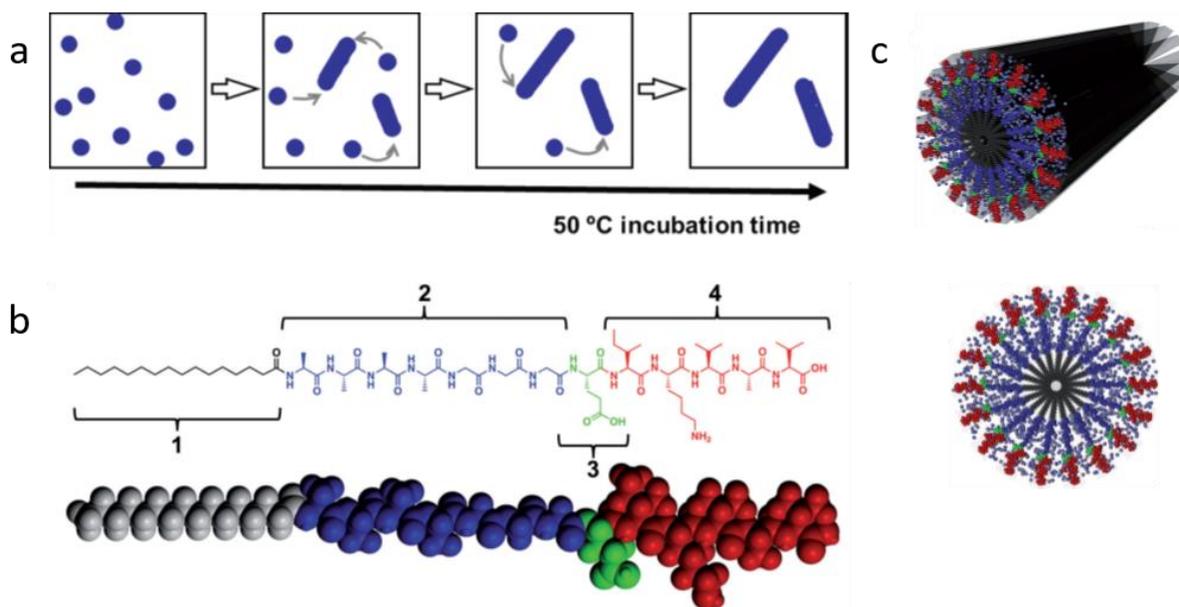
Figure 9: a. Self-assembly process of worm-like micelle in the PAm C16-W3K during the 50°C incubation. **b.** Molecular structure of a representative peptide amphiphile with four rationally designed chemical entities. **c.** Molecular graphics illustration of the peptide amphiphile molecule and its self-assembly into nanofibers as well as an illustration of the cross section of these fibers, highlighting the extensive hydration of the peptide shell. Adapted from [115] (**a**) and [116] (**b,c**).

The formulation process of drug loaded amphiphilic peptide nanofibers is straightforward as they spontaneously self-assemble after hydration with usually water or PBS at pH 7.4. Small anticancer drugs can be loaded into the nanofibers core by mixing the drug and PAm, prior to the hydration step, in a strong solvent like hexafluoro-2-propanol to allow molecular mixing. The obtained mixture is then evaporated to complete dryness before hydration with water or buffer to obtain the self-assembled structures.[66,67,69,70,118] The drug loading into peptide-based nanofibers is rarely mentioned in the literature. However, Soukasene *et al.* reported a molar ratio of 1:28, between the encapsulated drug, here camptothecin (CPT), and the peptide nanocarrier[69], while in another study Tat-based nanofibers loaded with PTX revealed a drug content of 6.8 %, making that those elongated nanoassemblies may be considered with a high loading capacity.[67] The rationale was to design PAm nanofibers with multiple short C_8 tails rather than with a single one to widen the core and reduce its crystallinity, hence allowing the incorporation of more hydrophobic drug. And effectively, the 4-tail conjugate incorporated more drug than the 1-tailed and 2-tailed counterparts. Of note, the carrier rigidity generally increased with the drug loading, as another potential way to control the physico-chemical properties of the nanocarriers and to modulate their behavior after administration.

Interestingly, the length of PAm nanofibers may be adjustable. For example, addition of various amounts of the capping phospholipid 1,2-dioleoyl-sn-glycero-3-phosphoethanolamine (DOPE) to the elastin-based PAm nanofibers stopped their growth by forming endcaps: nanofibers length decreased in a controlled way when increasing the DOPE amount, without alteration of the fibers diameter.[66] Since the length of nanofibers is largely involved in the biological processes, this study could provide a simple mean to modulate the therapeutic response of drug loaded into PAm nanofibers.

PAm as nanocarriers have mainly been applied to cancer treatment: after loading of anticancer drug, they generally exhibited an increased *in vitro* toxicity against several lines of breast cancer cells compared to the free drug, along with a reduction of the tumor volume *in vivo*.[68,69,118] Similarly to polymeric filomicelles, stimuli-sensitive PAm can be designed to release drug in a controlled way. Specific sequences substrate of enzymes like matrix metalloproteinase-2 (MMP-2)[71] or protein kinase A (PKA), both overexpressed in various cancers, can be incorporated into the amino acids sequence of the peptide to specifically trigger the drug release into the tumor.[68,71] A first strategy was to insert the MMP-2-sensitive sequence between the alkyl chain and an RGDS epitope (used for recognition). After complexation with cisplatin (CDDP), the enzymatic degradation resulted in the cleavage of the PAm, triggering the release of CDDP-RGDS complexe. In another way, the insertion of a sequence sensitive to PKA led to a completely different mechanism: the phosphorylation of the substrate by PKA caused the disruption of the nanofibrous structure without destroying the PAm, hence allowing the release of the encapsulated doxorubicin in the presence of cancer cells. The reverse reaction, dephosphorylation by alkaline phosphatase, allowed then the reversible formation of the nanofibers.[68] Recently, PAm nanofibers were adapted to treat atherosclerosis. The design nanofibers made of apolipoprotein-mimetic peptides permitted a specific accumulation into the atherosclerotic plaques in a model of LDLR KO mice and an improved cholesterol efflux from macrophages after loading the fibers with liver X receptor agonist.[70]

Under specific conditions, Pam nanofibers may entangle to form hydrogels. The peptide headgroup can be functionalized by small molecules such as hydrogelators, allowing the gelation of the PAm suspension after screening of the electrostatic interactions, generally by the addition of a

counterion[88]. However, the encapsulated drug itself can be used as the screening agent. For instance, CDDP loading into PAm suspension was found to induce gelation by forming inter-fiber complexes between the carboxylic acids of the peptide headgroups and the CDDP. Unexpectedly, this hydrogel displayed a high drug release *in vitro*, up to 80 % after 24 h at pH 7.4.[71] More recently, a gel was designed by the co-assembly of positively charged Lauryl-VVAGEE PAm and negatively charged Lauryl-VVAGKKK-AM PAm for DOX encapsulation. The drug release rate *in vitro* could then be adjusted by varying the initial PAm concentration. Prolonged drug delivery resulted in tumor growth and tumor volume reduction in 4T1 tumor-bearing BALB/c mice.[118] The potentialities of controlling the gelation as well as the drug release, along with the mechanical properties of the hydrogel make them interesting candidates also for the development of prolonged local drug delivery systems.

3. Bioconjugate-based nanocarriers

Chemical drug loading relies on the covalent linkage of a drug to an appropriately chosen building material. This approach led to the development of an important variety of one-component nanomedicines. Among the numerous advantages of these drug delivery systems, one can cite a dramatic increase of the drug content **(Table 4)** and thus a reduced amount of inert material to be administered to the patients, an improved solubility of the drug, the prevention of potential burst release and a better bioavailability.[119,120]

Table 4: Drug loading of prodrug nanocarriers

System	Composition	Drug	Drug loading (%)	References
Polymers-based	PEG-TetraCPT	CPT	30.6	[100]
	PEG-OctaCPT	CPT	38.9	[100]
	POEGMA-*b*-P(ST-*co*-VBA)	DOX	5.0	[101]
Lipid-based	DLPU	Uri	30.6*	[121]
	DLPA	Ade	32.6*	[76]
	SQ-Dox	DOX	57.0	[122]
	OA-Ara	Ara-C	47.9*	[77]
	LA-Ara	Ara-C	57.3	[78]
	PA-Ara	Ara-C	50.4*	[79]
Peptide-based	Ket-L-VEVE	Ket	33.4*	[81]
	CPT-buSS-Tau	CPT	23-31	[82]
	dCPT-K2	CPT	43	[123]
	dCPT-OEG$_5$-K2	CPT	36	[123]
	dCPT-Sup35-K2	CPT	28	[123]
	CPT-PTX-Sup35	CPT	29	[83]
		+ PTX	12	
	DOX-KGFRWR	DOX	31.9*	[86]
	PTX-buSS-Tau	PTX	41.0	[87]
Supramolecular hydrogels	TA-SA-Glu	TA	62.3*	[124]
	DEX-SA	DEX	77.0*	[89,125]
	PTX-SA	PTX	87.9*	[90]
	CRB-FFE-YSV	CRB	26.7*	[91]
		+ YSV	34.0*	

* Calculated from data

3.1. Polymer-based conjugates

Two approaches exist to develop drug-polymer filomicelles. The first method consists in using the drug molecule itself as one of the material building blocks. For example, Zhou *et al*. have chosen to exploit the hydrophobic nature CPT and have synthesized PEG_{45}-b-dendritic polylysine-camptothecin (PEG_{45}-xCPT) conjugates.[100] They discovered that by carefully choosing both the number of CPT molecules linked to dendritic polylysine (DPLL) moieties and the number of the dendritic generations altered the conjugate amphiphilicity, hence allowing the obtention of various nanostructures. More precisely, the conjugates with four and eight CPT molecules (PEG_{45}-TetraCPT and PEG_{45}-OctaCPT, respectively) allowed to obtain nanorods with drug content of 30.6 % and 38.9 %, respectively, while assemblies with one or two CPT molecules only displayed spheres with drug loadings of 13.4 % for PEG_{45}-CPT and 21.4 % for PEG_{45}-DiCPT. Such aggregates were formed by a simple procedure: briefly, deionized water was added dropwise under stirring into a filtered solution of PEG_{45}-xCPT in *N,N*-dimethylformamide (DMF). The DMF was then removed by dialysis. The obtained PEG_{45}-TetraCPT nanorods dimensions were ~ 60 nm diameter and 500 nm length, while the PEG_{45}-OctaCPT were bigger: ~ 100 nm diameter and 1 µm length. TEM observations revealed rigid rods, as a consequence of the hydrogen bonding between DPLL amide groups and CPT π-π stacking **(Figure 10)**. Both PEG_{45}-TetraCPT and PEG_{45}-OctaCPT presented improved therapeutic performances compared to spherical PEG_{45}-DiCPT **(Table 2),** like longer blood circulation, faster cell uptake and better drug release into the cytosol, making them good candidates for tumor drug delivery.

Another approach consisted in the conjugation by polymerization-induced self-assembly (PISA) of the drug directly to the polymer NPs after their formation. PISA consists in the synthesis of block copolymers for which the block undergoing polymerization is insoluble in the reaction media, hence triggering the self-assembly *in situ*.[101,105] It has been shown that in the case of poly[oligo(ethyleneglycol)methacrylate]-*block*-[poly(styrene)-*co*-poly(vinyl benzaldehyde)] (POEGMA-*b*-P(ST-*co*-VBA)), the morphology of the aggregates was related to the degree of polymerization (DP_n) of the P(ST-*co*-VBA) block, forming the core of the NPs. Transition towards elongated morphologies, like worms or rods, occurs with increasing reaction time. Reaction with the

aldehyde groups brought by the styrene units allowed then both crosslinking the core of the nanoassemblies and doxorubicin conjugation. However, this approach resulted in a drug loading of only 5 %, which remains a low value for chemical drug loading. These elongated morphologies revealed, however, decreased IC_{50} and increased cell uptake compared to spheres, but concerning drug release no significant differences were noted between the two structures **(Table 2)**. This method was further successfully applied to the conjugation of gadolinium complex Gd-DOTA to poly(glycidyl methacrylate)-based polymer, in order to build new worm-like MRI contrast agent with improved r_1 relaxivity comparatively to the spherical counterparts. And this was attributed to the larger core volume of worm-like micelles, hence slower rotational dynamics.[72]
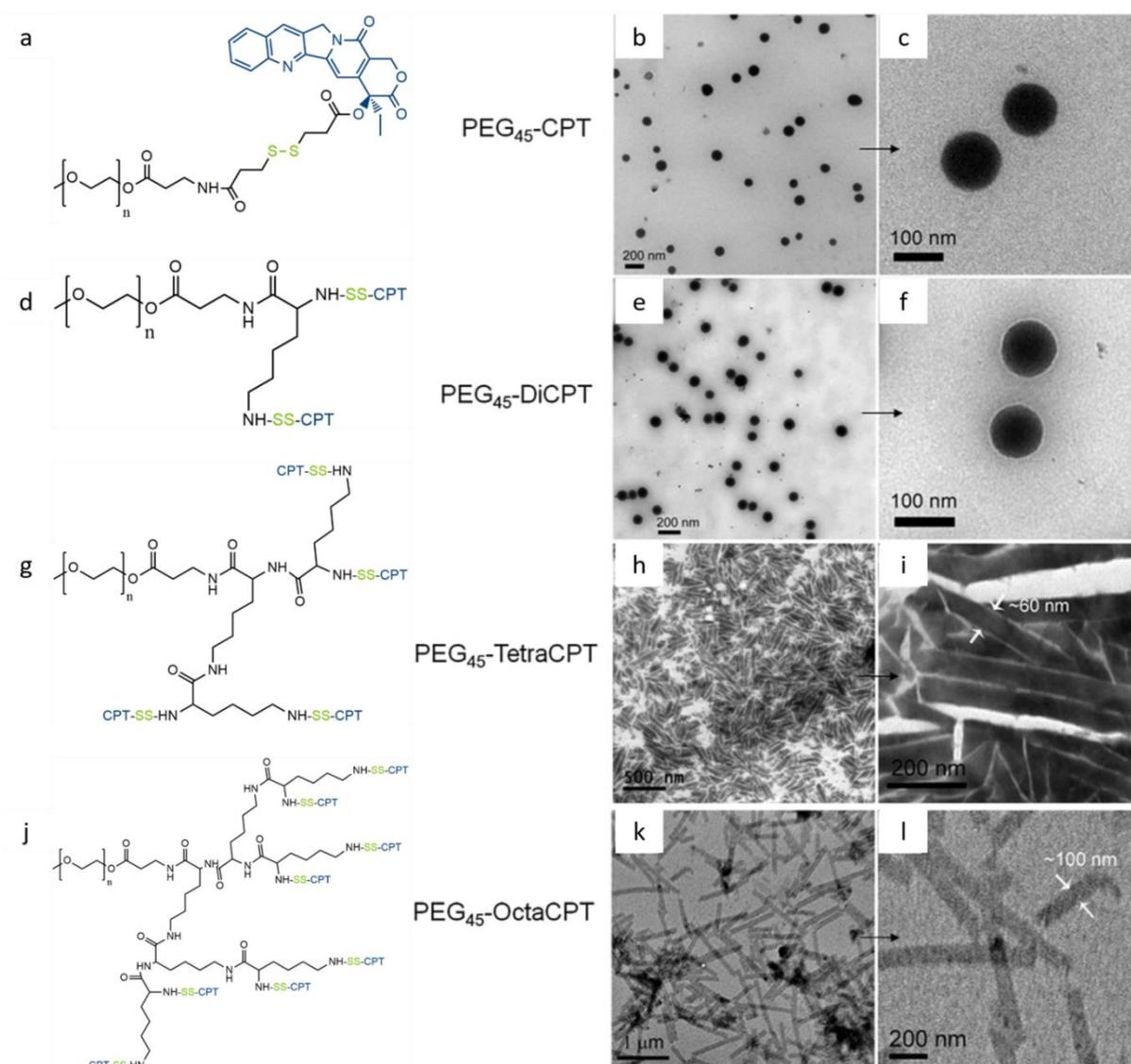

Figure 10: Chemical structure and TEM images (various magnifications) of PEG$_{45}$-CPT (a-c), PEG$_{45}$-diCPT (d-f), PEG$_{45}$-TetraCPT (g-i) and PEG$_{45}$-OctaCPT (j-l). Adapted from [100].

3.2. Lipid-based conjugates

Drug-lipid conjugates spontaneously forming worm-like micelles appeared in the early 2000's with the development of phospholiponucleosides consisting in nucleosidic headgroups covalently attached to one or two phospholipids.[74,121] For instance, 1,2-dilauroyl-sn-glycero-3-phosphatidyluridine (DLPU), composed of two C12 chains linked to uridine (Uri), assembled into long flexible cylindrical aggregates after solubilizing in PBS (pH 7.5), with length growing with bioconjugate concentration. Replacing uridine by adenosine (Ade) to form 1,2-dilauroyl-sn-glycero-3-phosphatidyladenosine (DLPA), led to worm-like micelles evolving towards helicoidal assemblies upon ageing. Mixtures of DLPU and DLPA behaved the same way than DLPA alone. An explanation was found in the higher stacking properties of purine bases compared to pyridine, hence the capacity of adenosine to drive the micelles structure.[74,76,121] While these drug-lipid conjugates opened the way to lipid-based worm-like micelles in the drug delivery field, their pharmaceutical activity was not investigated, despite the wide use of nucleoside to cure many diseases, including leukemias and HIV-infections.

Lipid-based worm-like micelles are usually obtained by the nanoprecipitation method, also called solvent displacement. Briefly, this straightforward approach consists in the solubilization of the amphiphile bioconjugate into a water-miscible organic solvent. The obtained solution is further added dropwise into an aqueous phase and the solvent is finally removed by evaporation, dialysis or centrifugation.[77–79,122] This formulation process was used to obtain oleic acid-cytarabine (OA-Ara) prodrug elongated nanoaggregates **(Fig 11)**. Although the opposition of nanoprecipitation (bottom-up) to the simple water dispersion obtained through sonication (top-down) led in both cases to helical fibers, their length and rigidity differed. The bottom-up process resulted in long entangled spirals, probably due to the centrifugation and redispersion steps to remove the solvent from the aqueous phase, while the top-down procedure formed shorter straight spirals. The longer ultrasonication time of the top-down process also helped reduce the length of the OA-Ara fibers.[77] Applying the bottom-up strategy to cytarabine (Ara-C) prodrugs coupled to other fatty acids (palmitic and lauric acids, PA-Ara and LA-Ara, respectively) led to the obtention of similar spirals.[78,79] However, no clear trend emerged

concerning the chain length evolution.
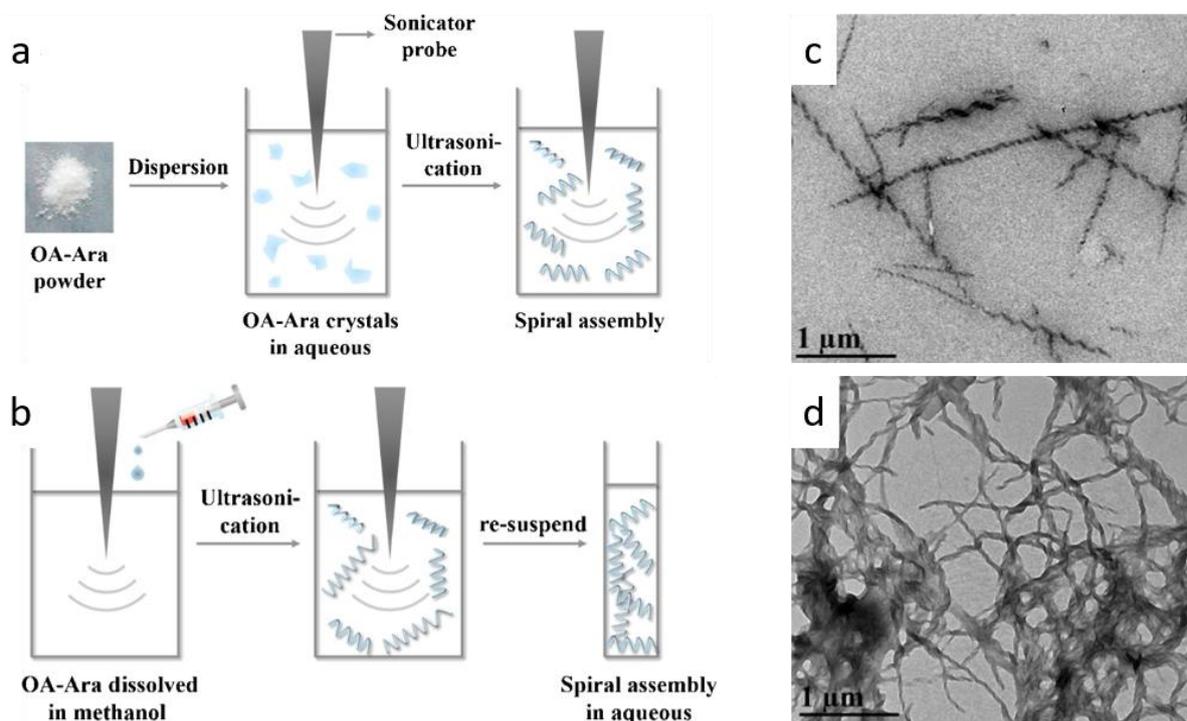
Figure 11: Schematic representation of sonication assisted OA-Ara assembly using the top-down (**a**) and bottom-up (**b**) approaches. TEM images of OA-Ara assembly prepared using top-down (**c**) and bottom-up (**d**) approaches. Adapted from[77].

The so-called "squalenoylation" approach has been developed since 2006 by Couvreur's group. This method consists in the covalent coupling of various drugs to squalene, a natural triterpene precursor of the cholesterol biosynthesis[126]. Due to the dynamically folded conformation of squalene, the resulting bioconjugates self-organized as spherical NPs with improved pharmacological activity for the treatment of cancer[127,128], neurological disorders[129] as well as for pain alleviation[130]. Interestingly, concerning the shape of these squalene-based nanoassemblies, squalenoyl-doxorubicin (SQ-Dox) represents an exception, forming elongated cylinders refolding into loop-train rather than spherical structures after simple nanoprecipitation into water. This unusual behavior originates from the strong π-π stacking propensity of DOX, enabling the formation of clusters of up to six DOX headgroups at the NPs periphery. DOX stacking combined to hydrophobic squalene-squalene interactions drive the uniaxial growth of those nanoassemblies.[80] This original structure allowed

decreased overall and cardiac toxicities, along with improved anticancer activity compared to free DOX. Still more interestingly, SQ-Dox was more potent than the two currently available liposomal formulations of doxorubicin, *ie*. Myocet and Caelyx.[122]

3.3. Peptide-based conjugates

Inspired by the design of peptide amphiphiles, self-assembling peptide-drug conjugates, also called drug amphiphiles represents a new class of prodrugs built from a hydrophobic drug linked to a hydrophilic peptide through a cleavable linker. As a result, drug amphiphiles combine both the advantages of peptide-based nanocarriers, like a high degree of functionality, biodegradability and safety, and those of one-component nanomedicines, like an increased drug content in the 25-45 % range **(Table 4)**, and avoidance of the use of additional excipients.[131]

Similarly to peptide amphiphiles, drug amphiphiles easily self-assemble over hours after the simple solubilization in water at physiological pH, hence avoiding the use of organic solvents whose residues can be problematic for clinical development. However, the preparation of these nanomedicines requires more time. The self-assembling mechanism of drug amphiphile relies on the π-π stacking properties of drug headgroups, such as CPT or Ketoprofene (Ket), which drive the first steps of the self-assembly process by acting as anchors to initiate the building of the nanofibers core. Afterwards, the intermolecular H-bond between the peptides would allow the β-sheet formation and the unidirectional growth.[81,132] Ket-L-VEVE drug amphiphile was used as a model to investigate this process in detail and to screen the external factors influencing the nanostructure, with the aim to establish a kind of a practical guide to design prodrugs self-assembling into particles with controlled morphologies. The pH of the nanofibers solution was shown to modulate their diameter by acting on the ionization state of the conjugate. On another hand, the addition of H-bonding inhibitor, such as urea, totally prevented the self-assembly. Of note, Ket-L-VEVE first assembled into nanorods undergoing ageing-induced transition towards nanofibers and multi-layered nanoribbons through end-to-end and fiber-to-fiber pathways. Twisting of the aggregates was a consequence of the lateral

stacking between fibers and of the chirality of amino acids (**Figure 12**).[81]
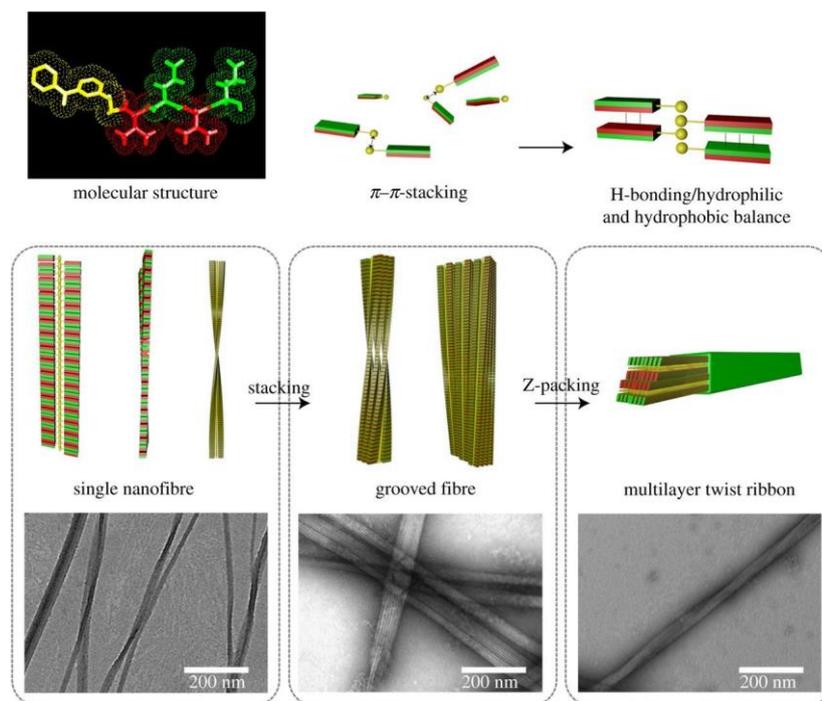
Figure 12: The mechanism of Ket-L-VEVE self-assembly.[81] Yellow represents the Ket moiety, red is for valine (V) and green for glutamic acid (E).

Cui *et al*. developed a drug amphiphile with high drug content for cancer treatment by using the β-sheet peptide VQIVYK, derived from the Tau protein, and conjugated to drug molecules through a 4-(pyridin-2-yl-disulfanyl)butyrate (buSS) linker, sensitive to the intracellular reducing agent glutathione (GSH). Conjugation with CPT led to CPT-buSS-Tau nanoaggregates with length and shape depending on the number of drug molecules conjugated to the peptide. Conjugates with 1 and 2 CPT molecules (mCPT-buSS-Tau and dCPT-buSS-Tau, respectively) formed nanofibers but dCPT-buSS-Tau displayed the most improved anticancer efficacy.[82] Starting from this conjugate, further investigations included comparison of different GSH-sensitive linkers[133], different hydrophilic moieties[123] or the use of a miktoarm star peptide, enabling the conjugation of different drugs (CPT and PTX) to the peptide bioconjugate, in order to overcome multi-drug resistance[83]. While all these molecular entities assembled into elongated shapes (nanofibers or nanotubes), the presence of β-sheet forming peptides, like Tau or Sup35, was mandatory to promote the formation of nanofibers. However,

the shape of these molecular assemblies was not the key parameter dictating the therapeutic efficacy, since surface chemistry and fast drug release were found to be much more influential.[123]

Another approach consisted in the *in situ* self-assembly of nanocarriers triggered by specific physiological parameters. As a proof of concept, Zhang *et al*. developed enzyme-responsive P18-PLGVRGRGD conjugate made of purpurin18 (P18) as the functional molecule (photosensitizer) with π-π stacking properties, PLGVRG as the enzyme-responsive sequence and RGD being the targeting ligand. The idea was to allow the diffusion of the hydrophilic bioconjugate into cancer cells. The linker peptide would then be cleaved by gelatinase, overexpressed in cancer cells. As a result, the drug hydrophobicity would increase, allowing the self-assembly as nanofibers which were able to increase the photoacoustic response for tumor detection, better than the controls not forming fibers. And an increased anti-cancer efficacy was also observed, consecutive to the slow activation of the drug release.[84] However, despite the promising results of this study, we didn't find any further studies with a similar prodrug approach.

3.4. Supramolecular hydrogels

Under certain conditions, prodrug-based nanofibers can entangle to form supramolecular hydrogels. The gelation occurs over hours and can be induced by various stimuli such as heating[124], charge screening by electrolyte addition[88–91,125,134] or pH modification[135], enzymatic reaction *etc*.[92,136] The formulation of active substances into hydrogels allows the release up to several days of the prodrug, then of the drug at specific sites, making those systems particularly interesting for local drug delivery. So far, nanofiber-based hydrogels have shown promising results in cancer therapy and for anti-inflammatory treatments.

One of the first reported examples of nanofiber-based hydrogels consisted in an enzyme-sensitive drug amphiphile. Xu *et al*. developed in the early 2010's, PTX coupled *via* a succinic acid (SA) linker, to a peptide containing a phosphatase substrate sequence (NapFFKYp). The resulting PTX-SA-NapFFKYp was able to form a gel after overnight incubation with phosphatase. The obtained

formulation preserved the anticancer activity of PTX, thanks to a slow release of the drug in physiological conditions without initial burst release (~ 3 % in 24 h).[92]

Following the emergence of peptide and drug amphiphiles, the Stupp group developed a PAm hydrogelator coupled to nabumetone (Nb)[88] or dexamethasone (DEX)[134] through a labile hydrazone linker. Drug-bearing PAm formed fibers able to gelify at a low concentration, following the addition of CaCl2. Both drugs were found to be slowly released (~ 35 % Nb released after 24 days and ~ 40 % DEX released after 32 days) at physiological pH. The DEX hydrogel was able to confer cytoprotective and anti-inflammatory action *in vivo* and reduced localized acute inflammatory response in mice.

However, the release rate relies also on the gel structure, including the network properties at the interface and the stability of the nanofibers into the matrix, consequences of the material design. Precise tuning drug amphiphile PTX-buSS-GGVVVRGDR revealed that the addition of alkyl side chains decreased the critical aggregation concentration (CAC) (as a consequence of higher hydrophobicity) resulting in a slower drug release, while increasing the CAC by the incorporation of oppositely charged amino acids in the sequence favored an accelerated release. The presence of the RGDR peptide promoted the tumor penetration of the drug amphiphile due to its high binding affinity with neutropilin-1, hence an improved tumor growth inhibition in a U87 spheroid model. [137] Using a peptide drug like tyroservatide (YSV) in the peptide moiety allowed further application of this approach to multidrug therapy.[91] For example, drug amphiphile chlorambucil (CRB)-FFE-YSV was able to form hydrogel *via* a heating-cooling method. The gel network conferred a protection of the prodrug against enzymatic degradation, permitting an elevated cellular uptake of the peptide-drug-conjugate released from the hydrogel. The synergy between CRB drug and YSV peptide displayed excellent antitumor activity in HepG2-tumor-bearing BALB/c nude mice. It was suggested that the decent biocompatibility of the hydrogel combined with a sustained and controllable drug release makes it interesting for local cancer treatment. Of course, this approach may find a limitation in the inability to reach potential metastatis anterior to the beginning of the treatment.[131]

Prodrugs based on small diacids may also be used exploited to form hydrogels, as demonstrated with SA. This diacid was successfully conjugated to DEX for ocular anti-inflammatory treatments[89,124,125] and to PTX for cancer therapy.[90] The low molecular weight of SA resulted in very impressive drug loadings, up to almost 90 % in the case of PTX-SA **(Table 4)**. If SA-prodrug nanofibers formed spontaneously after solubilization in PBS, their gelation occurred only after the partial hydrolysis of the ester linker between the drug and the succinic acid, which may be induced by the addition of sodium carbonate. Interestingly, the incorporation of a glucosamine (Glu) moiety in the linkage between triamcinolone acetonide (TA) and SA led to the formation of TA-SA-Glu as a hydrogelator able to undergo reversible sol-gel transitions depending only on temperature variations, without the need to add supplementary charged species.[124] In addition to the sustained and controlled released properties previously described, succinated prodrug hydrogelators formed thixotropic hydrogels. This is of particular interest for the design of injectable systems, but also for ocular delivery. Indeed, such formulations could turn liquid when the patients blink and rapidly recover the gel state afterwards to progressively deliver the anti-inflammatory drug. The cross-linking density might be tuned by carefully adjusting calcium chloride ($CaCl_2$) concentration, and consequently dictating the gelation rate, as well as, the drug release mechanism. High $CaCl_2$ concentrations favored crosslinking, conferring improved mechanical strength to the gel and slowing down the drug release.[125] Based on these promising features, DEX-SA hydrogels have shown improved corneal retention and bioavailability with good intraocular biocompatibility compared to the free drug.[89]

4. Pure nanodrugs

The design of pure nanodrugs represents a relevant approach for the delivery of drugs with self-aggregation properties and poor water solubility.[120] Based on these criteria, interest has been directed towards CPT and its derivatives. CPT is an antineoplastic agent constituted of five rings, one of which bearing a chiral center at position C_{20}, highly influencing the drug efficacy. However, CPT displays several limitations, such as a high toxicity and the sensitivity of the lactone ring to hydrolysis,

turning rapidly after administration into the inactive carboxylate form.[138] To overcome those restrictions, numerous CPT derivatives have been synthesized but only few of them displayed self-assembling capabilities **(Fig 13)**: CPT itself[50,93,94,139], 10-hydroxy camptothecin (HCPT)[49,73,95,96,102,103,139] and 7-ethyl-10-hydroxycamptohecin (SN-38)[97] bearing a hydroxyl function in C_{10} position to help stabilization in physiological medias[140], carboxylic camptothecin (CPT-COOH)[139] and camptothecin-20(*S*)-glycinate (CPT-NH$_2$)[96] for which the conjugation in the C_{20} position was expected to stabilize the lactone rings and to confer sustained release properties **(Fig 13)**.[141,142]
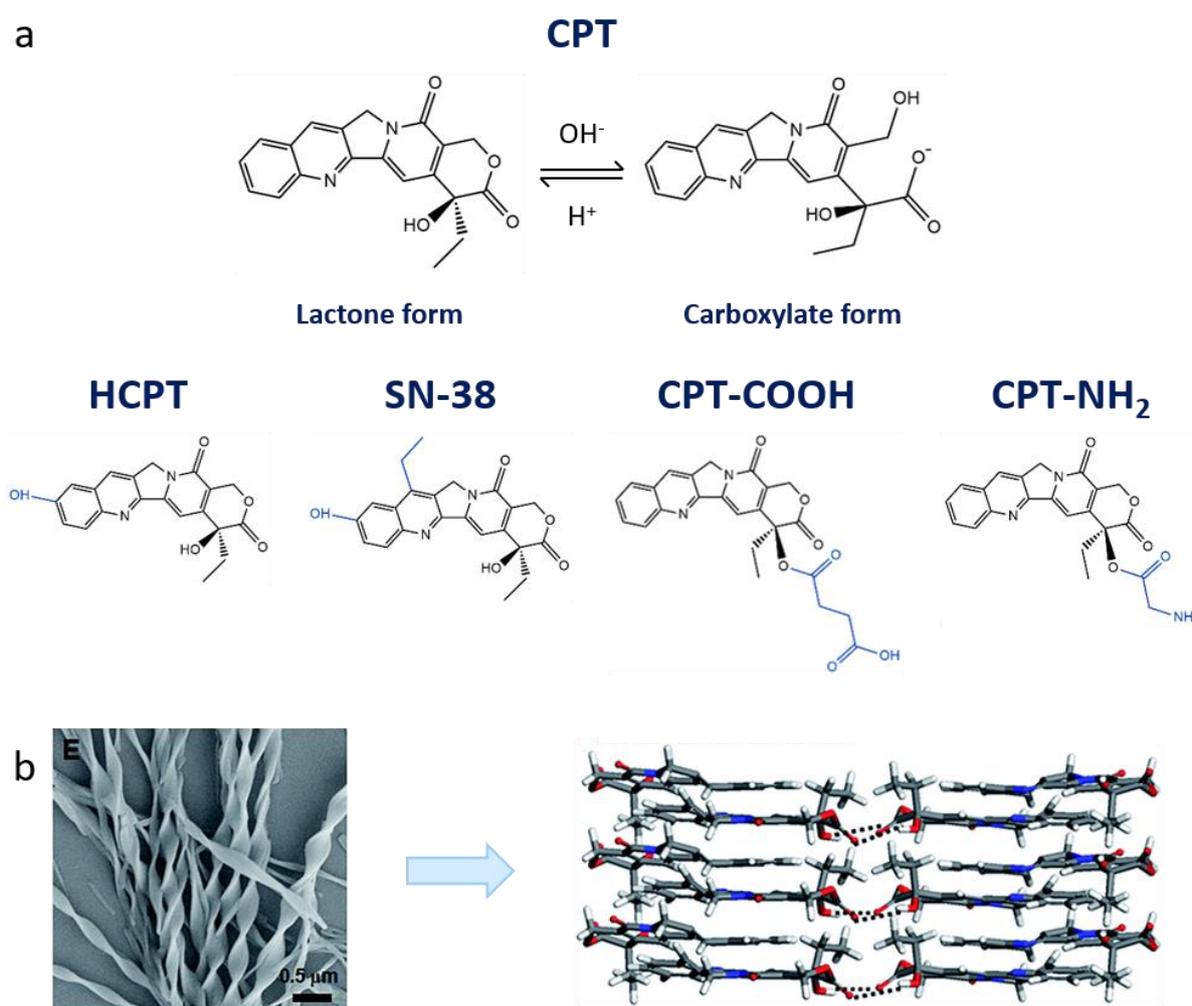
Figure 13: Structure of CPT and its derivatives (**a**). SEM image of CPT sample (3 x 10^{-4} mol L^{-1}) at room temperature and schematic illustration of molecules arrangement in CPT helical nanoribbons, dashed lines represent intermolecular H-bonds. Adapted from [94].

CPT and analogues were found to self-assemble in aqueous media after a very simple process: after the solubilization of the drug in a solvent (usually dimethyl sulfoxide) and the addition

of this solution to H_2O (under stirring or sonication), the helical nanoribbons formed. The planarity of CPT molecules combined to their π-π stacking and H-bonding properties likely favor the uniaxial growth of the fibers, forming edge-to-edge J-type stacks. Right-handed helicity has been reported, as a consequence of the presence of a chiral center in C_{20} position.[94,139] The stability of these nanostructures for several days suggests that the self-assembling enables the protection of the lactone ring. Nevertheless, Ma *et al.* took advantage of the sensitivity of this functional group to hydrolysis to trigger the pH-induced reversible assembly of CPT into nanofibers: raising the pH of a suspension of CPT helical nanoribbons led to the formation of the water-soluble carboxylate form, hence the disappearance of the nanostructures. However, decreasing the pH back to 5 allowed the reversible formation of nanoribbons.[94] Additionally, the length of the CPT nanoribbons revealed to be tunable by adjusting the sonication time of the nano-suspension: longest sonication durations produced shorter lengths without destruction of the helical morphology. Interestingly, this observation allowed to maximize the therapeutic efficacy of those nanostructures, as it was shown that comparatively to the longer nanoribbons (several μm), short nanoribbons with ~ 1 μm length displayed an improved uptake by 4T1 cells, a higher cytotoxicity and a faster drug release[50].

The self-assembly of CPT prodrugs was driven by the same stacking and H-bonding properties than the original drug, however with a loss of the helical conformation. Noteworthy, unlike CPT, the prodrug nanostructures revealed poor stability, as they started aggregating or sedimenting within minutes or hours. To overcome this limitation, different strategies were adopted. For example, the SN-38 CPT derivative was dimerized through various linkers (carbamate, ester or ether). However, this modification made the drug less planar, thus hindering the unidirectional growth and favoring the spherical morphology.[97]

Supramolecular elongated nanodrugs have been successfully used to encapsulate other small molecules for multidrug therapy. Mitragotri's group has proposed the first pure multidrug nanomedicine without using PEG or other stabilizer. The design was as follows: CPT nanorods were coated with trastazumab (TTZ) and loaded with DOX. Those three drugs were distributed into different cell compartments (late endosomes, recycled in plasma membrane, or in nucleus for CPT,

TTZ and DOX, respectively), hence allowing cytoplasmic targeting and synergistic anticancer efficacy against BT-474 breast cancer cells.[93] More recently, combinations of drug and photosensitizers were also proposed such as HCPT/chlorin e6 (Ce6)[95] or PTX/ di-iodinated borondipyrromethene[143] for dual chemo-photodynamic therapy purposes. Such formulations revealed superior anticancer activity comparatively to the corresponding monotherapies, allowing complete tumor growth inhibition *in vivo*, while reducing side effects.

IV. Conclusion

Important progresses have been realized over the last years in the comprehension of the driving forces behind the formation of cylindrical NPs (filomicelles, worm-like NPs or rod-like NPs). The self-assembling mechanism and supramolecular organization are key parameters to optimize the therapeutic efficacy of nanomedicines. Their understanding has allowed to formulate drug delivery devices using a wide range of biocompatible materials, from simple lipids or diblock polymers to more complex materials functionalized with targeting ligands, stimuli-responsive moieties and loading several drugs and/or dyes for theranostic applications. The viscoelasticity of worm-like particles has also successfully been exploited to design hydrogels suitable for local delivery.

All the described approaches have, however, both advantages and limitations, making difficult the task of designing an ideal cylindrical nanocarrier. Bioconjugates and pure nanodrug approaches are probably more promising than the physical encapsulation, in terms of drug loading capacity and avoidance of burst release after administration. Indeed, using a limited amount of carrier material may help to avoid potential toxicological issues. However, the synthesis of some bioconjugates may require complicated chemistry, while nanodrug design may after all necessitate also the addition of PEG to be stable in biological environments. Among the various drug conjugates, polymer-drug conjugates are probably among the easiest to design and functionalize. Similarly to lipid-conjugates, their formulation takes few time but requires the use of organic solvent that will need to be removed. Peptide-drug conjugates circumvent this drawback, as they simply assemble after

dispersion in water. But this process is time-consuming as it needs hours to days to equilibrate. Furthermore, most of these strategies apply to a limited number of drug molecules, as they often rely on π-π stacking properties to form elongated nanostructures. Nevertheless, despite the difficulty to design the ideal cylindrical drug delivery system, all reports tackling the comparison between spherical and cylindrical nanovectors agreed on the therapeutic benefits brought by the latter in preclinical *in vitro* or *in vivo* experiments.

V. References

(1)   Porte, G.; Appell, J. Growth and Size Distributions of Cetylpyridinium Bromide Micelles in High Ionic Strength Aqueous Solutions. *The Journal of Physical Chemistry* **1981**, *85* (17), 2511–2519.

(2)   Dreiss, C. A. Wormlike Micelles: Where Do We Stand? Recent Developments, Linear Rheology and Scattering Techniques. *Soft Matter* **2007**, *3* (8), 956–970.

(3)   Jafari Nodoushan, E.; Yi, T.; Lee, Y. J.; Kim, N. Wormlike Micellar Solutions, Beyond the Chemical Enhanced Oil Recovery Restrictions. *Fluids* **2019**, *4* (3), 173.

(4)   Yekeen, N.; Padmanabhan, E.; Idris, A. K.; Chauhan, P. S. Nanoparticles Applications for Hydraulic Fracturing of Unconventional Reservoirs: A Comprehensive Review of Recent Advances and Prospects. *Journal of Petroleum Science and Engineering* **2019**, *178*, 41–73.

(5)   Cai, S.; Vijayan, K.; Cheng, D.; Lima, E. M.; Discher, D. E. Micelles of Different Morphologies—Advantages of Worm-like Filomicelles of PEO-PCL in Paclitaxel Delivery. *Pharmaceutical Research* **2007**, *24* (11), 2099–2109.

(6)   Geng, Y.; Dalhaimer, P.; Cai, S.; Tsai, R.; Tewari, M.; Minko, T.; Discher, D. E. Shape Effects of Filaments versus Spherical Particles in Flow and Drug Delivery. *Nature Nanotechnology* **2007**, *2* (4), 249–255.

(7)   Berret, J.-F. Rheology of Wormlike Micelles: Equilibrium Properties and Shear Banding Transitions. In *Molecular Gels*; Weiss, R. G., Terech, P., Eds.; Springer-Verlag: Berlin/Heidelberg, 2006; pp 667–720.

(8)   Israelachvili, J.; Ladyzhinski, I. The Physico-Chemical Basis of Self-Assembling Structures. In *Forces, Growth and Form in Soft Condensed Matter: At the Interface between Physics and Biology*; Skjeltorp, A. T., Belushkin, A. V., Eds.; Kluwer Academic Publishers: Dordrecht, 2005; Vol. 160, pp 1–28.

(9)   Ben-Shaul, A.; May, S. Molecular Packing in Cylindrical Micelles. In *Giant Micelles*; Kaler, E., Zana, R., Eds.; CRC Press, 2007; Vol. 20074445, pp 41–79.

(10) Candau, S. J.; Hirsch, E.; Zana, R.; Adam, M. Network Properties of Semidilute Aqueous KBr Solutions of Cetyltrimethylammonium Bromide. *Journal of Colloid and Interface Science* **1988**, *122* (2), 430–440.

(11) Brown, W.; Johansson, K.; Almgren, M. Threadlike Micelles from Cetyltrimethylammonium Bromide in Aqueous Sodium Naphthalenesulfonate Solutions Studied by Static and Dynamic Light Scattering. *The Journal of Physical Chemistry* **1989**, *93* (15), 5888–5894.

(12) Quirion, F.; Magid, L. J. Growth and Counterion Binding of Cetyltrimethylammonium Bromide Aggregates at 25.Degree.C: A Neutron and Light Scattering Study. *The Journal of Physical Chemistry* **1986**, *90* (21), 5435–5441.

(13) Imae, T.; Ikeda, S. Characteristics of Rod-like Micelles of Cetyltrimethylammonium Chloride in Aqueous NaCl Solutions: Their Flexibility and the Scaling Laws in Dilute and Semidilute Regimes. *Colloid & Polymer Science* **1987**, *265* (12), 1090–1098.

(14) Candau, S. J.; Oda, R. Linear Viscoelasticity of Salt-Free Wormlike Micellar Solutions. *Colloids and Surfaces A: Physicochemical and Engineering Aspects* **2001**, *183–185*, 5–14.

(15) Magid, L. J. The Surfactant−Polyelectrolyte Analogy. *The Journal of Physical Chemistry B* **1998**, *102* (21), 4064–4074.

(16) Ezrahi, S.; Tuval, E.; Aserin, A. Properties, Main Applications and Perspectives of Worm Micelles. *Advances in Colloid and Interface Science* **2006**, *128–130*, 77–102.

(17) Cates, M. E.; Candau, S. J. Statics and Dynamics of Worm-like Surfactant Micelles. *Journal of Physics: Condensed Matter* **1990**, *2* (33), 6869–6892.

(18) In, M.; Aguerre-Chariol, O.; Zana, R. Closed-Looped Micelles in Surfactant Tetramer Solutions. *The Journal of Physical Chemistry B* **1999**, *103* (37), 7747–7750.

(19) Yu, H.; Jiang, W. Effect of Shear Flow on the Formation of Ring-Shaped ABA Amphiphilic Triblock Copolymer Micelles. *Macromolecules* **2009**, *42* (9), 3399–3404.

(20) Zhu, J.; Liao, Y.; Jiang, W. Ring-Shaped Morphology of "Crew-Cut" Aggregates from ABA Amphiphilic Triblock Copolymer in a Dilute Solution. *Langmuir* **2004**, *20* (9), 3809–3812.

(21) Pochan, D. J. Toroidal Triblock Copolymer Assemblies. *Science* **2004**, *306* (5693), 94–97.

(22)   Cates, M. E.; Fielding, S. M. Rheology of Giant Micelles. *Advances in Physics* **2006**, *55* (7–8), 799–879.

(23)   Sarmiento-Gomez, E.; Lopez-Diaz, D.; Castillo, R. Microrheology and Characteristic Lengths in Wormlike Micelles Made of a Zwitterionic Surfactant and SDS in Brine. *The Journal of Physical Chemistry B* **2010**, *114* (38), 12193–12202.

(24)   Lequeux, F. Structure and Rheology of Wormlike Micelles. *Current Opinion in Colloid & Interface Science* **1996**, *1* (3), 341–344.

(25)   Nagarajan, R.; Shah, K. M.; Hammond, S. Viscometric Detection of Sphere to Cylinder Transition and Polydispersity in Aqueous Micellar Solutions. *Colloids and Surfaces* **1982**, *4* (2), 147–162.

(26)   Clausen, T. M.; Vinson, P. K.; Minter, J. R.; Davis, H. T.; Talmon, Y.; Miller, W. G. Viscoelastic Micellar Solutions: Microscopy and Rheology. *The Journal of Physical Chemistry* **1992**, *96* (1), 474–484.

(27)   Lutz-Bueno, V.; Pasquino, R.; Liebi, M.; Kohlbrecher, J.; Fischer, P. Viscoelasticity Enhancement of Surfactant Solutions Depends on Molecular Conformation: Influence of Surfactant Headgroup Structure and Its Counterion. *Langmuir* **2016**, *32* (17), 4239–4250.

(28)   Zhao, M.; Yan, Z.; Dai, C.; Du, M.; Li, H.; Zhao, Y.; Wang, K.; Ding, Q. Formation and Rheological Properties of Wormlike Micelles by N-Hexadecyl-N-Methylpiperidinium Bromide and Sodium Salicylate. *Colloid and Polymer Science* **2015**, *293* (4), 1073–1082.

(29)   Shrestha, R. G.; Abezgauz, L.; Danino, D.; Sakai, K.; Sakai, H.; Abe, M. Structure and Dynamics of Poly(Oxyethylene) Cholesteryl Ether Wormlike Micelles: Rheometry, SAXS, and Cryo-TEM Studies. *Langmuir* **2011**, *27* (21), 12877–12883.

(30)   Pleines, M.; Kunz, W.; Zemb, T.; Benczédi, D.; Fieber, W. Molecular Factors Governing the Viscosity Peak of Giant Micelles in the Presence of Salt and Fragrances. *Journal of Colloid and Interface Science* **2019**, *537*, 682–693.

(31)   de Gennes, P. G. Reptation of a Polymer Chain in the Presence of Fixed Obstacles. *The Journal of Chemical Physics* **1971**, *55* (2), 572–579.

(32)   Cates, M. E. Dynamics of Living Polymers and Flexible Surfactant Micelles : Scaling Laws for Dilution. *Journal de Physique* **1988**, *49* (9), 1593–1600.

(33)   Lequeux, F. Reptation of Connected Wormlike Micelles. *Europhysics Letters (EPL)* **1992**, *19* (8), 675–681.

(34)   Cates, M. E. Reptation of Living Polymers: Dynamics of Entangled Polymers in the Presence of Reversible Chain-Scission Reactions. *Macromolecules* **1987**, *20* (9), 2289–2296.

(35)   Rehage, H.; Hoffmann, H. Viscoelastic Surfactant Solutions: Model Systems for Rheological Research. *Molecular Physics* **1991**, *74* (5), 933–973.

(36)   Rouse, P. E. A Theory of the Linear Viscoelastic Properties of Dilute Solutions of Coiling Polymers. *The Journal of Chemical Physics* **1953**, *21* (7), 1272–1280.

(37)   Granek, R.; Cates, M. E. Stress Relaxation in Living Polymers: Results from a Poisson Renewal Model. *The Journal of Chemical Physics* **1992**, *96* (6), 4758–4767.

(38)   Zhao, M.; Zhang, Y.; Zou, C.; Dai, C.; Gao, M.; Li, Y.; Lv, W.; Jiang, J.; Wu, Y. Can More Nanoparticles Induce Larger Viscosities of Nanoparticle-Enhanced Wormlike Micellar System (NEWMS)? *Materials* **2017**, *10* (9), 1096.

(39)   Berret, J. F.; Appell, J.; Porte, G. Linear Rheology of Entangled Wormlike Micelles. *Langmuir* **1993**, *9* (11), 2851–2854.

(40)   Spenley, N. A.; Cates, M. E.; McLeish, T. C. B. Nonlinear Rheology of Wormlike Micelles. *Physical Review Letters* **1993**, *71* (6), 939–942.

(41)   Berret, J.-F.; Porte, G.; Decruppe, J.-P. Inhomogeneous Shear Flows of Wormlike Micelles:MA Master Dynamic Phase Diagram. *Physical Review E* **1997**, *55* (2), 1668–1676.

(42)   Berret, J.-F. Transient Rheology of Wormlike Micelles. *Langmuir* **1997**, *13* (8), 2227–2234.

(43)   Champion, J. A.; Mitragotri, S. Role of Target Geometry in Phagocytosis. *Proceedings of the National Academy of Sciences* **2006**, *103* (13), 4930–4934.

(44)   Champion, J. A.; Mitragotri, S. Shape Induced Inhibition of Phagocytosis of Polymer Particles. *Pharmaceutical Research* **2009**, *26* (1), 244–249.

(45)   Simone, E. A.; Dziubla, T. D.; Muzykantov, V. R. Polymeric Carriers: Role of Geometry in Drug Delivery. *Expert Opinion on Drug Delivery* **2008**, *5* (12), 1283–1300.

(46) Venkataraman, S.; Hedrick, J. L.; Ong, Z. Y.; Yang, C.; Ee, P. L. R.; Hammond, P. T.; Yang, Y. Y. The Effects of Polymeric Nanostructure Shape on Drug Delivery. *Advanced Drug Delivery Reviews* **2011**, *63* (14–15), 1228–1246.

(47) Truong, N. P.; Whittaker, M. R.; Mak, C. W.; Davis, T. P. The Importance of Nanoparticle Shape in Cancer Drug Delivery. *Expert Opinion on Drug Delivery* **2015**, *12* (1), 129–142.

(48) Pawłowska, S.; Kowalewski, T. A.; Pierini, F. Fibrous Polymer Nanomaterials for Biomedical Applications and Their Transport by Fluids: An Overview. *Soft Matter* **2018**, *14* (42), 8421–8444.

(49) Li, W.; Zhang, X.; Hao, X.; Jie, J.; Tian, B.; Zhang, X. Shape Design of High Drug Payload Nanoparticles for More Effective Cancer Therapy. *Chem. Commun.* **2013**, *49* (93), 10989.

(50) Qin, S.-Y.; Cheng, Y.-J.; Jiang, Z.-W.; Ma, Y.-H.; Zhang, A.-Q. Morphology Control of Self-Deliverable Nanodrug with Enhanced Anticancer Efficiency. *Colloids and Surfaces B: Biointerfaces* **2018**, *165*, 345–354.

(51) Sun, X.; Liu, X.; Li, C.; Wang, Y.; Liu, L.; Su, F.; Li, S. Self-Assembled Micelles Prepared from Poly(ε-Caprolactone)-Poly(Ethylene Glycol) and Poly(ε-Caprolactone/Glycolide)-Poly(Ethylene Glycol) Block Copolymers for Sustained Drug Delivery. *Journal of Applied Polymer Science* **2018**, *135* (9), 45732.

(52) Gharebaghi, F.; Dalali, N.; Ahmadi, E.; Danafar, H. Preparation of Wormlike Polymeric Nanoparticles Coated with Silica for Delivery of Methotrexate and Evaluation of Anticancer Activity against MCF7 Cells. *Journal of Biomaterials Applications* **2017**, *31* (9), 1305–1316.

(53) Nair, P. R.; Karthick, S.; Spinler, K. R.; Vakili, M. R.; Lavasanifar, A.; Discher, D. E. Filomicelles from Aromatic Diblock Copolymers Increase Paclitaxel-Induced Tumor Cell Death and Aneuploidy Compared with Aliphatic Copolymers. *Nanomedicine* **2016**, *11* (12), 1551–1569.

(54) Zhao, P.; Liu, L.; Feng, X.; Wang, C.; Shuai, X.; Chen, Y. Molecular Nanoworm with PCL Core and PEO Shell as a Non-Spherical Carrier for Drug Delivery. *Macromolecular Rapid Communications* **2012**, *33* (16), 1351–1355.

(55)   He, X.; Yu, H.; Bao, X.; Cao, H.; Yin, Q.; Zhang, Z.; Li, Y. PH-Responsive Wormlike Micelles with Sequential Metastasis Targeting Inhibit Lung Metastasis of Breast Cancer. *Advanced Healthcare Materials* **2016**, *5* (4), 439–448.

(56)   Jelonek, K.; Li, S.; Wu, X.; Kasperczyk, J.; Marcinkowski, A. Self-Assembled Filomicelles Prepared from Polylactide/Poly(Ethylene Glycol) Block Copolymers for Anticancer Drug Delivery. *International Journal of Pharmaceutics* **2015**, *485* (1–2), 357–364.

(57)   Jelonek, K.; Li, S.; Kasperczyk, J.; Wu, X.; Orchel, A. Effect of Polymer Degradation on Prolonged Release of Paclitaxel from Filomicelles of Polylactide/Poly(Ethylene Glycol) Block Copolymers. *Materials Science and Engineering: C* **2017**, *75*, 918–925.

(58)   Jelonek, K.; Li, S.; Kaczmarczyk, B.; Marcinkowski, A.; Orchel, A.; Musiał-Kulik, M.; Kasperczyk, J. Multidrug PLA-PEG Filomicelles for Concurrent Delivery of Anticancer Drugs—The Influence of Drug-Drug and Drug-Polymer Interactions on Drug Loading and Release Properties. *International Journal of Pharmaceutics* **2016**, *510* (1), 365–374.

(59)   Jelonek, K.; Kasperczyk, J.; Li, S.; Nguyen, T. H. N.; Orchel, A.; Chodurek, E.; Paduszyński, P.; Jaworska-Kik, M.; Chrobak, E.; Bębenek, E.; Boryczka, S.; Jarosz-Biej, M.; Smolarczyk, R.; Foryś, A. Bioresorbable Filomicelles for Targeted Delivery of Betulin Derivative-*In Vitro* Study. *International Journal of Pharmaceutics* **2019**, *557*, 43–52.

(60)   Yang, X.; Grailer, J. J.; Rowland, I. J.; Javadi, A.; Hurley, S. A.; Steeber, D. A.; Gong, S. Multifunctional SPIO/DOX-Loaded Wormlike Polymer Vesicles for Cancer Therapy and MR Imaging. *Biomaterials* **2010**, *31* (34), 9065–9073.

(61)   Sarkar, K.; Krishna Meka, S. R.; Madras, G.; Chatterjee, K. A Self-Assembling Polycationic Nanocarrier That Exhibits Exceptional Gene Transfection Efficiency. *RSC Advances* **2015**, *5* (111), 91619–91632.

(62)   Williford, J.-M.; Archang, M. M.; Minn, I.; Ren, Y.; Wo, M.; Vandermark, J.; Fisher, P. B.; Pomper, M. G.; Mao, H.-Q. Critical Length of PEG Grafts on LPEI/DNA Nanoparticles for Efficient *in Vivo* Delivery. *ACS Biomaterials Science & Engineering* **2016**, *2* (4), 567–578.

(63)   Wan, X.; Min, Y.; Bludau, H.; Keith, A.; Sheiko, S. S.; Jordan, R.; Wang, A. Z.; Sokolsky-Papkov, M.; Kabanov, A. V. Drug Combination Synergy in Worm-like Polymeric Micelles

Improves Treatment Outcome for Small Cell and Non-Small Cell Lung Cancer. *ACS Nano* **2018**, *12* (3), 2426–2439.

(64)   Yi, S.; Allen, S. D.; Liu, Y.-G.; Ouyang, B. Z.; Li, X.; Augsornworawat, P.; Thorp, E. B.; Scott, E. A. Tailoring Nanostructure Morphology for Enhanced Targeting of Dendritic Cells in Atherosclerosis. *ACS Nano* **2016**, *10* (12), 11290–11303.

(65)   Kim, T. H.; Mount, C. W.; Dulken, B. W.; Ramos, J.; Fu, C. J.; Khant, H. A.; Chiu, W.; Gombotz, W. R.; Pun, S. H. Filamentous, Mixed Micelles of Triblock Copolymers Enhance Tumor Localization of Indocyanine Green in a Murine Xenograft Model. *Molecular Pharmaceutics* **2012**, *9* (1), 135–143.

(66)   Aluri, S.; Pastuszka, M. K.; Moses, A. S.; MacKay, J. A. Elastin-Like Peptide Amphiphiles Form Nanofibers with Tunable Length. *Biomacromolecules* **2012**, *13* (9), 2645–2654.

(67)   Zhang, P.; Cheetham, A. G.; Lin, Y.; Cui, H. Self-Assembled Tat Nanofibers as Effective Drug Carrier and Transporter. *ACS Nano* **2013**, *7* (7), 5965–5977.

(68)   Webber, M. J.; Newcomb, C. J.; Bitton, R.; Stupp, S. I. Switching of Self-Assembly in a Peptide Nanostructure with a Specific Enzyme. *Soft Matter* **2011**, *7* (20), 9665.

(69)   Soukasene, S.; Toft, D. J.; Moyer, T. J.; Lu, H.; Lee, H.-K.; Standley, S. M.; Cryns, V. L.; Stupp, S. I. Antitumor Activity of Peptide Amphiphile Nanofiber-Encapsulated Camptothecin. *ACS Nano* **2011**, *5* (11), 9113–9121.

(70)   So, M. M.; Mansukhani, N. A.; Peters, E. B.; Albaghdadi, M. S.; Wang, Z.; Rubert Pérez, C. M.; Kibbe, M. R.; Stupp, S. I. Peptide Amphiphile Nanostructures for Targeting of Atherosclerotic Plaque and Drug Delivery. *Advanced Biosystems* **2018**, *2* (3), 1700123.

(71)   Kim, J.-K.; Anderson, J.; Jun, H.-W.; Repka, M. A.; Jo, S. Self-Assembling Peptide Amphiphile-Based Nanofiber Gel for Bioresponsive Cisplatin Delivery. *Molecular Pharmaceutics* **2009**, *6* (3), 978–985.

(72)   Esser, L.; Truong, N. P.; Karagoz, B.; Moffat, B. A.; Boyer, C.; Quinn, J. F.; Whittaker, M. R.; Davis, T. P. Gadolinium-Functionalized Nanoparticles for Application as Magnetic Resonance Imaging Contrast Agents *via* Polymerization-Induced Self-Assembly. *Polym. Chem.* **2016**, *7* (47), 7325–7337.

(73)   Zhou, M.; Zhang, X.; Yang, Y.; Liu, Z.; Tian, B.; Jie, J.; Zhang, X. Carrier-Free Functionalized Multidrug Nanorods for Synergistic Cancer Therapy. *Biomaterials* **2013**, *34* (35), 8960–8967.

(74)   Baldelli Bombelli, F.; Berti, D.; Keiderling, U.; Baglioni, P. Living Polynucleotides Formed by the Spontaneous Aggregation of Dilauroylphosphonucleosides. *Applied Physics A: Materials Science & Processing* **2002**, *74* (0), s1270–s1273.

(75)   Bombelli, F. B.; Berti, D.; Pini, F.; Keiderling, U.; Baglioni, P. Flexibility of Dilauroyl-Phosphatidyl-Nucleoside Wormlike Micelles in Aqueous Solutions. *The Journal of Physical Chemistry B* **2004**, *108* (42), 16427–16434.

(76)   Bombelli, F. B.; Berti, D.; Almgren, M.; Karlsson, G.; Baglioni, P. Light Scattering and Cryo-Transmission Electron Microscopy Investigation of the Self-Assembling Behavior of Di-C $_{12}$ P-Nucleosides in Solution. *The Journal of Physical Chemistry B* **2006**, *110* (35), 17627–17637.

(77)   Liu, J.; Ma, N.; Zhao, D.; Li, Z.; Luan, Y. Spiral Assembly of Amphiphilic Cytarabine Prodrug Assisted by Probe Sonication: Enhanced Therapy Index for Leukemia. *Colloids and Surfaces B: Biointerfaces* **2015**, *136*, 918–927.

(78)   Liu, J.; Liu, J.; Zhao, D.; Ma, N.; Luan, Y. Highly Enhanced Leukemia Therapy and Oral Bioavailability from a Novel Amphiphilic Prodrug of Cytarabine. *RSC Adv.* **2016**, *6* (42), 35991–35999.

(79)   Zhang, J.; Zhang, D.; Hu, X.; Liu, R.; Li, Z.; Luan, Y. Rational Design of a New Cytarabine-Based Prodrug for Highly Efficient Oral Delivery of Cytarabine. *RSC Advances* **2018**, *8* (24), 13103–13111.

(80)   Mougin, J.; Yesylevskyy, S. O.; Bourgaux, C.; Chapron, D.; Michel, J.-P.; Dosio, F.; Stella, B.; Ramseyer, C.; Couvreur, P. Stacking as a Key Property for Creating Nanoparticles with Tunable Shape: The Case of Squalenoyl-Doxorubicin. *ACS Nano* **2019**, acsnano.9b05303.

(81)   Fan, Q.; Ji, Y.; Wang, J.; Wu, L.; Li, W.; Chen, R.; Chen, Z. Self-Assembly Behaviours of Peptide–Drug Conjugates: Influence of Multiple Factors on Aggregate Morphology and Potential Self-Assembly Mechanism. *R. Soc. open sci.* **2018**, *5* (4), 172040.

(82)   Cheetham, A. G.; Zhang, P.; Lin, Y.; Lock, L. L.; Cui, H. Supramolecular Nanostructures Formed by Anticancer Drug Assembly. *Journal of the American Chemical Society* **2013**, *135* (8), 2907–2910.

(83)   Cheetham, A. G.; Zhang, P.; Lin, Y.-A.; Lin, R.; Cui, H. Synthesis and Self-Assembly of a Mikto-Arm Star Dual Drug Amphiphile Containing Both Paclitaxel and Camptothecin. *J. Mater. Chem. B* **2014**, *2* (42), 7316–7326.

(84)   Zhang, D.; Qi, G.-B.; Zhao, Y.-X.; Qiao, S.-L.; Yang, C.; Wang, H. In Situ Formation of Nanofibers from Purpurin18-Peptide Conjugates and the Assembly Induced Retention Effect in Tumor Sites. *Advanced Materials* **2015**, *27* (40), 6125–6130.

(85)   Yang, M.; Xu, D.; Jiang, L.; Zhang, L.; Dustin, D.; Lund, R.; Liu, L.; Dong, H. Filamentous Supramolecular Peptide–Drug Conjugates as Highly Efficient Drug Delivery Vehicles. *Chem. Commun.* **2014**, *50* (37), 4827–4830.

(86)   Ji, Y.; Xiao, Y.; Xu, L.; He, J.; Qian, C.; Li, W.; Wu, L.; Chen, R.; Wang, J.; Hu, R.; Zhang, X.; Gu, Z.; Chen, Z. Drug-Bearing Supramolecular MMP Inhibitor Nanofibers for Inhibition of Metastasis and Growth of Liver Cancer. *Advanced Science* **2018**, *5* (8), 1700867.

(87)   Lin, R.; Cheetham, A. G.; Zhang, P.; Lin, Y.; Cui, H. Supramolecular Filaments Containing a Fixed 41% Paclitaxel Loading. *Chemical Communications* **2013**, *49* (43), 4968.

(88)   Matson, J. B.; Stupp, S. I. Drug Release from Hydrazone-Containing Peptide Amphiphiles. *Chemical Communications* **2011**, *47* (28), 7962.

(89)   Zhang, Z.; Yu, J.; Zhou, Y.; Zhang, R.; Song, Q.; Lei, L.; Li, X. Supramolecular Nanofibers of Dexamethasone Derivatives to Form Hydrogel for Topical Ocular Drug Delivery. *Colloids and Surfaces B: Biointerfaces* **2018**, *164*, 436–443.

(90)   Song, Q.; Zhang, R.; Lei, L.; Li, X. Self-Assembly of Succinated Paclitaxel into Supramolecular Hydrogel for Local Cancer Chemotherapy. *Journal of Biomedical Nanotechnology* **2018**, *14* (8), 1471–1476.

(91)   Yang, L.; Zhang, C.; Ren, C.; Liu, J.; Zhang, Y.; Wang, J.; Huang, F.; Zhang, L.; Liu, J. Supramolecular Hydrogel Based on Chlorambucil and Peptide Drug for Cancer Combination Therapy. *ACS Appl. Mater. Interfaces* **2019**, *11* (1), 331–339.

(92)   Gao, Y.; Kuang, Y.; Guo, Z.-F.; Guo, Z.; Krauss, I. J.; Xu, B. Enzyme-Instructed Molecular Self-Assembly Confers Nanofibers and a Supramolecular Hydrogel of Taxol Derivative. *J. Am. Chem. Soc.* **2009**, *131* (38), 13576–13577.

(93)   Barua, S.; Mitragotri, S. Synergistic Targeting of Cell Membrane, Cytoplasm, and Nucleus of Cancer Cells Using Rod-Shaped Nanoparticles. *ACS Nano* **2013**, *7* (11), 9558–9570.

(94)   Ma, M.; Xing, P.; Xu, S.; Li, S.; Chu, X.; Hao, A. Reversible PH-Responsive Helical Nanoribbons Formed Using Camptothecin. *RSC Adv.* **2014**, *4* (80), 42372–42375.

(95)   Wen, Y.; Zhang, W.; Gong, N.; Wang, Y.-F.; Guo, H.-B.; Guo, W.; Wang, P. C.; Liang, X.-J. Carrier-Free, Self-Assembled Pure Drug Nanorods Composed of 10-Hydroxycamptothecin and Chlorin E6 for Combinatorial Chemo-Photodynamic Antitumor Therapy *in Vivo*. *Nanoscale* **2017**, *9* (38), 14347–14356.

(96)   Zhou, Z.; Piao, Y.; Hao, L.; Wang, G.; Zhou, Z.; Shen, Y. Acidity-Responsive Shell-Sheddable Camptothecin-Based Nanofibers for Carrier-Free Cancer Drug Delivery. *Nanoscale* **2019**, *11* (34), 15907–15916.

(97)   Kasai, H.; Murakami, T.; Ikuta, Y.; Koseki, Y.; Baba, K.; Oikawa, H.; Nakanishi, H.; Okada, M.; Shoji, M.; Ueda, M.; Imahori, H.; Hashida, M. Creation of Pure Nanodrugs and Their Anticancer Properties. *Angew. Chem. Int. Ed.* **2012**, *51* (41), 10315–10318.

(98)   Christian, D. A.; Cai, S.; Garbuzenko, O. B.; Harada, T.; Zajac, A. L.; Minko, T.; Discher, D. E. Flexible Filaments for *in Vivo* Imaging and Delivery: Persistent Circulation of Filomicelles Opens the Dosage Window for Sustained Tumor Shrinkage. *Molecular Pharmaceutics* **2009**, *6* (5), 1343–1352.

(99)   Loverde, S. M.; Klein, M. L.; Discher, D. E. Nanoparticle Shape Improves Delivery: Rational Coarse Grain Molecular Dynamics (RCG-MD) of Taxol in Worm-Like PEG-PCL Micelles. *Advanced Materials* **2012**, *24* (28), 3823–3830.

(100)   Zhou, Z.; Ma, X.; Jin, E.; Tang, J.; Sui, M.; Shen, Y.; Van Kirk, E. A.; Murdoch, W. J.; Radosz, M. Linear-Dendritic Drug Conjugates Forming Long-Circulating Nanorods for Cancer-Drug Delivery. *Biomaterials* **2013**, *34* (22), 5722–5735.

(101)   Karagoz, B.; Esser, L.; Duong, H. T.; Basuki, J. S.; Boyer, C.; Davis, T. P. Polymerization-Induced Self-Assembly (PISA)-Control over the Morphology of Nanoparticles for Drug Delivery Applications. *Polym. Chem.* **2014**, *5* (2), 350–355.

(102)   Zhou, M.; Zhang, X.; Yu, C.; Nan, X.; Chen, X.; Zhang, X. Shape Regulated Anticancer Activities and Systematic Toxicities of Drug Nanocrystals *in Vivo*. *Nanomedicine: Nanotechnology, Biology and Medicine* **2016**, *12* (1), 181–189.

(103)   Li, Y.; Lin, J.; Huang, Y.; Li, Y.; Yang, X.; Wu, H.; Wu, S.; Xie, L.; Dai, L.; Hou, Z. Self-Targeted, Shape-Assisted, and Controlled-Release Self-Delivery Nanodrug for Synergistic Targeting/Anticancer Effect of Cytoplasm and Nucleus of Cancer Cells. *ACS Appl. Mater. Interfaces* **2015**, *7* (46), 25553–25559.

(104)   Wang, Y.; Wang, D.; Fu, Q.; Liu, D.; Ma, Y.; Racette, K.; He, Z.; Liu, F. Shape-Controlled Paclitaxel Nanoparticles with Multiple Morphologies: Rod-Shaped, Worm-Like, Spherical, and Fingerprint-Like. *Molecular Pharmaceutics* **2014**, *11* (10), 3766–3771.

(105)   Truong, N. P.; Quinn, J. F.; Whittaker, M. R.; Davis, T. P. Polymeric Filomicelles and Nanoworms: Two Decades of Synthesis and Application. *Polym. Chem.* **2016**, *7* (26), 4295–4312.

(106)   Shen, X.; Liu, X.; Li, R.; Yun, P.; Li, C.; Su, F.; Li, S. Biocompatibility of Filomicelles Prepared from Poly(Ethylene Glycol)-Polylactide Diblock Copolymers as Potential Drug Carrier. *Journal of Biomaterials Science, Polymer Edition* **2017**, *28* (15), 1677–1694.

(107)   Lee, J. H.; Kopecek, J.; Andrade, J. D. Protein-Resistant Surfaces Prepared by PEO-Containing Block Copolymer Surfactants. *Journal of Biomedical Materials Research* **1989**, *23* (3), 351–368.

(108)   Oltra, N. S.; Swift, J.; Mahmud, A.; Rajagopal, K.; Loverde, S. M.; Discher, D. E. Filomicelles in Nanomedicine-from Flexible, Fragmentable, and Ligand-Targetable Drug Carrier Designs to Combination Therapy for Brain Tumors. *Journal of Materials Chemistry B* **2013**, *1* (39), 5177.

(109)   Yu, H.; Xu, Z.; Wang, D.; Chen, X.; Zhang, Z.; Yin, Q.; Li, Y. Intracellular PH-Activated PEG-b-PDPA Wormlike Micelles for Hydrophobic Drug Delivery. *Polymer Chemistry* **2013**, *4* (19), 5052.

(110)   Parker, N.; Turk, M. J.; Westrick, E.; Lewis, J. D.; Low, P. S.; Leamon, C. P. Folate Receptor Expression in Carcinomas and Normal Tissues Determined by a Quantitative Radioligand Binding Assay. *Analytical Biochemistry* **2005**, *338* (2), 284–293.

(111)   Lee, J. O.; Oh, K. T.; Kim, D.; Lee, E. S. PH-Sensitive Short Worm-like Micelles Targeting Tumors Based on the Extracellular PH. *J. Mater. Chem. B* **2014**, *2* (37), 6363–6370.

(112)   Trent, A.; Marullo, R.; Lin, B.; Black, M.; Tirrell, M. Structural Properties of Soluble Peptide Amphiphile Micelles. *Soft Matter* **2011**, *7* (20), 9572.

(113)   Paramonov, S. E.; Jun, H.-W.; Hartgerink, J. D. Self-Assembly of Peptide−Amphiphile Nanofibers: The Roles of Hydrogen Bonding and Amphiphilic Packing. *Journal of the American Chemical Society* **2006**, *128* (22), 7291–7298.

(114)   Shimada, T.; Lee, S.; Bates, F. S.; Hotta, A.; Tirrell, M. Wormlike Micelle Formation in Peptide-Lipid Conjugates Driven by Secondary Structure Transformation of the Headgroups [†]. *The Journal of Physical Chemistry B* **2009**, *113* (42), 13711–13714.

(115)   Shimada, T.; Sakamoto, N.; Motokawa, R.; Koizumi, S.; Tirrell, M. Self-Assembly Process of Peptide Amphiphile Worm-Like Micelles. *The Journal of Physical Chemistry B* **2012**, *116* (1), 240–243.

(116)   Webber, M. J.; Berns, E. J.; Stupp, S. I. Supramolecular Nanofibers of Peptide Amphiphiles for Medicine. *Israel Journal of Chemistry* **2013**, *53* (8), 530–554.

(117)   Temming, K.; Schiffelers, R. M.; Molema, G.; Kok, R. J. RGD-Based Strategies for Selective Delivery of Therapeutics and Imaging Agents to the Tumour Vasculature. *Drug Resistance Updates* **2005**, *8* (6), 381–402.

(118)   Cinar, G.; Ozdemir, A.; Hamsici, S.; Gunay, G.; Dana, A.; Tekinay, A. B.; Guler, M. O. Local Delivery of Doxorubicin through Supramolecular Peptide Amphiphile Nanofiber Gels. *Biomaterials Science* **2017**, *5* (1), 67–76.

(119)   Luo, C.; Sun, J.; Sun, B.; He, Z. Prodrug-Based Nanoparticulate Drug Delivery Strategies for Cancer Therapy. *Trends in Pharmacological Sciences* **2014**, *35* (11), 556–566.

(120)   Ma, W.; Cheetham, A. G.; Cui, H. Building Nanostructures with Drugs. *Nano Today* **2016**, *11* (1), 13–30.

(121)   Baldelli Bombelli, F.; Berti, D.; Keiderling, U.; Baglioni, P. Giant Polymerlike Micelles Formed by Nucleoside-Functionalized Lipids. *The Journal of Physical Chemistry B* **2002**, *106* (44), 11613–11621.

(122)   Maksimenko, A.; Dosio, F.; Mougin, J.; Ferrero, A.; Wack, S.; Reddy, L. H.; Weyn, A.-A.; Lepeltier, E.; Bourgaux, C.; Stella, B.; Cattel, L.; Couvreur, P. A Unique Squalenoylated and Nonpegylated Doxorubicin Nanomedicine with Systemic Long-Circulating Properties and Anticancer Activity. *Proceedings of the National Academy of Sciences* **2014**, *111* (2), E217–E226.

(123)   Su, H.; Zhang, P.; Cheetham, A. G.; Koo, J. M.; Lin, R.; Masood, A.; Schiapparelli, P.; Quiñones-Hinojosa, A.; Cui, H. Supramolecular Crafting of Self-Assembling Camptothecin Prodrugs with Enhanced Efficacy against Primary Cancer Cells. *Theranostics* **2016**, *6* (7), 1065–1074.

(124)   Xiong, T.; Li, X.; Zhou, Y.; Song, Q.; Zhang, R.; Lei, L.; Li, X. Glycosylation-Enhanced Biocompatibility of the Supramolecular Hydrogel of an Anti-Inflammatory Drug for Topical Suppression of Inflammation. *Acta Biomaterialia* **2018**, *73*, 275–284.

(125)   Zhou, Y.; Lei, L.; Zhang, Z.; Zhang, R.; Song, Q.; Li, X. Cation Instructed Steroidal Prodrug Supramolecular Hydrogel. *Journal of Colloid and Interface Science* **2018**, *528*, 10–17.

(126)   Couvreur, P.; Stella, B.; Reddy, L. H.; Hillaireau, H.; Dubernet, C.; Desmaële, D.; Lepêtre-Mouelhi, S.; Rocco, F.; Dereuddre-Bosquet, N.; Clayette, P.; Rosilio, V.; Marsaud, V.; Renoir, J.-M.; Cattel, L. Squalenoyl Nanomedicines as Potential Therapeutics. *Nano Letters* **2006**, *6* (11), 2544–2548.

(127)   Kotelevets, L.; Chastre, E.; Caron, J.; Mougin, J.; Bastian, G.; Pineau, A.; Walker, F.; Lehy, T.; Desmaële, D.; Couvreur, P. A Squalene-Based Nanomedicine for Oral Treatment of Colon Cancer. *Cancer Research* **2017**, *77* (11), 2964–2975.

(128) Sobot, D.; Mura, S.; Yesylevskyy, S. O.; Dalbin, L.; Cayre, F.; Bort, G.; Mougin, J.; Desmaële, D.; Lepetre-Mouelhi, S.; Pieters, G.; Andreiuk, B.; Klymchenko, A. S.; Paul, J.-L.; Ramseyer, C.; Couvreur, P. Conjugation of Squalene to Gemcitabine as Unique Approach Exploiting Endogenous Lipoproteins for Drug Delivery. *Nature Communications* **2017**, *8*, 15678.

(129) Gaudin, A.; Yemisci, M.; Eroglu, H.; Lepetre-Mouelhi, S.; Turkoglu, O. F.; Dönmez-Demir, B.; Caban, S.; Sargon, M. F.; Garcia-Argote, S.; Pieters, G.; Loreau, O.; Rousseau, B.; Tagit, O.; Hildebrandt, N.; Le Dantec, Y.; Mougin, J.; Valetti, S.; Chacun, H.; Nicolas, V.; Desmaële, D.; *et al.* Squalenoyl Adenosine Nanoparticles Provide Neuroprotection after Stroke and Spinal Cord Injury. *Nature Nanotechnology* **2014**, *9* (12), 1054–1062.

(130) Feng, J.; Lepetre-Mouelhi, S.; Gautier, A.; Mura, S.; Cailleau, C.; Coudore, F.; Hamon, M.; Couvreur, P. A New Painkiller Nanomedicine to Bypass the Blood-Brain Barrier and the Use of Morphine. *Sci. Adv.* **2019**, *5* (2), eaau5148.

(131) Wang, Y.; Cheetham, A. G.; Angacian, G.; Su, H.; Xie, L.; Cui, H. Peptide–Drug Conjugates as Effective Prodrug Strategies for Targeted Delivery. *Advanced Drug Delivery Reviews* **2017**, *110–111*, 112–126.

(132) Kang, M.; Zhang, P.; Cui, H.; Loverde, S. M. π–π Stacking Mediated Chirality in Functional Supramolecular Filaments. *Macromolecules* **2016**, *49* (3), 994–1001.

(133) Cheetham, A. G.; Ou, Y.-C.; Zhang, P.; Cui, H. Linker-Determined Drug Release Mechanism of Free Camptothecin from Self-Assembling Drug Amphiphiles. *Chem. Commun.* **2014**, *50* (45), 6039–6042.

(134) Webber, M. J.; Matson, J. B.; Tamboli, V. K.; Stupp, S. I. Controlled Release of Dexamethasone from Peptide Nanofiber Gels to Modulate Inflammatory Response. *Biomaterials* **2012**, *33* (28), 6823–6832.

(135) Das, S.; Horo, H.; Goswami, U.; Kundu, L. M. Synthesis of a Peptide Conjugated 5-Fluorouracil Gelator Prodrug for Photo-Controlled Release of the Antitumor Agent. *ChemistrySelect* **2019**, *4* (22), 6778–6783.

(136) Li, J.; Gao, Y.; Kuang, Y.; Shi, J.; Du, X.; Zhou, J.; Wang, H.; Yang, Z.; Xu, B. Dephosphorylation of D-Peptide Derivatives to Form Biofunctional, Supramolecular Nanofibers/Hydrogels and Their Potential Applications for Intracellular Imaging and Intratumoral Chemotherapy. *J. Am. Chem. Soc.* **2013**, *135* (26), 9907–9914.

(137) Chakroun, R. W.; Wang, F.; Lin, R.; Wang, Y.; Su, H.; Pompa, D.; Cui, H. Fine-Tuning the Linear Release Rate of Paclitaxel-Bearing Supramolecular Filament Hydrogels through Molecular Engineering. *ACS Nano* **2019**.

(138) Henne, W. A.; Doorneweerd, D. D.; Hilgenbrink, A. R.; Kularatne, S. A.; Low, P. S. Synthesis and Activity of a Folate Peptide Camptothecin Prodrug. *Bioorganic & Medicinal Chemistry Letters* **2006**, *16* (20), 5350–5355.

(139) Qin, S.-Y.; Peng, M.-Y.; Rong, L.; Li, B.; Wang, S.-B.; Cheng, S.-X.; Zhuo, R.-X.; Zhang, X.-Z. Self-Defensive Nano-Assemblies from Camptothecin-Based Antitumor Drugs. *Regen Biomater* **2015**, *2* (3), 159–166.

(140) Bala, V.; Rao, S.; Boyd, B. J.; Prestidge, C. A. Prodrug and Nanomedicine Approaches for the Delivery of the Camptothecin Analogue SN38. *Journal of Controlled Release* **2013**, *172* (1), 48–61.

(141) Zhao, H.; Lee, C.; Sai, P.; Choe, Y. H.; Boro, M.; Pendri, A.; Guan, S.; Greenwald, R. B. 20-*O*-Acylcamptothecin Derivatives: Evidence for Lactone Stabilization. *J. Org. Chem.* **2000**, *65* (15), 4601–4606.

(142) Lerchen, H.-G.; Baumgarten, J.; von dem Bruch, K.; Lehmann, T. E.; Sperzel, M.; Kempka, G.; Fiebig, H.-H. Design and Optimization of 20-O-Linked Camptothecin Glycoconjugates as Anticancer Agents. *J. Med. Chem.* **2001**, *44* (24), 4186–4195.

(143) Li, Y.; Hu, X.; Zheng, X.; Liu, Y.; Liu, S.; Yue, Y.; Xie, Z. Self-Assembled Organic Nanorods for Dual Chemo-Photodynamic Therapies. *RSC Adv.* **2018**, *8* (10), 5493–5499.

Chapitre 2 : Article de recherche

Stacking as a key property for creating nanoparticles with tunable shape: the case of squalenoyl-doxorubicin

Julie Mougin[†], Semen O. Yesylevskyy[‡, ||], Claudie Bourgaux[†], David Chapron[†], Jean-Philippe Michel[†], Franco Dosio[§], Barbara Stella[§], Christophe Ramseyer[||], Patrick Couvreur,[†]*

[†]Institut Galien Paris-Sud UMR CNRS 8612, Faculty of Pharmacy, Univ. Paris-Sud, Université Paris-Saclay, 92290 Châtenay-Malabry, France

[‡]Department of Physics of Biological Systems, Institute of Physics of the National Academy of Sciences of Ukraine, Prospect Nauky 46, 03028 Kyiv, Ukraine

[§]Dipartimento di Scienza e Tecnologia del Farmaco, Università degli Studi di Torino, 10125 Turin, Italy

[||]Laboratoire Chrono Environnement UMR CNRS 6249, Université de Bourgogne Franche-Comté, 16 route de Gray, 25030 Besançon Cedex, France

69

Stacking as a key property for creating nanoparticles with tunable shape: the case of squalenoyl-doxorubicin
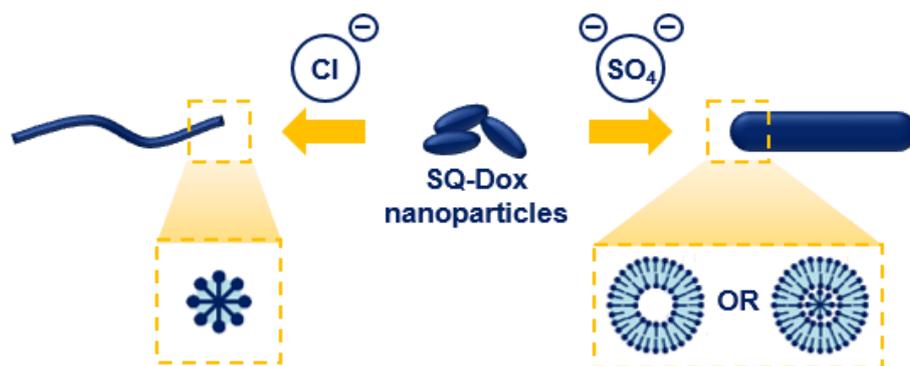
Abstract

The development of elongated nanoparticles (NPs) for drug delivery is of growing interest in recent years, due to longer blood circulation and improved efficacy compared to spherical counterparts. Squalenoyl-doxorubicin (SQ-Dox) conjugate was previously shown to form elongated NPs with improved therapeutic efficacy and decreased toxicity compared to free doxorubicin. By using experimental and computational techniques, we demonstrate here that the specific physical properties of SQ-Dox, which include stacking and electrostatic interactions of doxorubicin as well as hydrophobic interactions of squalene, are involved in the formation of nanoassemblies with diverse elongated structures. We show that SQ-Dox bioconjugate concentration, ionic strength, and anion nature can be used to modulate the shape and stiffness of SQ-Dox NPs. As those parameters are involved in nanoparticle behavior in biological media, these findings could bring interesting opportunities for drug delivery and serve as an example for the design of original nanodrugs with stacking properties tuned for particular clinical purposes.

I. Introduction

Doxorubicin (Dox) is a widely used anticancer drug presenting a broad spectrum of activity but limited by dose-dependent and irreversible cardiotoxicity.[1] To overcome this major drawback, we have previously conjugated the anticancer drug to squalene, a natural and biocompatible lipid, and it was found that the resulting bioconjugate was able to self-assemble into NPs in water. This nanomedicine displayed increased anticancer efficiency and decreased cardiotoxicity compared to free doxorubicin. This could be attributed to the elongated shape of squalenoyl-doxorubicin (SQ-Dox) NPs.[2] Long flexible cylindrical micelles, generally referred to as worm-like micelles or filomicelles, have been first used for therapeutic purposes by Discher *et al.* in the middle 2000's.[3,4] Interestingly, cylindrical paclitaxel-loaded poly(ethylene glycol)-poly(caprolactone) NPs were observed to exhibit an extended circulation time in mouse bloodstream compared to analogous spherical particles and a higher accumulation in xenograft tumors. Since then, increasing attention has been paid to the role of nanocarrier's shape for drug delivery. It has been revealed that beyond sustaining a long circulation time, elongated shape may favor margination (preferential migration of some NPs close to the vessel wall in the bloodstream), allowing an improved delivery to target tissues *via* the enhanced permeation and retention effect.[5] In addition, the nanoparticle rigidity may also impact the tumor accumulation: soft nanocarriers accumulate more in tumor tissues than the stiffer ones.[6,7] All these findings help considering worm-like NPs as promising nanomedicines with a high degree of adjustability.

As the majority of the efforts has been put on polymer worm-like NPs in recent years,[8–10] SQ-Dox is currently a simple nonpolymeric nanomedicine forming elongated nanostructures with confirmed therapeutic efficacy. But the mechanism allowing the formation of these worm-like structures remained completely unknown, and this has been extensively investigated in the current study. SQ-Dox molecule combines amphiphilic lipid-like properties with the net positive charge and strong stacking propensity of the Dox moiety, which makes it, indeed, an interesting model object for elucidating the role of these properties in the controllable formation of elongated NPs. The experimental and computational techniques were used complementary for all the steps of the nanoparticle formation, which allowed studying this process in detail. Herein, we show that stacking

interactions of Dox moieties play a major role in the self-assembling of elongated NPs and their aggregation and reshaping in solution. The role of the added anion concentration and valency is also highlighted, as a simple way to modulate the nanoparticle shape and rigidity. This could bring interesting opportunities to the drug delivery field by designing nanomedicines with controlled shape and structure.

II. Materials and methods

1. Materials

All solvents were purchased from Carlo-Erba (Val-de-Reuil, France), and doxorubicin and daunorubicin hydrochloride were purchased from APAC Pharmaceutical LLC (Ellicott City, MD). Squalene, doxorubicin hydrochloride, sodium acetate, sodium chloride and sodium sulfate were purchased from Sigma-Aldrich Chemical Co. (St. Quentin Fallavier, France), and TLC plates and silica gels for chromatography were purchased from Merck (Darmstadt, Germany).

2. Formulation and characterization of SQ-Dox nanoparticles

SQ-Dox was synthesized as described in **Supporting Information**. SQ-Dox NPs were prepared according to the nanoprecipitation process, adapted from Maksimenko *et al*.[2] Practically, SQ-Dox (2 mg) was solubilized into 500 μL THF and added dropwise in 1 mL H_2O under stirring (500 rpm) using a syringe pump with a flow rate of 130 μL min. THF was then removed by evaporation at 20 °C under vacuum to obtain a suspension of SQ-Dox NPs in water.

To study the influence of added salts, concentrated solutions were added to already prepared SQ-Dox nanoparticle suspensions. NaCl solutions were prepared at concentrations ranging from 200 to 800 mM. 2 μL of salt solution of appropriate concentration were added to 200 μL of SQ-Dox NPs in water prepared at concentrations ranging from 2 mM to 8 mM, to reach a final SQ-Dox:NaCl molar

ratio of 1:1. Na_2SO_4 solutions were prepared at concentrations ranging from 10 to 100 mM. 2 μL of salt solution of appropriate concentration were added to 200 μL of 2 mM SQ-Dox NPs in water to reach a final SQ-Dox:Na_2SO_4 molar ratio ranging from 20:1 to 2:1.

The ζ-potential was measured at 25 °C after 1:10 dilution of SQ-Dox NPs in 1 mM NaCl solution using a Zetasizer Nano ZS (Malvern Panalyticals).

3. Cryo-transmission electron microscopy

5 μL of SQ-Dox NPs at different concentrations (2 mM, 4 mM or 8 mM) in pure water or in the presence of salts (NaCl or Na_2SO_4 at molar ratios SQ-Dox:NaCl 1:1 or SQ-Dox:Na_2SO_4 20:1 to 2:1) were deposited onto a Lacey Formvar/carbon 300 mesh copper Grid (Ted Pella). The excess was manually blotted with a filter paper and the residual thin film was immediately frozen by plunging into liquid ethane cooled down at liquid nitrogen temperature using a Leica EM-CPC cryo-plunger. Observation was performed using a JEOL 2100HC microscope (JEOL Europe) or a JEOL 2200FS field emission microscope (JEOL USA) operating under an acceleration voltage of 200 kV in zero-loss mode (slit was 20 eV). High magnification images (2k x 2k pixels) were recorded by a CCD camera (Gatan Inc.) using Digital Micrograph software.

4. Atomic force microscopy

SQ-Dox NPs samples (2 mM SQ-Dox with NaCl 2 mM and 4 mM SQ-Dox in water) were diluted to 20 μM in water. 1 mL of this nanoparticle suspension was then deposited during 2 h onto a hydrophilic silicon surface previously treated with acidic piranha solution. AFM experiments were performed using the Nanowizard 3 Ultra Speed (JPK Instruments), installed on an air-buffered table coupled to a dynamic antivibration device, and enclosed in an acoustic box. Imaging of the surface morphology was performed in water in AC mode with gold-coated silicon cantilever MLCT of 0.6 ±

0.1 N.m^{-1} spring constant, 170 ± 5 kHz resonance frequency and 10 nm nominal radius of curvature (Bruker). The pyramid-shaped tips had a radius of curvature < 20 nm. A free amplitude oscillation of 15 nm was chosen allowing the best resolution of the imaged surface. Set points ranging between 75 % and 85 % of the free amplitude were used. Images were taken at scan rate of 1 Hz. Image processing (flatten, plane fit, edge and hole detection) was performed with the JPK Data Processing software (JPK Instruments). At least three different areas of each sample were scanned and typical images were presented.

5. Small angle X-ray scattering

SAXS experiments were performed on the SWING beamline at SOLEIL and on the BM29 beamline at ESRF. For measurements on the SWING beamline, samples were loaded into quartz capillaries (1.5 mm diameter). The scattering intensity I(q) was reported as a function of the scattering vector q = 4π sinθ / λ where 2θ is the scattering angle and λ the X-ray wavelength. Data were recorded at 12 keV in the scattering vector q-range 0.04 < q < 4 nm^{-1}, using a bi-dimensional Aviex detector. For each sample, 10 frames of 0.150 s were recorded at 20 °C and averaged. Water scattering was subtracted from the sample scattering. The beamline software Foxtrot was used for data collection and processing. On the BM29 beamline, samples were injected *via* an automated sample changer into a quartz capillary (1.8 mm internal diameter) and streamed at a constant flow rate through the capillary during beam exposure to avoid possible degradation under X-ray irradiation.[11] Data were recorded at 12.5 keV in the scattering vector q-range 0.04 < q < 5 nm^{-1}, using a Pilatus 1 M detector. For each sample 12 frames of 0.3 s were averaged and water scattering was measured before and after each sample.[12] The dedicated beamline software BsxCuBe was used for data collection, and data processing was carried out using EDNA software.[13] For all of the samples, the scattering intensity was normalized with respect to the incident beam intensity, acquisition time and sample transmission. Structural information was retrieved from the SAXS patterns using the SASfit program.[14]

6. Molecular dynamics force field

The topology of SQ-Dox was used from our previous study.[15] Initial topology of SQ-Dox was generated by Acpype topology generator.[16] The structure was optimized in Gaussian 09[17] at the B3LYP/6-31++G(d) level of theory. The ESP partial charges were computed and added to initial topology. The charges of topologically equivalent atoms were averaged. The charges of squalene moiety were set to zero except the linker between Dox and SQ. The atom types of SQ tails were adjusted to match lipids force field.

7. Construction of pre-arranged cylindrical aggregates

Cylindrical aggregates were also constructed from the pre-arrangement of SQ-Dox molecules in preferred orientation. This allowed a much simpler simulation setup, which could be easily used to generate several initial structures for independent simulations. 100 SQ-Dox molecules were arranged into 10 disks with the molecules in each disk oriented radially around z-axis with Dox moiety facing outside. The system was solvated with ~13,000 water molecules and either 100 Cl^- or 100 SO_4^{2-} and 50 Na^+ counter ions in such a way that the solvent did not penetrate into the region of the SQ tails. The system was equilibrated for 300 ns without any restraints.

8. Simulations of SQ-Dox bilayers.

In order to simulate the bilayer phase of SQ-Dox, the molecules were arranged into the monolayer at 7 x 7 grid in x,y plane with Dox moieties facing upwards. The second inverted monolayer was added, and the system was solvated with ~ 5,000 water molecules and the corresponding number of Cl^- counterions. No water molecules were placed into the region of SQ tails. The system was equilibrated for 300 ns without restraints. The area per molecule was used to monitor equilibration.

III. Results and discussion

1. Structure of SQ-Dox nanoparticles

SQ-Dox NPs were prepared by nanoprecipitation of a THF solution of SQ-Dox hydrochloride in water, as previously described.[2] Clear red suspension of NPs formed with a ζ-potential of ∼ +56 mV, arising from the positively charged ammonium group on the daunosamine sugar moiety of Dox. Cryo-TEM pictures of the 2 mM SQ-Dox NPs suspension revealed the presence of small quasi-spherical NPs with ∼5–6 nm diameter and only few long cylinders (**Figure 1a**). When increasing the concentration of SQ-Dox from 2 mM to 4 mM, cryo-TEM observations revealed the coexistence of short NPs and worm-like NPs with lengths up to microns (**Figures 1b** and **S1a**). In addition, some flexible NPs of diameter ∼5 nm seemed to assemble to form thicker ones of diameter ∼11.7 nm. Generally, it was observed that the number of long worm-like NPs increased when raising the SQ-Dox concentration. To investigate the reversibility of NPs elongation, 4 mM Sq-Dox NPs were diluted to 20 μM prior to atomic force microscopy (AFM) imaging. The obtained pictures showed that even when diluted, long worm-like NPs remained in the suspension (**Figure S1b, c**), which suggested that these elongated NPs were stable upon dilution.

Figure 1c displays the small-angle X-ray scattering (SAXS) patterns of nanoparticle suspensions depending on SQ-Dox concentration. The SAXS pattern of SQ-Dox suspensions at 2 mM concentration was modeled by core–shell prolate ellipsoids. The obtained lengths for short and long semiaxes were 2.3 ± 0.1 nm and 3.4 ± 0.1 nm, respectively, and the shell thickness was 1.1 ± 0.1 nm, in good agreement with cryo-TEM findings (**Figure 1a**). The SAXS patterns of more concentrated suspensions (4–15 mM) were characteristic of cylindrical NPs, as shown by the q^{-1} dependence of the scattered intensity I(q) at intermediate scattering vectors q ($q = 4\pi \sin \theta/\lambda$, where 2θ is the scattering angle and λ the X-ray wavelength).[18] In the high q region, short length scales were probed, and the curves reflected the structure of the nanoparticle cross-section. The intermediate and high q regions of the curves could be well described with a model of core–shell cylindrical aggregate, the core and the shell corresponding to the hydrophobic SQ chains and the hydrophilic Dox polar heads, respectively

(Figure 1d, e). Fitting of the SAXS curve resulted in a core radius of 2.2 ± 0.1 nm, matching the length of stretched SQ chains, and a shell thickness of 1.1 ± 0.1 nm. The fitting method is described in **Supporting Information**.
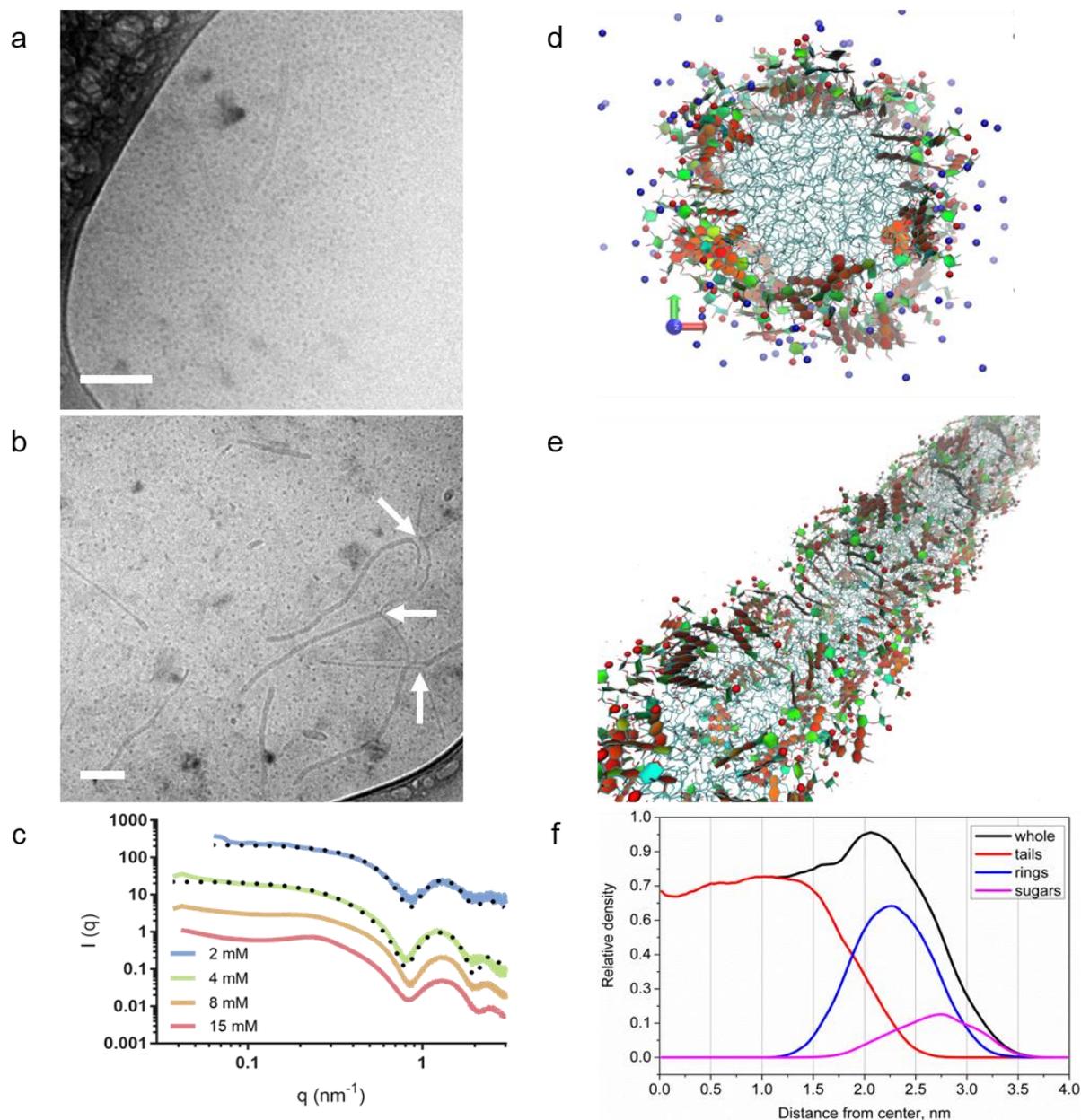

Figure 1. Structural characterization of SQ-Dox NPs **a, b.** Cryo-TEM micrographs of SQ-Dox NPs suspensions prepared at **a.** 2 mM (scale bar, 50 nm) and **b.** 4 mM of SQ-Dox in water. The arrows indicate the interaction sites between SQ-Dox thin cylinders (scale bar, 100 nm). **c.** Small-angle X-ray scattering pattern of SQ-Dox NPs in water. The plain lines represent experimental data, and the dotted lines are the corresponding fits. Curves are shifted along the y-axis for clarity. **d, e.** Snapshots of a cylindrical nanoparticle. SQ tails are shown as sticks. Aromatic rings are filled with red and orange, while nonaromatic rings are green and cyan. Positively charged NH_3^+ groups are shown as red spheres. Na^+ ions are blue spheres. Water is not shown for clarity. **d.** Front view. **e.** Perspective view. **f.** Radial density distribution (in dimensionless units) of the SQ chains and Dox heads in the cylindrical nanoparticle with Cl^- counterions.

The low q region contained information on the length and flexibility of the NPs. Those features are expected to depend on the bioconjugate concentration. When the concentration increased, elongated NPs tended to grow in order to minimize the excess of the free energy in the system by reducing the number of end-caps. Simultaneously, the rate of growth may be decreased by the electrostatic repulsions between charges along the nanoparticle body, favoring shorter NPs.[19,20] The SAXS pattern of the 4 mM suspension could be fitted by ∼18 nm-long cylinders.

The increase in I(q) at lowest q values suggested the coexistence of these majority NPs with long nanoassemblies. Upon aging, short cylinders evolved toward long worm-like NPs with $2l_p \sim 40$ nm, as shown by the SAXS curve recorded after 18 days **(Figure S2)**, where l_p is the persistence length, defined as the shortest scale over which a nanoparticle can be considered as a rigid rod.[19,20] Short l_p allows more flexibility, while cylinders rigidity increases for higher persistence lengths. For SQ-Dox concentration above 4 mM, the flattening in X-ray scattering intensity at low q and the broad maximum at about 0.24 nm^{-1}, indicative of a structure factor, emphasized the existence of repulsive interactions between NPs, with an average distance between cylinders d ∼ 26 nm. The interactions between NPs depend on the effective volume fraction and dimensions of the NPs. Due to the presence of charges, the diameter 2R of the NPs was increased to the effective value $2R + 2\lambda_D$, where λ_D is the Debye screening length accounting for the extent of the electrostatic repulsion. The volume of a nanoparticle of length l was increased to the effective volume $\pi l(R + \lambda_D)^2$ **(Table S1)**. Of note, the existence of interactions between NPs is a major obstacle to determine their actual persistence length because the scattering in the low q region is affected by both the length of the NPs and their interactions. Scattering in the intermediate q region provided the lower limit of the actual persistent (or nanoparticle) length (∼13–20 nm).

The coexistence of rather short and long worm-like NPs was further supported by the ultracentrifugation of the 8 mM SQ-Dox suspension. The supernatant SAXS pattern could be modeled by rod-like particles with length of ∼20 nm, while the pellet pattern showed longer aggregated NPs **(Figure S3)**.

The radial density distribution obtained from molecular dynamics (MD) calculations was in excellent agreement with these findings **(Figure 1f)**. During the simulations **(Figure 1d, e)**, spontaneous formation of cylindrical NPs could be observed from initial unstructured SQ-Dox aggregates on the time scale of hundreds of nanoseconds **(Figure S4)**.

Of note, the formation of cylindrical aggregates is specific to SQ-Dox and contrasts with the shape of other squalene-based NPs.[21–24] We assume that it originates from Dox stacking. Indeed, Dox is known to self-assemble in aqueous solution to form dimers, in parallel or antiparallel orientation, oligomers, or fibers, depending on the concentration, the pH of the solution, and the presence of added salts.[25–30] The absorbance and fluorescence spectra of SQ-Dox in water confirmed the stacking of Dox moieties in NPs for concentration above 5 µM **(Figure S5)**.

In simulated SQ-Dox aggregates, the stacks started forming within hundreds of picoseconds and persisted on the time scales of hundreds of nanoseconds up to the end of the simulations. Four distinct types of stacks were observed, differing in the relative orientation of the Dox rings **(Figure 2)**. We classified the stacks by the relative orientation of the long axes and normal of Dox ring systems (see **Supporting Information** for detailed description). The p–p stacks were the most abundant and tended to form extended fan-like structures, including up to six molecules with long axes slightly inclined to each other. Three subpopulations of p–p pairs, which differed in the inclination angle α and the distance d: $p–p_1$ (d ∼ 0.55 nm, α ∼ 20°): $p–p_2$ (d ∼ 0.45 nm, α ∼ 40°); $p–p_3$ (d ∼ 0.45 nm, α ∼ 60°), coexisted in cylindrical NPs **(Figure S6a)**. The free energy barrier of disrupting the $p–p_1$ stacking interaction in cylindrical micelles was estimated in MD simulations as ∼30 kJ mol^{-1} **(Figure S7)**. This indicated strong interaction with characteristic lifetime of minutes. The a–a and p–a stacks were also observed, while a–p stacks were very rare **(Figure S6b)**. Despite numerous subpopulations of stacked pairs, the orientation of Dox heads relative to the radius of cylinders was rather homogeneous and formed a single dominant population **(Figure S6c)**. However, the relative abundances of the different types of stacks could not be quantified since the molecule stacking was correlated with the nanoparticle density, given in arbitrary units.
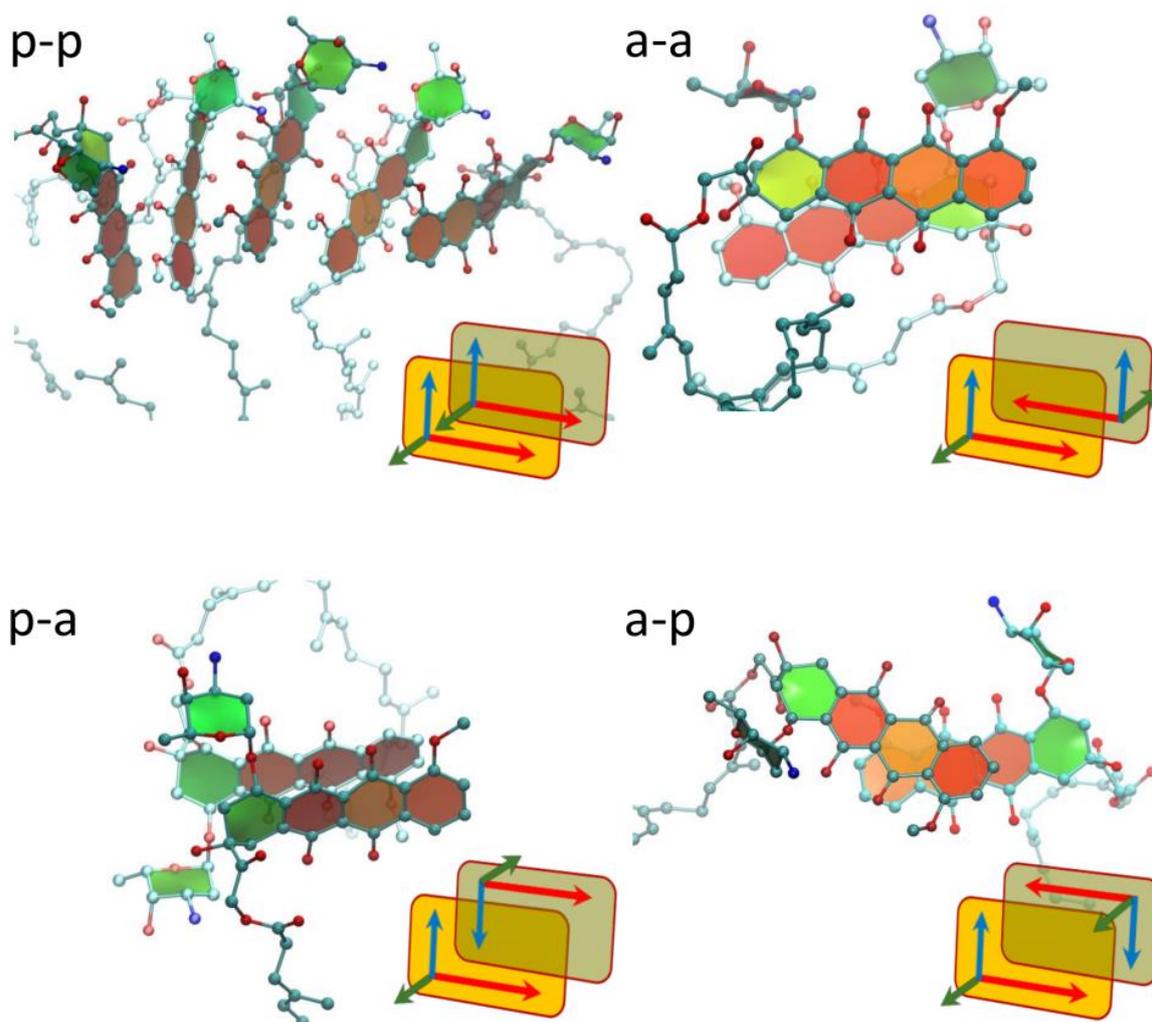
Figure 2. Different types of stacked aggregates observed in MD simulations. Each panel shows a simulation snapshot with stacked SQ-Dox molecules in corresponding configuration and a scheme of the aggregate. On the scheme red, blue and green arrows correspond to long, short and normal axes of the Dox rings (see Supporting Information for details). Schemes are not aligned with the molecules on snapshots and correspond to them up to 3D rotation. On the first panel the fan-like aggregate of five stacked molecules in p-p orientation is shown. Other panels show aggregates of two molecules.

To confirm the preferential assembling of SQ-Dox into cylindrical aggregates, the packing parameter p has been evaluated through Langmuir–Blodgett experiments. A molecular area of 53 Å² was deduced from the SQ-Dox monolayer compression isotherm **(Figure S8a)**, leading to a p value of 0.51, clearly consistent with the formation of cylindrical NPs.[31] The compressibility modulus K for the SQ-Dox monolayer exhibited a maximum value of 92 mN·m^{-1}, higher than the compressibility modulus maxima of squalenic acid and squalene-based cytidine derivatives, comprised in the 43–62 mN·m^{-1} range **(Figure S8b)**.[32] This is likely a consequence of Dox stacking. Interestingly, this

maximum was obtained for a large range of surface pressure, suggesting possible molecular reorganization in the monolayer.

2. Influence of salt on SQ-Dox nanoparticles structure

The influence of adding NaCl to an already prepared SQ-Dox nanoparticle suspension in water was investigated, using a SQ-Dox:NaCl ratio of 1:1 mol:mol. Added salts are expected to screen the intramicellar repulsive interactions between charges, entailing the growth of aggregates.[19] Cryo-TEM pictures revealed that compared to SQ-Dox in pure water, the number and the length of long worm-like NPs increased after NaCl addition and the two previously described populations with diameters ∼5 nm and ∼11.7 nm were detected **(Figure 3a)**.
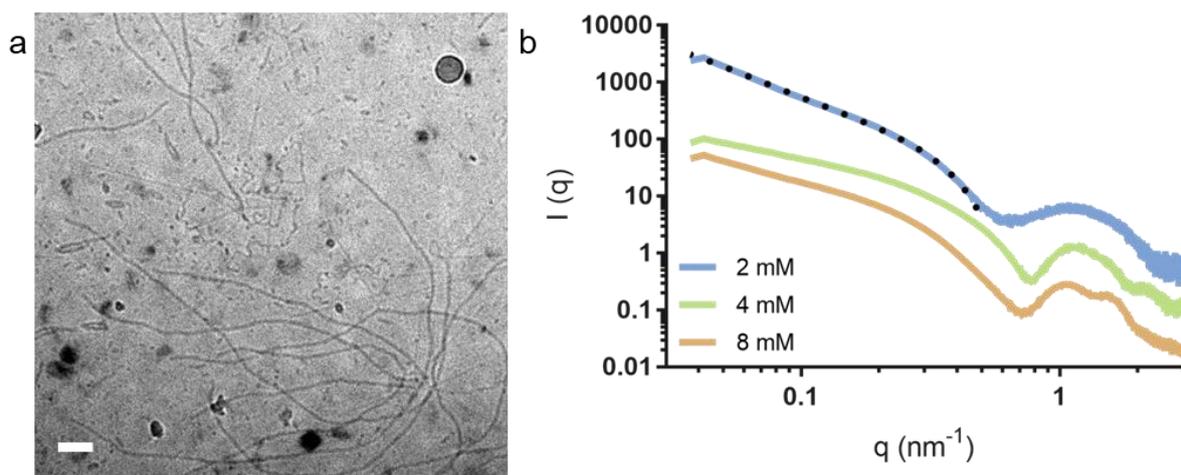
Figure 3. Morphological evolution of SQ-Dox NPs. **a.** Cryo-TEM micrograph of a suspension of NPs prepared at a concentration of 2 mM in H_2O with addition of 2 mM NaCl (scale bar, 100 nm). **b.** Influence of salt addition on NPs SAXS patterns. The SQ-Dox NPs are prepared at concentrations ranging from 2 mM to 8 mM, and NaCl is added using a molar ratio SQ-Dox:NaCl 1:1. The dotted line corresponds to the fit of the 2 mM curve. The curves have been shifted along the y-axis for clarity.

The SAXS pattern of a 2 mM SQ-Dox nanosuspension in the presence of 2 mM NaCl revealed the formation of long worm-like NPs **(Figure 3b)**. The scattered intensity I(q) showed a clear upturn in the low q region (q ≤ 0.25 nm−1) relative to the q^{-1} behavior typical of straight rods observed at intermediate q values. In the 0.05–0.5 nm^{-1} q-range, the curve could be fitted with the two

models of long semiflexible chains without interactions developed by Kholodenko and Pedersen and Schurtenberger.[33,34] They yielded similar Kuhn lengths $2l_p \sim 30$ nm. For NPs prepared at 4 mM and 8 mM, the repulsive interactions between the NPs were screened upon addition of NaCl, as shown by the disappearance of the correlation peak at $q \sim 0.24$ nm^{-1} compared to NPs in water **(Figure 1d)** and by the q^{-1} dependence of the scattered intensity extending at low q values **(Figure 3b)**. The decrease of the Debye lengths λ_D also confirmed this screening process **(Table S1)**. The SAXS pattern of the 4 mM suspension could be fitted with a model of 100 nm-long stiff cylinders. However, according to cryo-TEM pictures, this length could rather describe the persistence length. Taken together, the above results suggested an increase of nanoparticle flexibility with the addition of NaCl.

The screening of repulsive interactions between cylindrical aggregates may favor their side-by-side association, as suggested by the scattering curve in the high q region of the SQ-Dox NPs at a concentration of 8 mM with NaCl at molar ratio 1:1 **(Figure 3b)**. A factor structure, resulting from the close packing of some cylinders, was superimposed on the oscillation at high q, while the low-q part of the curve could be fitted, as above, with 100 nm-long rods, here displaying an ellipsoidal cross-section. The length of the short semi-axis and the ellipticity ratio were 3.8 nm and 2.2, respectively, consistent with the size of the thicker NPs. The peaks at 0.94 nm^{-1} and 1.7 nm^{-1} corresponded to the first and second order of reflection arising from the stacking of cylinders with a mean distance between their axes of $\sim$6.7 nm, consistent with their diameter.

Additional insights into the structure of the SQ-Dox NPs were provided by AFM imaging. It has been observed that the AFM height image of the SQ-Dox samples displayed a mixture of spheres and long cylinders affected in two ways: (i) by the attractive interactions between the positively charged NPs and the silicon surface that tended to flatten the NPs and (ii) by the convolution between the AFM tip and NPs lateral dimensions **(Figure 4a)**. The AFM phase image suggested that thin cylinders formed helical bundles during their aggregation into thick cylinders (see arrow in **Figure 4b**). The MD simulations of interacting worm-like NPs also highlighted the formation of twisted aggregates, which could also form helical bundles on larger scales **(Figure S9)**.
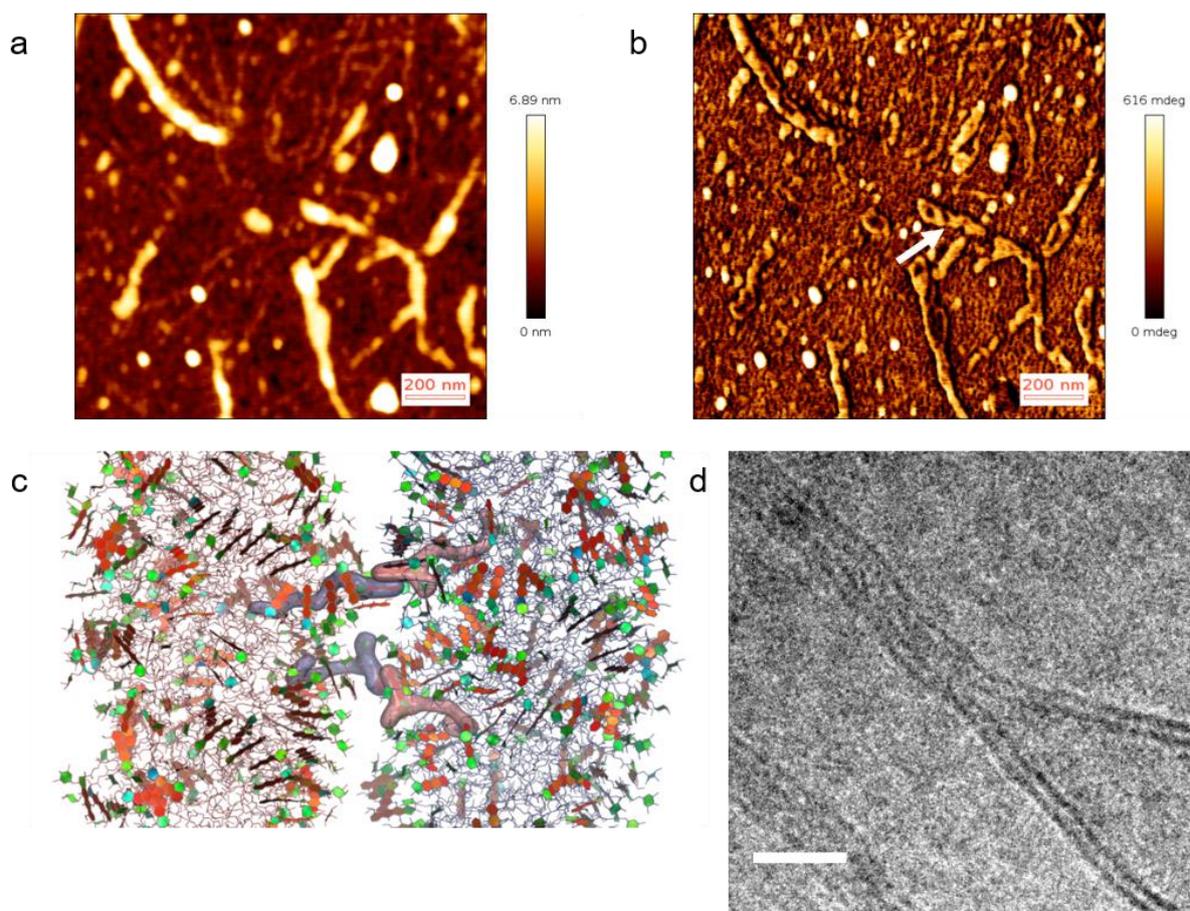
Figure 4. Mechanism of interaction between cylindrical NPs with monovalent anions. **a. b.** AFM pictures obtained in liquid medium of SQ-Dox NPs (2 mM with 2 mM NaCl, scale bar, 200 nm). **a.** Height image. **b.** Phase image. **c.** MD simulations showing intercylinders stacking interactions. Stacking pairs from different cylinders are highlighted by semitransparent surfaces. The colors are the same as in **Figure 1**. **D.** Cryo-TEM pictures show the stacking of SQ-Dox NPs (2 mM with 2 mM NaCl) to form multilayer structures (scale bar, 20 nm).

MD simulations also revealed the existence of intercylinder stacking interactions involving a–a and a–p stacking pairs. Although the formation of such "bridges" was rare (only two pairs were formed during the simulation time of 300 ns), they were able to keep the cylinders together once formed. This allowed us to hypothesize a "zipper-like" mechanism of interaction between the cylinders **(Figure 4c)**. Once several intercylinder stacks formed, they would keep the cylinders at close distance for a sufficiently long time to facilitate the formation of even more stacks. The formation of "zipped" cylinders was also clearly observed by cryo-TEM **(Figure 4d)**.

3. Influence of the nature of the salt on the structure of the SQ-Dox nanoparticles

In order to investigate the impact of the nature of the salt on the supramolecular assembly of SQ-Dox, Na_2SO_4 was added to a 2 mM water suspension of NPs, with addition of 0.01 to 1 mM Na_2SO_4 (SQ-Dox:Na_2SO_4 ratios 20:1 to 2:1 mol:mol, respectively). Using 0.01 mM Na_2SO_4, long core–shell cylinders were observed as the main population **(Figure 5a)**, while with higher Na_2SO_4 concentrations, the divalent anions allowed the formation of wider (d ~14.3 nm, **Figures 5b** and **S10a**), shorter, and more rigid cylindrical NPs compared to monovalent anions (*i.e.*, NaCl). The SAXS curve at low q could be modeled by cylinders with a log normal distribution of radii around 7 nm, in agreement with the diameters measured in cryo-TEM experiment **(Figure 5a)**. Both Cryo-TEM images and SAXS pattern suggested the formation of nanotubes consisting of an aqueous core surrounded by a SQ-Dox bilayer. Some images also suggested the existence of nanoassemblies comprising a SQ-Dox cylindrical core surrounded by a bilayer shell **(Figure S10b)**.

The possible formation of stable bilayers with an average thickness of ~4 nm was supported by MD simulation (**Figures 5c, d** and **S11a, b**). Experimentally, the rod-to-bilayer transition was expected to arise from both the screening of charges and the ability of divalent anions to form long-lived bridges between charged Dox moieties. The distributions of the distances between N atoms of the sugar moieties in stacked Dox pairs were computed for Cl^- and SO_4^{2-} ions, demonstrating that these distances were significantly shorter in the presence of SO_4^{2-} ions **(Figure S11c)**. The decrease in electrostatic repulsion and salt bridges between nearest-neighbor amine groups led to a denser packing of SQ-Dox molecules, along with an increase in the packing parameter and a lower curvature of the NPs. The bilayers thus formed were flexible enough to bend into cylinders.
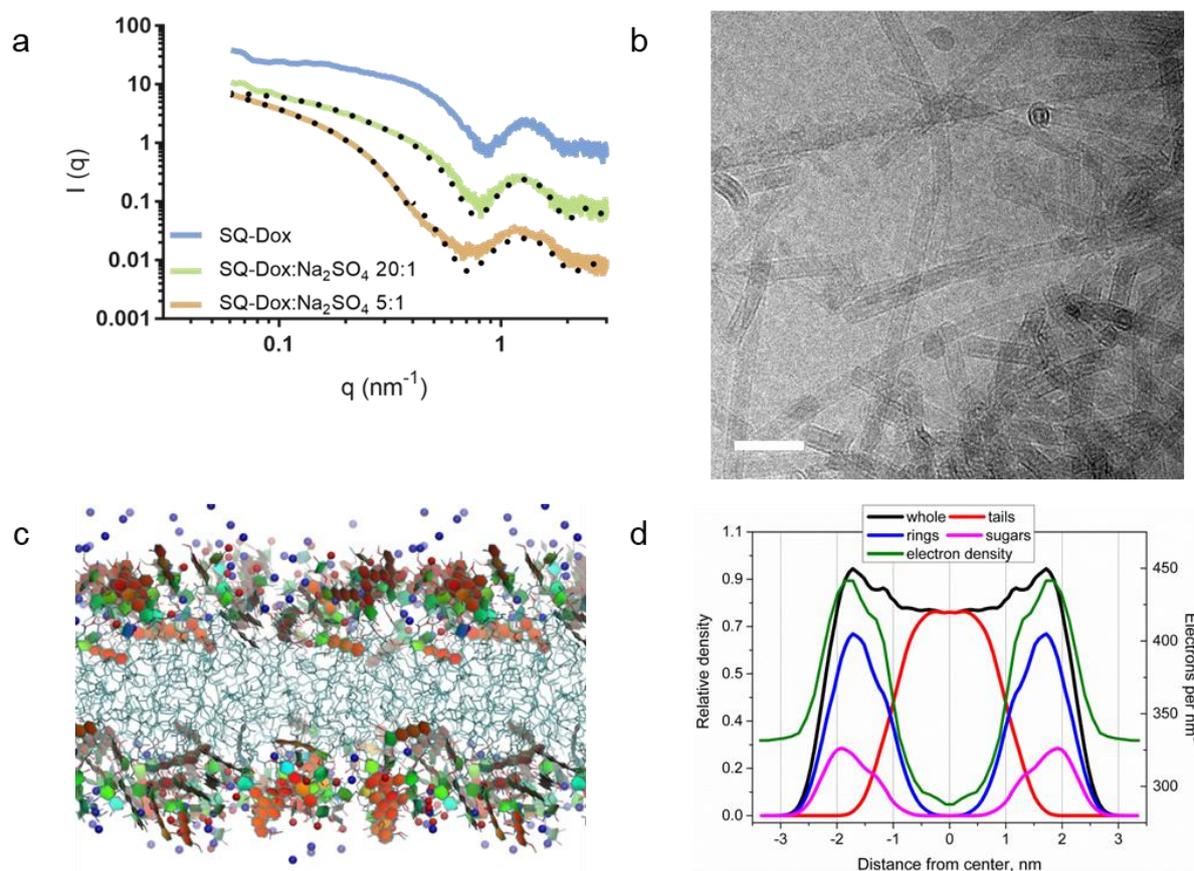
Figure 5. Morphology of SQ-Dox NPs in the presence of divalent anions. **a.** SAXS patterns of SQ-Dox NPs in the presence of Na_2SO_4. The SQ-Dox NPs are prepared at 2 mM, and Na_2SO_4 is added at 0.01 mM (molar ratio 20:1) or 0.04 mM (molar ratio 5:1). The dotted lines correspond to the fits of the experimental curves. The curves have been shifted along the y-axis for clarity. **b.** Cryo-TEM micrograph of a suspension of SQ-Dox NPs at a concentration of 2 mM with addition of 0.04 mM Na_2SO_4 (Scale bar, 50 nm). **c.** Snapshot of equilibrated SQ-Dox bilayer. Squalene tails are shown as sticks. Aromatic rings are filled with red and orange while non-aromatic rings with green and cyan. Positively charged NH_3^+ groups are shown as red spheres. Na^+ ions are blue. Water is not shown for clarity. **d.** Density profiles for equilibrated SQ-Dox bilayer including electron density profile.

Interestingly, some cryo-TEM images suggested the wrapping of a bilayer around a SQ-Dox cylinder (**Figure S10b**). The formation mechanism could rely on the adsorption of SQ-Dox monomers at the surface of cylindrical NPs through the formation of SO_4^{2-} bridges. The bilayer could then be generated by the addition of another layer of monomers to avoid unfavorable interaction of SQ chains with water. Tubes of 16–17 nm diameter, consisting in a SQ-Dox bilayer separated from the cylindrical core by a thin layer of water, were constructed in MD simulations (**Figure S10c, d**). The density map of Dox headgroups in the cross-section, symmetrized radially around the axis of the tube, exhibited three distinct rings corresponding to the layers of Dox moieties located at distances of ~2.2

nm, ~4.1 nm, and ~7.5 nm from the center. Those values are in good agreement with cryo-TEM findings (**Figure S10b, e**).

4. Discussion

So far, two main delivery strategies have been employed to reduce the toxicity and improve the efficacy of Dox: (i) the encapsulation of Dox into nanocarriers, usually liposomes or polymeric carriers and (ii) the design of prodrugs activated by an enzyme overexpressed in the tumor microenvironment or by an acidic pH.[35] SQ-Dox is a simple lipid-like molecule which combines the properties of a prodrug and the ability to self-assemble as elongated NPs in water to ensure enhanced pharmacological activity, making it appealing for clinical perspective. The structure of the NPs results from the interplay between hydrophobic interactions of squalene chains and stacking and electrostatic interactions of Dox head groups. Absorbance and fluorescence experiments revealed the stacking of Dox heads, whose MD simulations gave a more quantitative description. Stacking interactions of Dox heads not only lead to the formation of cylindrical NPs instead of spherical, but such interactions also result in an impressive heterogeneity of NPs surfaces, which contain four distinct topologies of stacks subdivided further into a number of subpopulations. The minor population of antiparallel stacks is especially important because of its ability to "zip" cylindrical NPs together, leading to the formation of bundles and other complex aggregates, especially in the presence of salts. The charge of the Dox headgroups adds, indeed, another dimension for adjusting and controlling the NPs structure. Addition of monovalent salts resulted in the elongation of cylindrical NPs, which could be beneficial for prolonging the blood circulation time and avoiding the capture by the macrophages of the reticuloendothelial system. But divalent anions provided another mechanism of assembly by means of salt bridges, triggering a dramatic transition from individual cylindrical NPs to bilayer tubes in solutions in the late stages of their evolution. Suggested sequence of events during the evolution of SQ-Dox NPs in different salt solutions is shown in **Figure 6**.
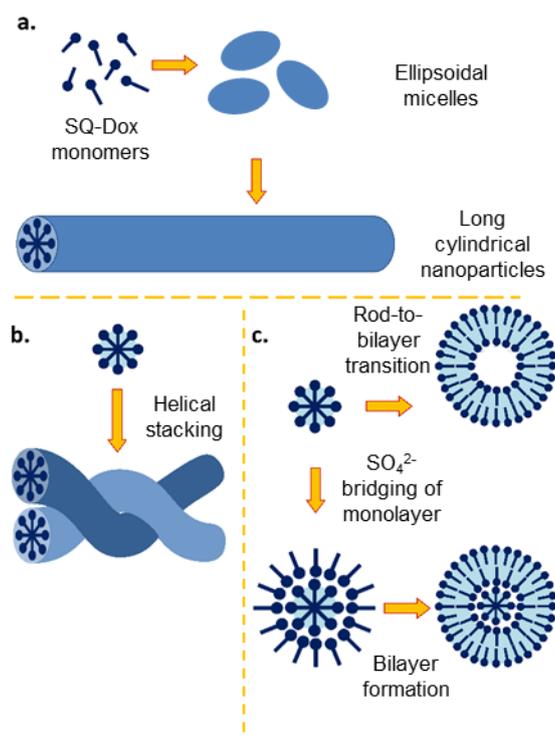
Figure 6. Schematic representation of the mechanisms of SQ-Dox assembly into elongated NPs. **a.** Early stages of assembly – spontaneous formation of short cylindrical micelles and their elongation. **b.** Late stages of assembly with monovalent anions. **c.** Late stages of assembly with divalent anions. Dox headgroups are shown as filled circles and squalene tails as rods. In **b.** and **c.** the hydrophobic areas are cyan, while white areas are assumed to be filled with water.

It has been reported in the literature that self-assembled nucleolipids may exhibit a variety of morphologies, including worm-like micelles, that depend on both the nucleosidic headgroups and the lipid chains.[36–38] The phase behavior of SQ-Dox demonstrates that polar heads other than those derived from a nucleobase can guide the self-assembly of lipid-based bioconjugates into complex structures such as rod-like NPs. Moreover, previous experiments on squalene-based nucleolipids have shown that squalene chains could fit into various structures such as inverse hexagonal phases or bilayers forming liposomes, lamellar phases, inverse bicontinuous cubic phases, or sponge phases.[32] Coupling squalene with other polar drug molecules capable of π–π interactions (*e.g.,* camptothecin and derivatives, ciprofloxacin, *etc*.)[39,40] could therefore be envisioned to broaden the approach and to design nonspherical drug-delivery systems. In addition, the excellent agreement between experimental results and MD simulations suggests that computational techniques could be used to screen bioconjugates prone to self-assemble as elongated NPs.

Altogether, these results raise another concern about the preservation of the nanodrugs properties after administration in patient body. For example, the shape of NPs influences their circulation in the bloodstream, while their size drives the filtration processes. Adjusting shape and surface charge may also help to avoid capture by the macrophages and the reticuloendothelial system.[41] We demonstrated here that those parameters may be radically modified by addition of species as simple as basic ions, naturally present in the blood. The investigation of this feature seems particularly relevant for the development of NPs specifically engineered to reach particular targets.

IV. Conclusion

We demonstrated here that the shape, size, and surface properties of SQ-Dox NPs could easily be modulated in broad ranges by varying the bioconjugate concentration, the ionic strength, and the nature of the anion. But the present study also suggests that the NPs in the test tube and in the body may not be the same since their structure may dramatically vary according to the local *in vivo* environment, and this may have some clinical implications. Nevertheless, SQ-Dox may serve as a model for creating lipid-like self-assembling molecules with stacking and cross-linking behavior tuned for particular medical applications.

V. References

(1)   Lefrak, E. A.; Piťha, J.; Rosenheim, S.; Gottlieb, J. A. A Clinicopathologic Analysis of Adriamycin Cardiotoxicity. *Cancer* **1973**, *32* (2), 302–314.

(2)   Maksimenko, A.; Dosio, F.; Mougin, J.; Ferrero, A.; Wack, S.; Reddy, L. H.; Weyn, A.-A.; Lepeltier, E.; Bourgaux, C.; Stella, B.; Cattel, L.; Couvreur, P. A Unique Squalenoylated and Nonpegylated Doxorubicin Nanomedicine with Systemic Long-Circulating Properties and Anticancer Activity. *Proceedings of the National Academy of Sciences* **2014**, *111* (2), E217–E226.

(3)   Geng, Y.; Dalhaimer, P.; Cai, S.; Tsai, R.; Tewari, M.; Minko, T.; Discher, D. E. Shape Effects of Filaments versus Spherical Particles in Flow and Drug Delivery. *Nature Nanotechnology* **2007**, *2* (4), 249–255.

(4)   Christian, D. A.; Cai, S.; Garbuzenko, O. B.; Harada, T.; Zajac, A. L.; Minko, T.; Discher, D. E. Flexible Filaments for *in Vivo* Imaging and Delivery: Persistent Circulation of Filomicelles Opens the Dosage Window for Sustained Tumor Shrinkage. *Molecular Pharmaceutics* **2009**, *6* (5), 1343–1352.

(5)   Li, Y.; Lian, Y.; Zhang, L. T.; Aldousari, S. M.; Hedia, H. S.; Asiri, S. A.; Liu, W. K. Cell and Nanoparticle Transport in Tumour Microvasculature: The Role of Size, Shape and Surface Functionality of Nanoparticles. *Interface Focus* **2016**, *6* (1), 20150086.

(6)   Champion, J. A.; Mitragotri, S. Shape Induced Inhibition of Phagocytosis of Polymer Particles. *Pharmaceutical Research* **2009**, *26* (1), 244–249.

(7)   Sun, J.; Zhang, L.; Wang, J.; Feng, Q.; Liu, D.; Yin, Q.; Xu, D.; Wei, Y.; Ding, B.; Shi, X.; Jiang, X. Tunable Rigidity of (Polymeric Core)-(Lipid Shell) Nanoparticles for Regulated Cellular Uptake. *Advanced Materials* **2015**, *27* (8), 1402–1407.

(8)   Jelonek, K.; Li, S.; Wu, X.; Kasperczyk, J.; Marcinkowski, A. Self-Assembled Filomicelles Prepared from Polylactide/Poly(Ethylene Glycol) Block Copolymers for Anticancer Drug Delivery. *International Journal of Pharmaceutics* **2015**, *485* (1–2), 357–364.

(9)   Wan, X.; Min, Y.; Bludau, H.; Keith, A.; Sheiko, S. S.; Jordan, R.; Wang, A. Z.; Sokolsky-Papkov, M.; Kabanov, A. V. Drug Combination Synergy in Worm-like Polymeric Micelles Improves Treatment Outcome for Small Cell and Non-Small Cell Lung Cancer. *ACS Nano* **2018**, *12* (3), 2426–2439.

(10)   Nair, P. R.; Karthick, S.; Spinler, K. R.; Vakili, M. R.; Lavasanifar, A.; Discher, D. E. Filomicelles from Aromatic Diblock Copolymers Increase Paclitaxel-Induced Tumor Cell Death and Aneuploidy Compared with Aliphatic Copolymers. *Nanomedicine* **2016**, *11* (12), 1551–1569.

(11)   Round, A.; Felisaz, F.; Fodinger, L.; Gobbo, A.; Huet, J.; Villard, C.; Blanchet, C. E.; Pernot, P.; McSweeney, S.; Roessle, M.; Svergun, D. I.; Cipriani, F. BioSAXS Sample Changer: A Robotic Sample Changer for Rapid and Reliable High-Throughput X-Ray Solution Scattering Experiments. *Acta Crystallographica Section D Biological Crystallography* **2015**, *71* (1), 67–75.

(12)   Pernot, P.; Round, A.; Barrett, R.; De Maria Antolinos, A.; Gobbo, A.; Gordon, E.; Huet, J.; Kieffer, J.; Lentini, M.; Mattenet, M.; Morawe, C.; Mueller-Dieckmann, C.; Ohlsson, S.; Schmid, W.; Surr, J.; Theveneau, P.; Zerrad, L.; McSweeney, S. Upgraded ESRF BM29 Beamline for SAXS on Macromolecules in Solution. *Journal of Synchrotron Radiation* **2013**, *20* (4), 660–664.

(13)   Brennich, M. E.; Kieffer, J.; Bonamis, G.; De Maria Antolinos, A.; Hutin, S.; Pernot, P.; Round, A. Online Data Analysis at the ESRF BioSAXS Beamline, BM29. *Journal of Applied Crystallography* **2016**, *49* (1), 203–212.

(14)   Breßler, I.; Kohlbrecher, J.; Thünemann, A. F. *SASfit*: A Tool for Small-Angle Scattering Data Analysis Using a Library of Analytical Expressions. *Journal of Applied Crystallography* **2015**, *48* (5), 1587–1598.

(15)   Yesylevskyy, S. O.; Ramseyer, C.; Savenko, M.; Mura, S.; Couvreur, P. Low-Density Lipoproteins and Human Serum Albumin as Carriers of Squalenoylated Drugs: Insights from Molecular Simulations. *Molecular Pharmaceutics* **2018**, *15* (2), 585–591.

(16)   Sousa da Silva, A. W.; Vranken, W. F. ACPYPE - AnteChamber PYthon Parser InterfacE. *BMC Research Notes* **2012**, *5* (1), 367.

(17)   Frisch, M. J.; Trucks, G. W.; Schlegel, H. B.; Scuseria, G. E.; Robb, M. A.; Cheeseman, J. R.; Scalmani, G.; Barone, V.; Mennucci, B.; Petersson, G. A.; Nakatsuji, H.; Caricato, M.; Li, X.; Hratchian, H. P.; Izmaylov, A. F.; Bloino, J.; Zheng, G.; Sonnenberg, J. L.; Hada, M.; Ehara, M.; *et al. GAUSSIAN09*; Gaussian, Inc.: Wallingford, CT, 2009.

(18)   Espinat, D. Principes Théoriques de La Diffusion Cohérente Statique. *Application des Techniques de Diffusion de la Lumière, des Rayons X et des Neutrons à l'Etude des Systèmes Colloïdaux*; Technip: Paris, 1992; pp 3–13.

(19)   Dreiss, C. A. Worm-like Micelles: Where Do We Stand? Recent Developments, Linear Rheology and Scattering Techniques. *Soft Matter* **2007**, *3* (8), 956–970.

(20)   Lequeux, F. Structure and Rheology of Worm-like Micelles. *Current Opinion in Colloid & Interface Science* **1996**, *1* (3), 341–344.

(21)   Kotelevets, L.; Chastre, E.; Caron, J.; Mougin, J.; Bastian, G.; Pineau, A.; Walker, F.; Lehy, T.; Desmaële, D.; Couvreur, P. A Squalene-Based Nanomedicine for Oral Treatment of Colon Cancer. *Cancer Research* **2017**, *77* (11), 2964–2975.

(22)   Gaudin, A.; Yemisci, M.; Eroglu, H.; Lepetre-Mouelhi, S.; Turkoglu, O. F.; Dönmez-Demir, B.; Caban, S.; Sargon, M. F.; Garcia-Argote, S.; Pieters, G.; Loreau, O.; Rousseau, B.; Tagit, O.; Hildebrandt, N.; Le Dantec, Y.; Mougin, J.; Valetti, S.; Chacun, H.; Nicolas, V.; Desmaële, D.; *et al.* Squalenoyl Adenosine Nanoparticles Provide Neuroprotection after Stroke and Spinal Cord Injury. *Nature Nanotechnology* **2014**, *9* (12), 1054–1062.

(23)   Ralay-Ranaivo, B.; Desmaële, D.; Bianchini, E. P.; Lepeltier, E.; Bourgaux, C.; Borgel, D.; Pouget, T.; Tranchant, J. F.; Couvreur, P.; Gref, R. Novel Self Assembling Nanoparticles for the Oral Administration of Fondaparinux: Synthesis, Characterization and *in Vivo* Evaluation. *Journal of Controlled Release* **2014**, *194*, 323–331.

(24)   Hillaireau, H.; Dereuddre-Bosquet, N.; Skanji, R.; Bekkara-Aounallah, F.; Caron, J.; Lepêtre, S.; Argote, S.; Bauduin, L.; Yousfi, R.; Rogez-Kreuz, C.; Desmaële, D.; Rousseau, B.; Gref, R.; Andrieux, K.; Clayette, P.; Couvreur, P. Anti-HIV Efficacy and Biodistribution of

Nucleoside Reverse Transcriptase Inhibitors Delivered as Squalenoylated Prodrug Nanoassemblies. *Biomaterials* **2013**, *34* (20), 4831–4838.

(25)   Menozzi, M.; Valentini, L.; Vannini, E.; Arcamone, F. Self-Association of Doxorubicin and Related Compounds in Aqueous Solution. *Journal of Pharmaceutical Sciences* **1984**, *73* (6), 766–770.

(26)   Agrawal, P.; Barthwal, S. K.; Barthwal, R. Studies on Self-Aggregation of Anthracycline Drugs by Restrained Molecular Dynamics Approach Using Nuclear Magnetic Resonance Spectroscopy Supported by Absorption, Fluorescence, Diffusion Ordered Spectroscopy and Mass Spectrometry. *European Journal of Medicinal Chemistry* **2009**, *44* (4), 1437–1451.

(27)   Fülöp, Z.; Gref, R.; Loftsson, T. A Permeation Method for Detection of Self-Aggregation of Doxorubicin in Aqueous Environment. *International Journal of Pharmaceutics* **2013**, *454* (1), 559–561.

(28)   Li, X.; Hirsh, D. J.; Cabral-Lilly, D.; Zirkel, A.; Gruner, S. M.; Janoff, A. S.; Perkins, W. R. Doxorubicin Physical State in Solution and inside Liposomes Loaded *via* a PH Gradient. *Biochimica et Biophysica Acta (BBA) - Biomembranes* **1998**, *1415* (1), 23–40.

(29)   Zhu, L.; Yang, S.; Qu, X.; Zhu, F.; Liang, Y.; Liang, F.; Wang, Q.; Li, J.; Li, Z.; Yang, Z. Fibril-Shaped Aggregates of Doxorubicin with Poly- L -Lysine and Its Derivative. *Polymer Chemistry* **2014**, *5* (19), 5700–5706. https://doi.org/10.1039/C4PY00686K.

(30)   Eksborg, S. Extraction of Daunorubicin and Doxorubicin and Their Hydroxyl Metabolites: Self-Association in Aqueous Solution. *Journal of Pharmaceutical Sciences* **1978**, *67* (6), 782–785.

(31)   Israelachvili, J.; Ladyzhinski, I. The Physico-Chemical Basis of Self-Assembling Structures. In *Forces, Growth and Form in Soft Condensed Matter: At the Interface between Physics and Biology*; Skjeltorp, A. T., Belushkin, A. V., Eds.; Kluwer Academic Publishers: Dordrecht, 2005; Vol. 160, pp 1–28.

(32)   Lepeltier, E.; Bourgaux, C.; Rosilio, V.; Poupaert, J. H.; Meneau, F.; Zouhiri, F.; Lepêtre-Mouelhi, S.; Desmaële, D.; Couvreur, P. Self-Assembly of Squalene-Based Nucleolipids:

Relating the Chemical Structure of the Bioconjugates to the Architecture of the Nanoparticles. *Langmuir* **2013**, *29* (48), 14795–14803.

(33)   Kholodenko, A. L. Analytical Calculation of the Scattering Function for Polymers of Arbitrary Flexibility Using the Dirac Propagator. *Macromolecules* **1993**, *26* (16), 4179–4183.

(34)   Pedersen, J. S.; Schurtenberger, P. Scattering Functions of Semiflexible Polymers with and without Excluded Volume Effects. *Macromolecules* **1996**, *29* (23), 7602–7612.

(35)   Borišev, I.; Mrđanovic, J.; Petrovic, D.; Seke, M.; Jović, D.; Srđenović, B.; Latinovic, N.; Djordjevic, A. Nanoformulations of Doxorubicin: How Far Have We Come and Where Do We Go from Here? *Nanotechnology* **2018**, *29* (33), 332002.

(36)   Bombelli, F. B.; Berti, D.; Almgren, M.; Karlsson, G.; Baglioni, P. Light Scattering and Cryo-Transmission Electron Microscopy Investigation of the Self-Assembling Behavior of Di-C $_{12}$ P-Nucleosides in Solution. *The Journal of Physical Chemistry B* **2006**, *110* (35), 17627–17637.

(37)   Gissot, A.; Camplo, M.; Grinstaff, M. W.; Barthélémy, P. Nucleoside, Nucleotide and Oligonucleotide Based Amphiphiles: A Successful Marriage of Nucleic Acids with Lipids. *Organic & Biomolecular Chemistry* **2008**, *6* (8), 1324.

(38)   Berti, D.; Montis, C.; Baglioni, P. Self-Assembly of Designer Biosurfactants. *Soft Matter* **2011**, *7* (16), 7150–7158.

(39)   Lei, J.; Chen, Y.; Feng, X.; Jin, J.; Gu, J. Electrostatic Potentials of Camptothecin and Its Analogues. *Theoretical Chemistry Accounts* **2014**, *133* (10).

(40)   Zhang, G.; Zhang, L.; Yang, D.; Zhang, N.; He, L.; Du, G.; Lu, Y. Salt Screening and Characterization of Ciprofloxacin. *Acta Crystallographica Section B Structural Science, Crystal Engineering and Materials* **2016**, *72* (1), 20–28.

(41)   Zhao, Z.; Ukidve, A.; Krishnan, V.; Mitragotri, S. Effect of Physicochemical and Surface Properties on *in Vivo* Fate of Drug Nanocarriers. *Advanced Drug Delivery Reviews* **2019**, *143*, 3-21.

VI. Supporting information

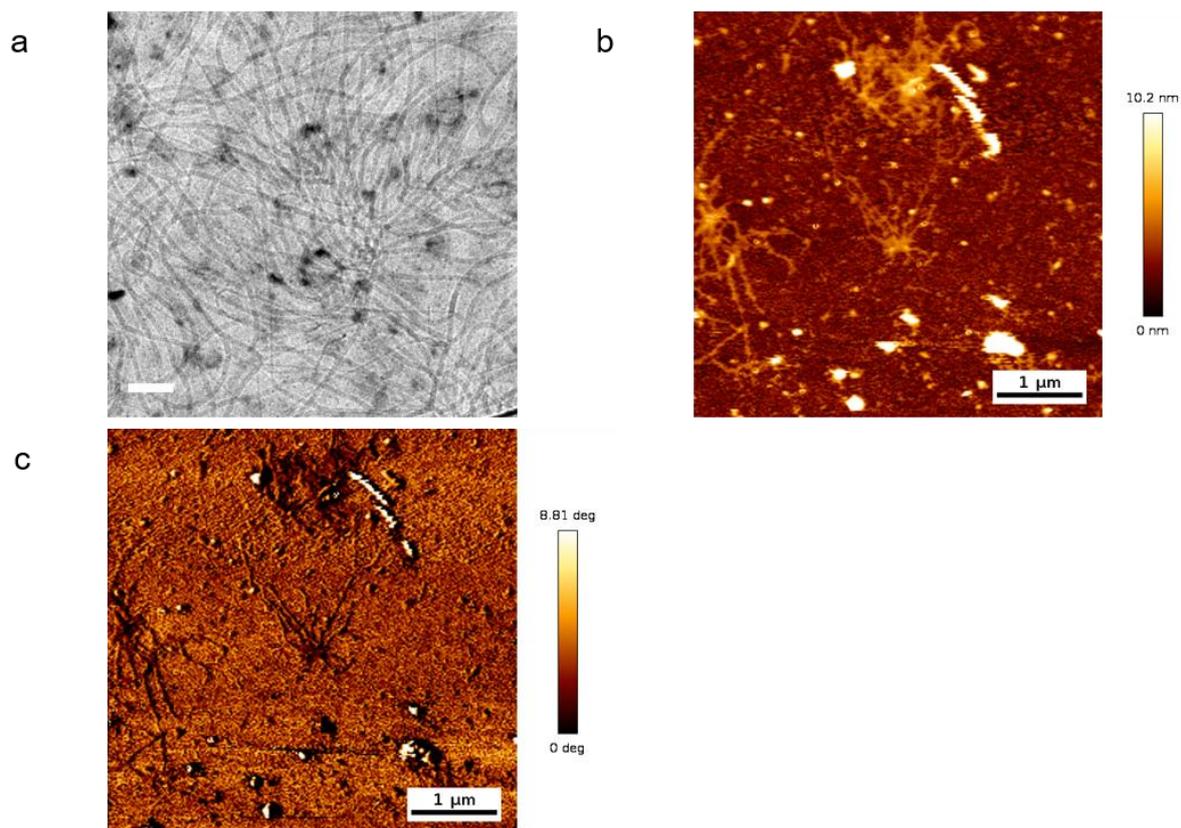### 1. Supplementary figures

Figure S1. a. Additional cryo-TEM micrograph of NPs prepared at 4 mM in H$_2$O (Scale bar, 100 nm). **b. c.** AFM pictures obtained in liquid medium of SQ-Dox NPs prepared at 4 mM in water and diluted to 20 µM (Scale bar, 200 nm). **b.** Height image. **c.** Phase image.
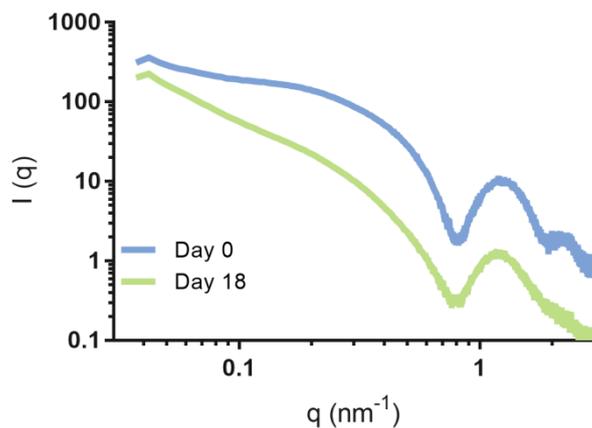
Figure S2. Ageing effect on SAXS patterns of SQ-Dox NPs prepared at 4 mM. SQ-Dox long wormlike NPs are detected after several days: in the low q-range (q ≤ 0.6 nm^{-1}), I(q) could be fitted with the Kholodenko model. Curves are shifted along the y-axis for clarity.
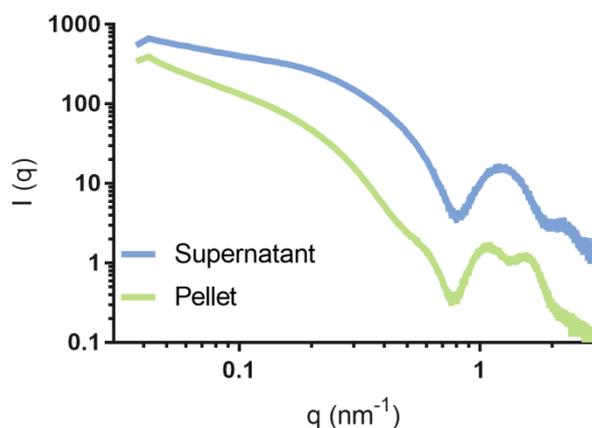

Figure S3. SAXS pattern of SQ-Dox NPs prepared at 8 mM, after ultracentrifugation. The supernatant curve corresponds to short cylindrical NPs (length ~ 20 nm) while the pellet curve indicates the presence of longer aggregated NPs. At q < 0.4 nm^{-1} curve fitting suggests that bundles of about three cylinders, with length ≥ 100 nm, are mostly formed while at q > 0.4 nm^{-1}, the SAXS curve is consistent with the stacking of core-shell cylinders. Curves are shifted along the y-axis for clarity.
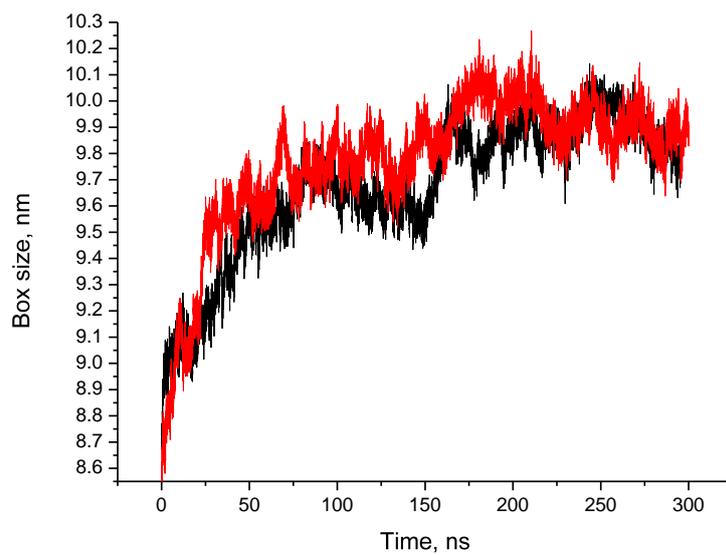
Figure S4. Evolution of the box size in the course of equilibration of SQ-Dox cylindrical NPs. The equilibrium is reached after ~ 200 ns. Results of two independent simulations are shown.
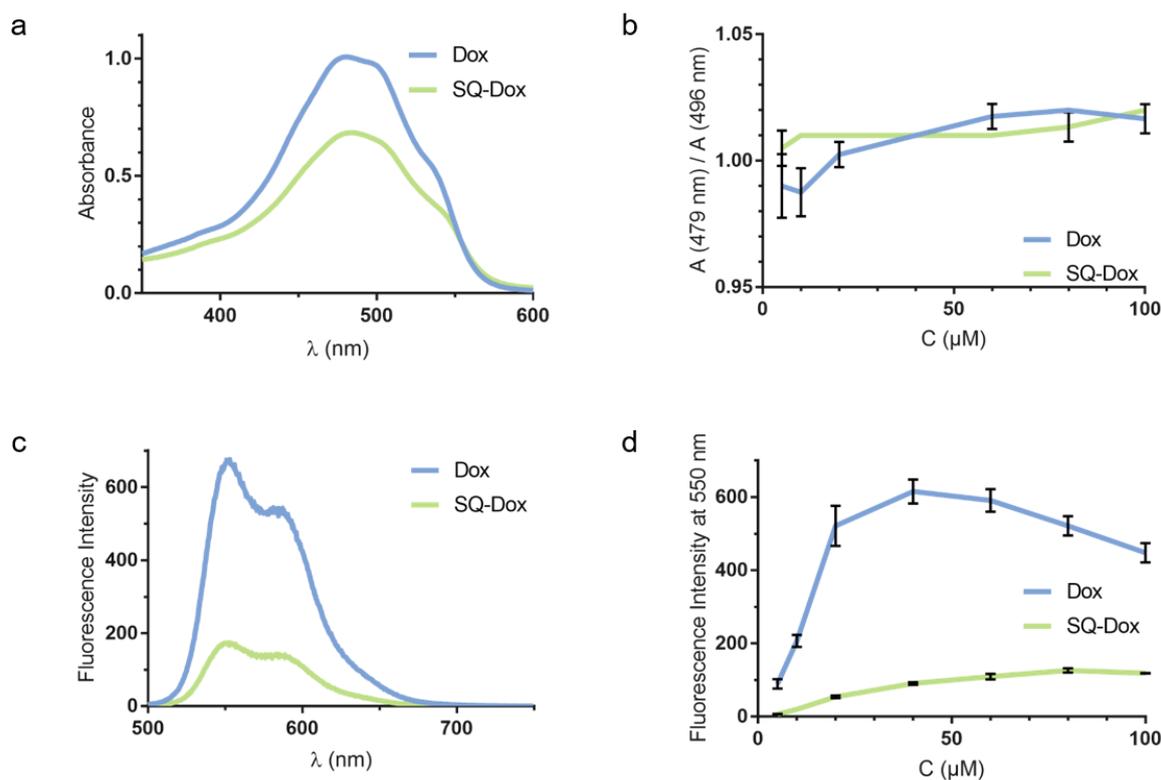
Figure S5. Dox and SQ-Dox spectroscopic properties and stacking characterization. **a.** Absorbance plots of SQ-Dox NPs and free Dox diluted in water at 104 μM. The Dox absorption spectrum displays three bands characteristic of the anthracycline rings in the visible region (479, 496 and 529 nm). Stacking is known to lead to a significant hypochromism in the spectral region below 540 nm and a weak hyperchromism above 540 nm.[1] This highlights the stronger stacking in SQ-Dox NPs than in free Dox solutions. **b.** Absorbance ratio of the 479 and 496 nm bands. The stacking occurs when the absorbance at 496 nm overcomes the absorbance at 479 nm, *i.e.*, A (479 nm) / A (496 nm) > 1. **c.** Fluorescence spectra of SQ-Dox NPs and Dox diluted in water at 52 μM after excitation at 480 nm. The fluorescence of Dox arises from the monomers and is quenched when Dox forms dimers (above ~ 20 μM for free Dox). **d.** Fluorescence intensity at 550 nm after excitation at 480 nm. The enhanced stacking of the anthracycline rings in SQ-Dox NPs is demonstrated by the much lower fluorescence intensity of SQ-Dox compared to free Dox at the same molar concentration. (Data presented as mean ± S. D.)
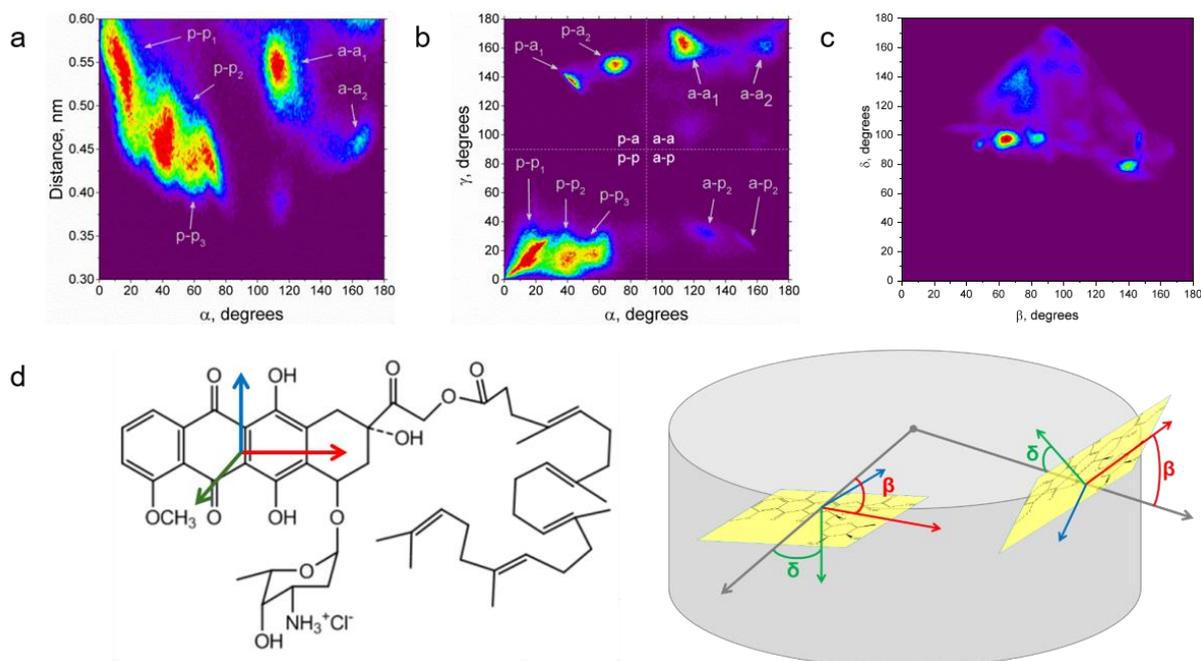
Figure S6. Properties of stacked pairs of rings and their abundances in cylindrical NPs. Color shows probability of finding particular combination of parameters for each type of stacking pairs (purple correspond to zero, red is the maximum). Labels with arrows indicate subpopulations discussed in the text. The codes of aggregates correspond to **Figure 2**. (a) The distance-angle maps where d is the distance between the centers of masses of the rings in a stacked pair and α is the angle between long axes of the rings. (b) The angle-angle maps where α and γ are the angles between long axes and normals to the rings with the axis of cylinder. Dashed lines separate the quadrants corresponding to different types of stacked aggregates, which are shown near the crossing of these lines. (c) The orientation maps of Dox rings where β is the angle between the long axis of the ring and the radius of cylinder at the point of its center of masses. δ is the same for the normal to the ring. (d) Scheme of Dox axes and angles with radius of cylinders. Long axis is red, short axis is blue, normal axis (perpendicular to the figure) is green.
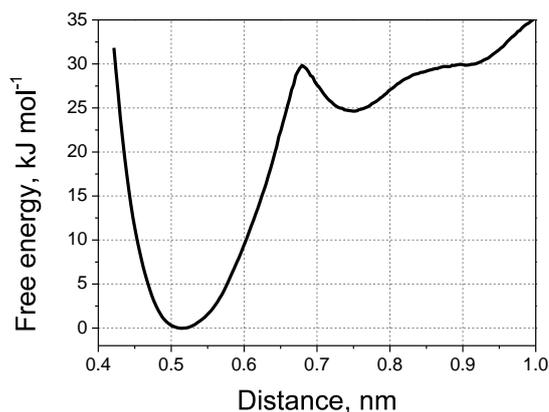
Figure S7. The potential of mean force of disrupting lone p-p$_1$ stacking pair in cylindrical NPs. The minimum corresponds to the most favorable distance between Dox stacking pairs of type p-p$_1$. The optimal stacking distance is ~ 0.51 nm and the free energy rises rapidly with the increase in the distance. There is a metastable state at the distance of ~ 0.74 nm corresponding to two adjacent Dox moieties interacting by means of unspecific interactions. Further increase in the distance starts to drive two molecules away from the same coordination shell.
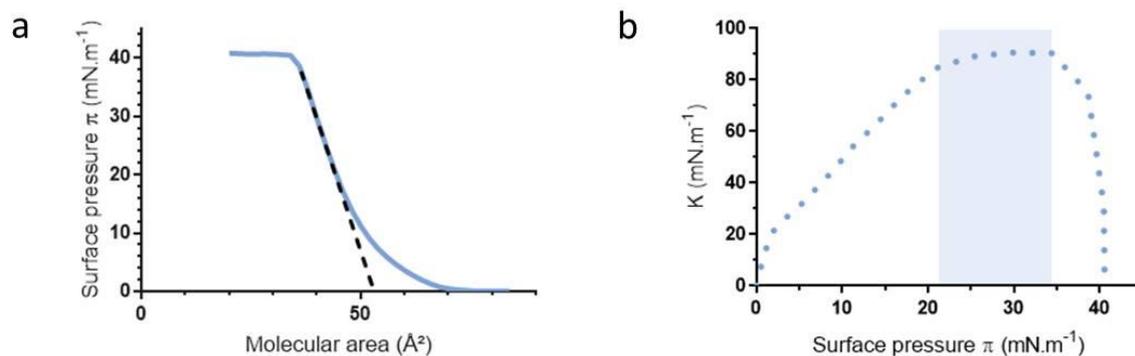

Figure S8. SQ-Dox monolayer properties. (a) Surface pressure-molecular area compression isotherm. The mean molecular area is deduced from the intersection of the tangent to the curve (dashed line) with the X axis. (b) Compressibility modulus K = C$_s^{-1}$ as a function of surface pressure. The blue domain highlights the wide pressure range corresponding to the maximum monolayer compressibility modulus, which suggests possible molecular reorganization within the monolayer.
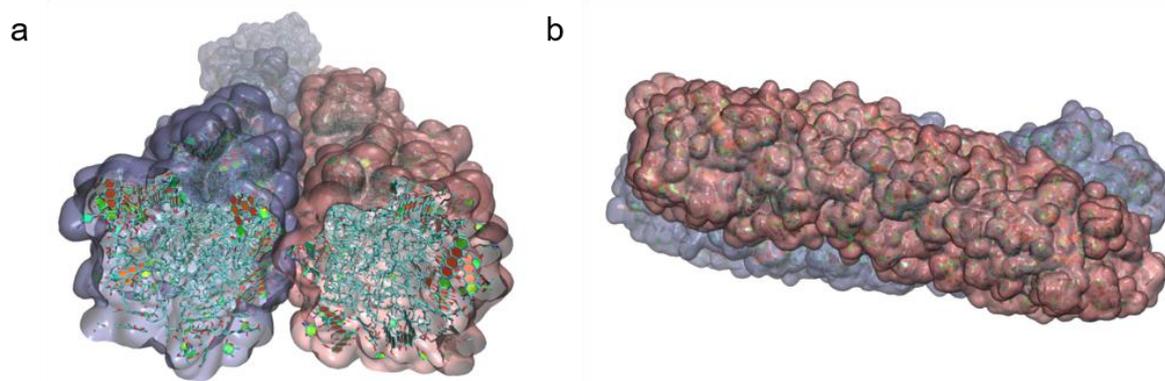
Figure S9. Interacting cylindrical NPs with helical twisting. (a) Front view. (b) Side view
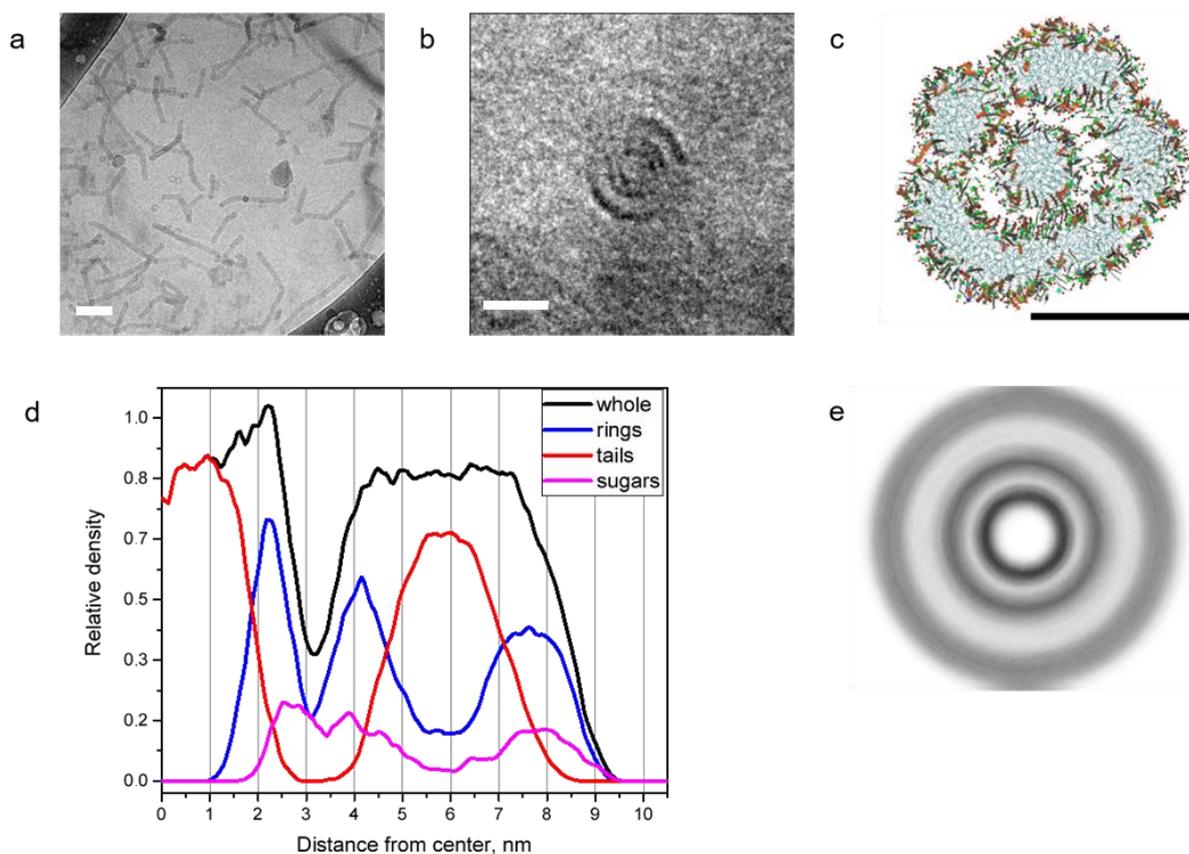

Figure S10. Structure of SQ-Dox nanotubes in the presence of divalent anions. (a) Additional cryo-TEM micrograph of SQ-Dox NPs 2 mM with addition of Na_2SO_4 1 mM (molar ratio SQ-Dox:Na_2SO_4 2:1). Using divalent anion, the SQ-Dox NPs are shorter, and more rigid than with monovalent anion. (Scale bar, 100 nm). (b) Cross-section of a 2 mM SQ-Dox tube with addition of 0.04 mM Na_2SO_4 (Scale bar, 10 nm). (c) Snapshot of equilibrated SQ-Dox tube. Water and ions are not shown for clarity. The colors are the same than in **Figure 1**. (d) Radial density distribution of the SQ chains and Dox heads in the three-layer tubes with SO_4^{2-}. (e) Density map of Dox headgroups. The black rings represent the Dox heads in the cross section of the tube computed over equilibrated part of MD trajectory and symmetrized radially around the center of the tube.
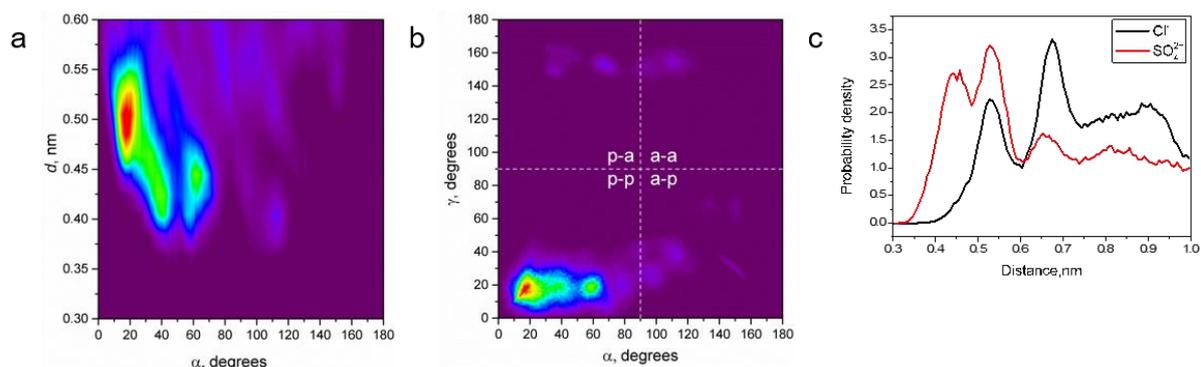
Figure S11. Properties of planar SQ-Dox bilayers. (a) Distance-angle map for the pairs of SQ-Dox rings in equilibrated bilayer. (b) Angle-angle map for the pairs of SQ-Dox rings in equilibrated bilayer. d is the distance between the centers of masses of the rings, α is the angle between long axes of the rings, γ is the angle between normals of the rings. Color shows probability of finding particular combination of parameters (purple correspond to zero, red is the maximum). Dashed lines on the panel separate the quadrants corresponding to different types of stacked aggregates, which are shown near the crossing of these lines. The codes of aggregates correspond to **Figure 2**. (c) Distribution of the distances between N atoms of the sugar in stacked pairs of Dox rings for Cl^- and SO_4^{2-} anions.

In simulated bilayers, different populations of stacked pairs were observed within the p-p pairs with an inclination angle of ~ 20 ° being the most abundant. Minor populations with inclination angles of ~ 40 ° and ~ 60 ° are also present. Other types of pairs (a-a, a-p, p-a) are extremely rare in equilibrated bilayers **(Figure S11a, b)**.

2. Supplementary table

Parameter		SQ-Dox concentration			
		2 mM	4 mM	8 mM	15 mM
λ_D (Å)	In H$_2$O	95.0	67.0	47.5	34.6
	With added NaCl at molar ratio SQ-Dox:NaCl 1:1	54.8	38.7	27.4	/
Volume ratio $\pi(R + \lambda_D)^2 L / \pi R^2 L$ *(R ~ 3.5 nm)*	In H$_2$O	13.8	8.5	5.5	3.95

Table S1: SQ-Dox NPs Debye lengths

3. Supplementary methods

Synthesis of squalenoyl-doxorubicin. Squalenoyl-doxorubicin hydrochloride (SQ-Dox) was synthesized as previously described[2] with some slight modifications. Trimethylorthoformate (0.20 mL, 1.83 mmol) was added to a solution of daunorubicin hydrochloride (**Scheme S1**, 0.20 g, 0.35 mmol) dissolved in methanol/1,4-dioxane (v/v = 1:2, 12 mL). The reaction mixture was then stirred at room temperature for 20 min. To this mixture was further added a $Br_2/CHCl_3$ (w/v =1:9, 0.68 mL, 0.43 mmol) solution. After stirring for 40 min at 30 °C, the resulting solution was poured into dry ether (200 mL) and the solid residue was filtered and washed with ether (50 mL x 3). The solid was recrystallized from acetone/ether (v/v = 1:1, 10 mL), filtered off, washed with ether, and dried over P_2O_5 to give 14-bromo-daunorubicin (4, 0.19 g, 84 %) as a red solid (m.p. 176–177 °C). 14-Bromo-daunorubicin (415.6 mg, 0.625 mmol) and 1,1′,2-tris-norsqualenoic acid (320 mg, 0.80 mmol) were dissolved in acetone (150 mL) under inert Argon atmosphere. Potassium carbonate (260 mg, 1.875mmol) was then added and the reaction mixture was stirred at room temperature for 24 h (dark). The solvent was evaporated and the crude product was purified by silica gel flash column chromatography (95:5, CH_2Cl_2–MeOH) to give a red powder (**Scheme S1**, 365.5 mg, 63 %). The target compound dissolved in anhydrous THF (325 mg in 22 mL) was then converted to hydrochloride salt by adding a anhydrous, titrated 1.64 M solution of HCl in dioxane (1.2 eq, 0.185 ml) and stirring at 20 °C for 2 h. The solvents were then removed and the red solid product was further purified by washing with diisopropylether. The yield of squalenoyl doxorubicin hydrochloride (SQ-Dox) was 303 mg (90 %). The purity of SQ-Dox was checked by SiO_2 TLC eluted CH_2Cl_2:MeOH:HCOOH:H_2O (88:15:2:1, Rf 0,5) and by HPLC-MS. 1H NMR (methanol-d_4): 8.02 (d, 1H, H-3), 7.87 (d, 1H, H-1), 7.70 (t, 1H, , H-2), 5.46 (s, 1H, H-10), 5.3– 5.25 (m, 2H, H-14a, H-14b) and 5.20 (s, 5H, C(sq-H)), 5.19 (s, 1H, H-7), 4.15 (q, 1H, H-50), 4.01 (s, 3H, OCH3), 3.74 (m, 2H, H-30, H-40), 3.24 (d, 1H, H-10), 3.00 (d, 1H, H-10), 2.43 (m, 1H, H-8), 2,29 and 2.35 (s 4H, CH2 SQ acid), 2.13 (m, 1H, H-8), 2.03 (m, 16H, CH2 SQ), 1.97 (m, 1H, H-20), 1.82 (m, 1H, H-20), 1.71 (m, 18H, C(SQ)-CH3), 1.29 (d, 3H, CH3); HPLC: Waters XTerra RP-18 column eluted with water, methanol, (starting 50:50, and then after 7 min gradient up to 100 % methanol, 15 min) plus formic acid 0.05 %, elution time 28.95

min. The elution was monitored at 234 and 480 nm using a Waters 2996 Photodiode Array detector.

ESI MS (Waters micromass) m/z calculated for $[C_{54}H_{71}NO_{12} +H]^+$ 927.14, found 927.2. Elemental

Analysis: calculated C, 67.38; H, 7.54; Cl, 3.68; N, 1.46; found C 67.42; H, 7.61; Cl 3.67; N, 1.42.
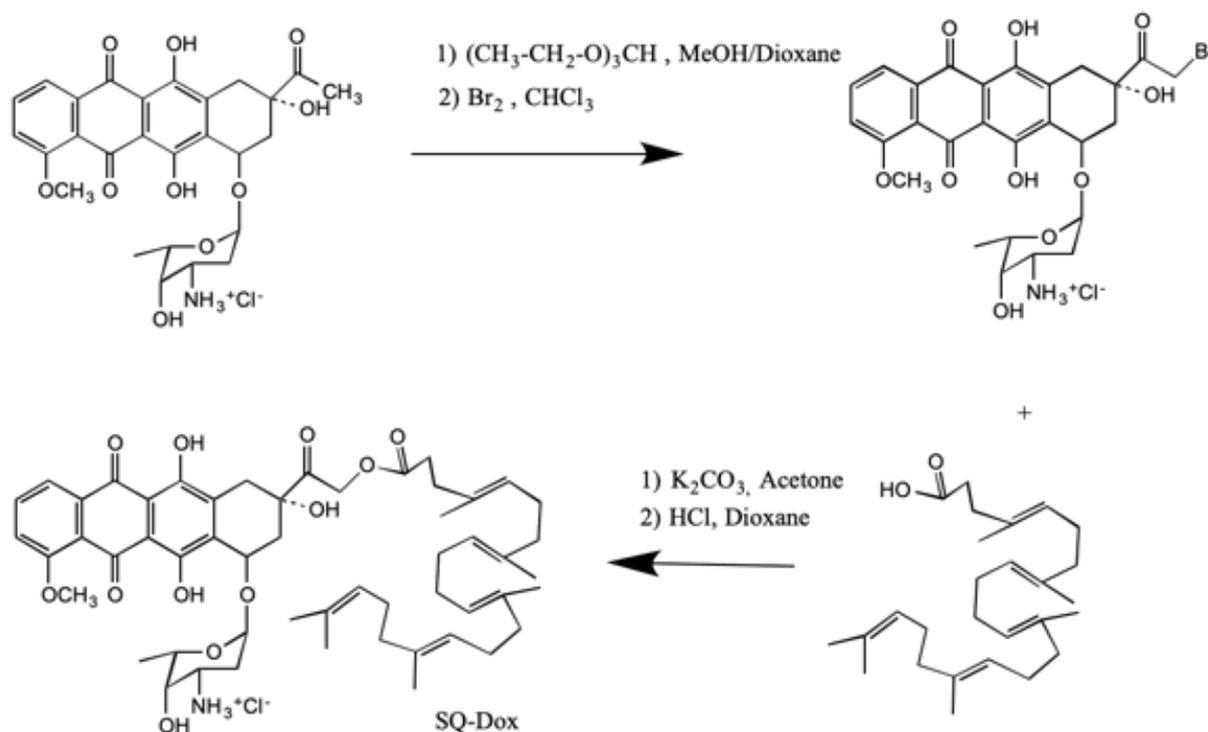
Scheme S1. SQ-Dox synthesis

Spectroscopic characterization of Dox and SQ-Dox. Dox and SQ-Dox solutions were

prepared at a concentration of 104 µM in water and loaded into a quartz cell. Absorbance profiles were

obtained using a LS25 Spectrophotometer (Perkin Elmer). Fluorescence profiles were obtained using a

LS-50B luminescence spectrometer (Perkin Elmer). Samples were excited at 480 nm.

Langmuir Film Balance. The compression properties of a SQ-Dox monolayer were

characterized at a constant temperature of 293K using a computer-controlled KSV-Nima Langmuir-

Blodgett balance coupled to a Wilhelmy plate Device (Biolin Scientific). 100 µL of a 1 mg mL^{-1} SQ-

Dox solution in CHCl$_3$:MeOH (9:1 v:v) was spread onto pure water. After deposition, the solvents

were allowed to evaporate for 10 min before compression of the monolayer at a rate of 5 Å²/molec/min. Experiments were performed at 22 °C.

The compressibility modulus $K = C_s^{-1}$ was deduced from the obtained surface pressure-molecular area (π-A) isotherms using $K = -A \, d\pi/dA$. K is indicative of the physical state of the monolayer: liquid expanded for $13 < K < 100$ mN.m^{-1} and liquid condensed for $100 < K < 250$ mN.m^{-1}

Packing parameter. The packing parameter was defined as $p = V/A_0 l_c$ where V and l_c were the volume and the maximum effective length of the hydrophobic chain, respectively, and A_0 the area per molecule at the amphiphilic molecule-water interface.

The stretched chain length was composed of 10 C-C-C units, with 2.5 Å length, for a total SQ chain length l_c of 25.0 Å **(Figure S12)**.
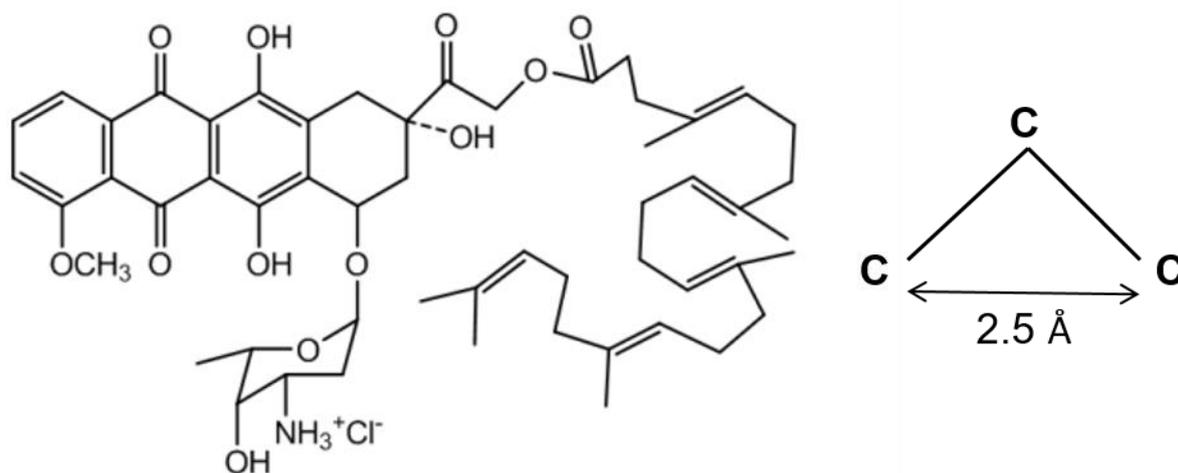

Figure S12. SQ-Dox structure.

The chain volume V was calculated as follow:

$$V = \frac{M}{\mu \cdot N_A}$$

where M was the molar mass of SQ (353 g.mol^{-1}), μ the volumic mass of SQ (8.6 .10^5 g.m^{-3})

105

and N_A the Avogadro number ($6.02 \cdot 10^{23}$ mol^{-1}). The calculated value for V was 681 Å^3.

Ultracentrifugation of SQ-Dox nanoparticles. To attempt to separate the different populations, the SQ-Dox NPs were centrifuged during 2 h at 40 000 g and 20 °C using an Optima CO-LE80K centrifuge equipped with a 70.1 Ti rotor (Beckman Coulter). The obtained pellet and supernatant were characterized by SAXS.

Fitting of SAXS patterns. The software package SASfit was used for the analysis of the SAXS data. The experimental SAXS patterns of SQ-Dox suspensions with or without added NaCl could be fitted using the expression that describes the scattering pattern of non-interacting core-shell cylinders (or core-shell ellipsoidal NPs for 2 mM concentration in the absence of added salt). The parameters are the core radius, the shell width, the cylinder length and the scattering length densities of the core, the shell and the solvent. The scattering intensity depends on the contrast, *i.e.*, on the squared difference in the scattering length density between the core and the shell, on one hand, and the shell and the aqueous medium, on the other hand. The scattering length density is given by $\rho_L = \rho b_e$, where ρ is the electronic density of the medium and be is the Thomson scattering length ($b_e = 0.28179$ x 10^{-12} cm). Homogeneous electronic densities were assumed for the SQ core and the Dox shell. The electronic densities of SQ and water were calculated as $\rho = N_e$ x N_A / V_{mol}, where N_e is the number of electrons in one molecule, N_A the Avogadro constant and V_{mol} the molar volume of the compound **(Table S2)**. In the absence of a known value for the molar volume of Dox, the scattering length density of the Dox shell was determined by fitting of the SAXS curves. Values in the range ~ 1.20 x 10^{11}1.35 x 10^{11} cm^{-2} were obtained for ρ_L(Dox), in good agreement with the electronic density of Dox headgroups in simulated SQ-Dox bilayers. Of note, bound Cl$^-$ ions can increase the scattering length density of the Dox shell. The marked oscillation of I(q) at about q = 0.15 Å^{-1} arises from the contrast between the Dox shell and the SQ core and surrounding water.

Molecule	V_{mol} (cm^3)	N_e (e)	ρ (e/cm^3)	ρ_L (cm^{-2})
H$_2$O	18	10	$3.33 \ 10^{23}$	$0.942 \ 10^{11}$
Squalene (C$_{30}$H$_{50}$)	478	230	$2.90 \ 10^{23}$	$0.816 \ 10^{11}$

Table S2: Electronic densities and scattering lengths calculations.

The wormlike micelle models calculate the form factor for a semi-flexible cylinder with a circular cross-section and a uniform scattering length density. The fit parameters are the cylinder radius, the contour length and the Khun length of the wormlike nanoparticle. The Khun length is $2l_p$ (l_p is the persistence length). The overall contour length, being outside the resolution of the SAXS experiment (~ 100 nm), was fixed to 1000 nm.

Calculation of Debye lengths. The Debye lengths λ_D for SQ-Dox NPs were calculated using $\lambda_D = (\varepsilon_0 \varepsilon_r \ k_B T / 2e^2 I)^{1/2}$ where ε_0 is the vacuum permittivity, ε_r the dielectric constant of water, k_B the Boltzmann constant, T the absolute temperature, e the elementary charge and I the ionic strength. In the absence of added salt, the ionic strength was determined assuming a total dissociation of the Cl$^-$ counter ions. When NaCl was added to SQ-Dox NPs, it was calculated by adding the salt contribution to the ionic strength of the couterions.

Molecular Dynamics

Analysis of SQ-Dox aggregates. For the sake of analysis the SQ-Dox molecule was divided into three structural parts: the "tail" (*i.e.*, the squalene moiety including the linker), the "rings" (the tetracene part of Dox) and the sugar. The distances between the groups were measured as the distances between their centers of masses.

The orientation of the rings was determined by the long and short axes and the normal to tetracene rings, which is a cross product of the former **(Figure S6d)**.

The rings formed stacked aggregates in the course of the simulation and were classified depending on the relative orientations of their long and normal axes. The aggregates were encoded as n-n where the first letter showed whether long axes of two molecules were parallel ("p") or antiparallel ("a") and the second letter showed the same for normal axis. Thus "p-p" means that both axes are parallel, "a-a" means that both of them are antiparallel, *etc*. All four possible types of aggregates are shown in **Figure 2**. Noteworthy, "p-p" stacking in the context of this work only means parallel orientation of involved molecules and should not be mistaken with π-π stacking of π orbitals in general chemical meaning.

Potentials of mean force for stacking interaction. In order to estimate the strength of the stacking interaction between the rings of two SQ-Dox molecules the lone stacked pair was selected in equilibrated cylindrical nanoparticle by visual inspection. The distance between the rings was restrained by harmonic potential with the force constant of 2000 kJ.mol^{-1}.nm^{-2} at equally spaced points from 0.3 nm to 1.0 nm, which resulted in 15 umbrella sampling windows. Each window was simulated for 40 ns and the last 10 ns were used for analysis. The potential of mean force (PMF) was obtained with the weighted histogram technique[3] as implemented in Gromacs package.

Interaction of cylindrical nanoparticles. In order to study the interaction between cylindrical NPs, two pre-equilibrated NPs were arranged parallel to each other. The weak flat-bottom potential with the force constant of 200 kJ.mol^{-1}.nm^{-2} was applied between their centers of masses in XY plain to restrict their diffusion beyond the distance of 5 nm and to keep their surfaces in contact. The system was simulated for 300 ns.

Pre-arranged three-layer bilayer tubes. Three-layer tubes were constructed to mimic the experimentally observed structures. The central part of the tube was modelled by the pre-equilibrated cylindrical micelle. The outer bilayer tube was constructed independently from SQ-Dox molecules arranged into two concentric cylindrical shells with Dox moieties facing internal lumen and outer

solvent respectively. Inner and outer leaflets contained 180 and 300 SQ-Dox molecules respectively. The tube was infinite in Z direction due to periodic boundary conditions. The system was initially solvated with ~32000 water molecules, 446 SO_4^{2-} ions and Na^+ counter ions to achieve electro neutrality. The system was pre-equilibrated in a series of four short simulations (10 ps each). At the end of each such simulation compactization of the bilayer creates a free volume inside the tube, which is isolated from the outer water bath and thus cannot be filled by water molecules. This volume was solvated manually in an iterative manner. After reaching equilibrium water density inside the tube, the inner cylindrical micelle was inserted manually into the lumen. Overlapping water molecules and ions where removed and the system was energy minimized to relax any remaining satirical clashes. After that the system was equilibrated for 100 ns. Last 30 ns were used for analysis.

Technical details. All simulations were performed in Gromacs package versions 5.1.2, 2016.1 and 2018.1.[4] TIP3P water model was used. All simulations were performed in NPT conditions with temperature of 320 K and pressure of 1 bar maintained by v-rescale thermostat and Parrinello-Rahman barostat respectively. The time step of 2 fs was used with all bonds converted to rigid constraints. An integration step of 2 fs was used. Long range electrostatics was computed with the PME method.[5] This choice of the parameters was used with great success in our previous work.[6,7] Preparation of the systems and data analysis was performed with Pteros 2.0 molecular modeling library.[8,9] VMD 1.9.2 was used for visualization.[10]

4. References

(1) Changenet-Barret, P.; Gustavsson, T.; Markovitsi, D.; Manet, I.; Monti, S. Unravelling Molecular Mechanisms in the Fluorescence Spectra of Doxorubicin in Aqueous Solution by Femtosecond Fluorescence Spectroscopy. *Physical Chemistry Chemical Physics* **2013**, *15* (8), 2937–2944.

(2) Maksimenko, A.; Dosio, F.; Mougin, J.; Ferrero, A.; Wack, S.; Reddy, L. H.; Weyn, A.-A.; Lepeltier, E.; Bourgaux, C.; Stella, B.; Cattel, L.; Couvreur, P. A Unique Squalenoylated and Nonpegylated Doxorubicin Nanomedicine with Systemic Long-Circulating Properties and Anticancer Activity. *Proceedings of the National Academy of Sciences* **2014**, *111* (2), E217–E226.

(3) Kumar, S.; Rosenberg, J. M.; Bouzida, D.; Swendsen, R. H.; Kollman, P. A. THE Weighted Histogram Analysis Method for Free-Energy Calculations on Biomolecules. I. The Method. *Journal of Computational Chemistry* **1992**, *13* (8), 1011–1021.

(4) Abraham, M. J.; Murtola, T.; Schulz, R.; Páll, S.; Smith, J. C.; Hess, B.; Lindahl, E. GROMACS: High Performance Molecular Simulations through Multi-Level Parallelism from Laptops to Supercomputers. *SoftwareX* **2015**, *1–2*, 19–25.

(5) Van Der Spoel, D.; Lindahl, E.; Hess, B.; Groenhof, G.; Mark, A. E.; Berendsen, H. J. C. GROMACS: Fast, Flexible, and Free. *Journal of Computational Chemistry* **2005**, *26* (16), 1701–1718.

(6) Yesylevskyy, S. O.; Rivel, T.; Ramseyer, C. The Influence of Curvature on the Properties of the Plasma Membrane. Insights from Atomistic Molecular Dynamics Simulations. *Scientific Reports* **2017**, *7* (1), 16078.

(7) Sobot, D.; Mura, S.; Yesylevskyy, S. O.; Dalbin, L.; Cayre, F.; Bort, G.; Mougin, J.; Desmaële, D.; Lepetre-Mouelhi, S.; Pieters, G.; Andreiuk, B.; Klymchenko, A. S.; Paul, J.-L.; Ramseyer, C.; Couvreur, P. Conjugation of Squalene to Gemcitabine as Unique Approach Exploiting Endogenous Lipoproteins for Drug Delivery. *Nature Communications* **2017**, *8*, 15678.

(8)   Yesylevskyy, S. O. Pteros: Fast and Easy to Use Open-Source C++ Library for Molecular Analysis. *Journal of Computational Chemistry* **2012**, *33* (19), 1632–1636.

(9)   Yesylevskyy, S. O. Pteros 2.0: Evolution of the Fast Parallel Molecular Analysis Library for C++ and Python. *Journal of Computational Chemistry* **2015**, *36* (19), 1480–1488.

(10)   Humphrey, W.; Dalke, A.; Schulten, K. VMD: Visual Molecular Dynamics. *Journal of Molecular Graphics* **1996**, *14* (1), 33–38.

Discussion Générale

The "Squalenoylation" is a nanomedicine technology that emerged a decade ago, consisting in the chemical linkage of a drug to the squalene, a natural and biocompatible lipid precursor of the cholesterol synthesis.[1] Among the wide diversity of bioconjugates developed[2–4], doxorubicin conjugated to squalene (SQ-Dox) represented one of the most promising anticancer nanomedicine.[5] The intravenous injection of SQ-Dox into mice resulted, indeed, in a significantly improved therapeutic efficacy, comparatively to Doxorubicin (DOX) free. Interestingly, SQ-Dox nanoparticles allowed a prolonged circulation time in the bloodstream and a reduced urinary excretion, comparatively to the free drug **(Fig. 1a, c)**, favoring also an improved tumor accumulation of Dox 24 h after injection **(Fig. 1b)**. This resulted in a significantly improved anti-tumor efficacy. Of note, SQ-Dox even displayed a better tumor inhibition than the liposomal formulations Myocet and Caelyx, currently available on the market **(Fig. 1d)**.
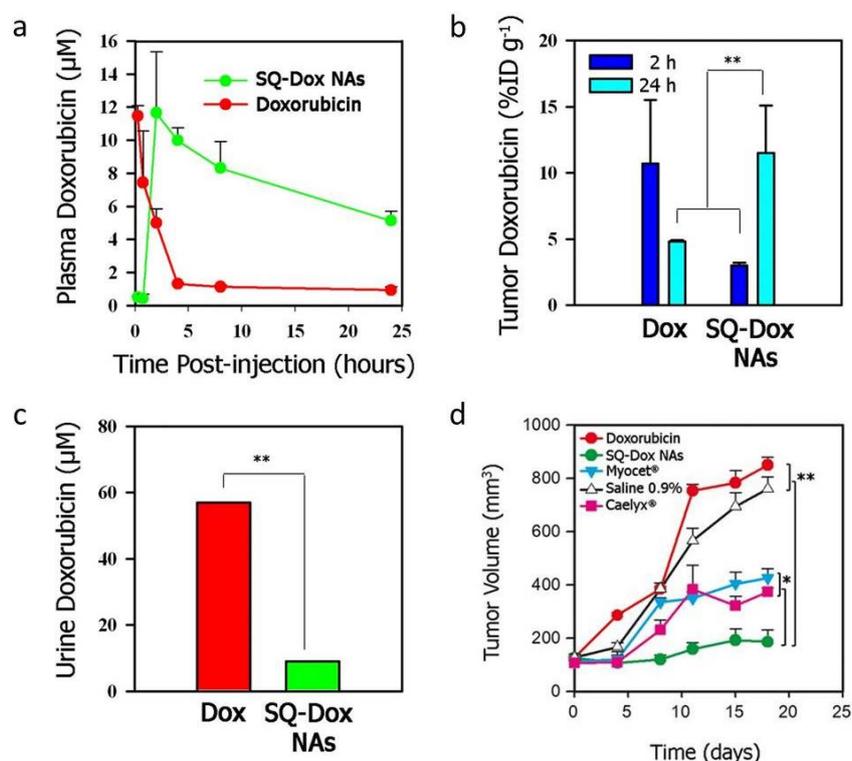

Fig 1: a. Plasma Dox concentration resulting from a single injection of SQ-Dox nanoparticle or free Dox. **b.** Tumor concentration of Dox, 2 h and 24 h after a single injection of either SQ-Dox nanoparticles or free Dox. **c.** Urine Dox concentration, 24 h after administration of a single injection of SQ-Dox nanoparticles or free Dox. **d.** Comparison of the antitumor activity of SQ-Dox nanoparticles with liposomal formulations of doxorubicin (Myocet and Caelyx). Results are reported as means ± SD. Adapted from [5].

On another hand, the main restriction to the use of Dox in cancer therapy is its irreversible cardiotoxicity. Histological analysis of the cardiac tissues confirmed that rats treated with free Dox displayed important myocardial lesions, as shown on **Fig. 2a**. Oppositely, rats treated with SQ-Dox didn't exhibit such damages **(Fig. 2b)**, demonstrating an improved safety of SQ-Dox nanoparticles. This was explained by the decreased heart accumulation of Dox after injection of the SQ-Dox nanomedicine **(Fig. 2c)**.
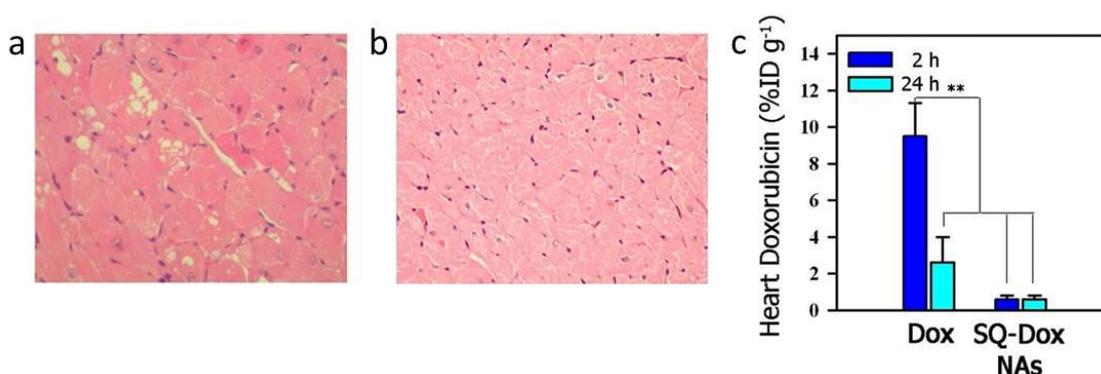

Fig. 2: a. b. HES-stained sections of cardiac tissue (left ventricular inner myocardium) of SH male rats. All tissue images were analyzed by microscopy at 100× magnification (Leica). **a.** Dox-treated rat. **b.** SQ-Dox nanoparticles-treated rat. **c.** Cardiac concentration of Dox, 2 h and 24 h after a single injection of either SQ-Dox nanoparticles or free Dox. Adapted from [5].

Interestingly, SQ-Dox nanoparticles (NPs) displayed original "loop-train" nanostructures, in contrast with all the other squalene-based nanomedicines which displayed spherical shapes. Yet, it has been shown in the literature that elongated nanoparticles can circulate longer in the bloodstream and avoid clearance by the macrophages due to the combination of their ability to extend along the bloodstream[6] and because of the dependence of the cellular uptake on the geometry of the particle at the cell membrane contact point.[7,8] Consequently, the improved anticancer activity of SQ-Dox NPs over free Dox has been attributed to their specific elongated shape. Based on these observations, the aim of the present thesis was to elucidate the physico-chemical mechanisms implied in the formation of these elongated SQ-Dox NPs.

I. Preparation and characterization of SQ-Dox nanoparticles

1. Characteristics of SQ-Dox nanoparticles in water

SQ-Dox NPs were prepared at a concentration of 2 mM following the usual nanoprecipitation method.[5] However, instead of the expected loop-train shape, cryo-TEM pictures of the obtained suspensions revealed spherical particles and very rare filaments, both with a diameter of ~ 5 nm **(Chapter 2, Fig. 1a)**. Consequently, the first step of the present study was to standardize the formulation method, allowing to better identify the parameters controlling the shape of the SQ-Dox NPs. However, despite the variation of an important number of parameters at each step of the formulation process (nature and/or volume of the organic phase, rate of addition of the organic phase into the aqueous phase, rotation speed and size of the magnetic stirrer, solvent evaporation rate and temperature, *etc*), the size and shape of the NPs remained unchanged.

The packing parameter p was then investigated to determine the preferred shape of the SQ-Dox assembly. The squalene chain length and volume were calculated **(Chapter 2, Supplementary Methods),** while the SQ-Dox mean molecular area was obtained from Langmuir monolayer isotherm **(Chapter 2, Fig. S8a)**. Those data gave a p value of 0.51, yet clearly confirming the ability of SQ-Dox to assemble into cylindrical NPs.[9] SAXS analysis eventually shed light on the NPs shape: the NPs SAXS pattern could be fitted by a model of prolate ellipsoids **(Chapter 2, Fig. 1c)**.

2. Formation of SQ-Dox cylinders

Interestingly, increasing the concentration of NPs in suspension resulted in a drastic change in the NPs morphology. Indeed, cryo-TEM pictures and SAXS patterns revealed a high amount of cylinders with 2 populations of diameters ~ 5 nm and ~ 11.7 nm, the latter apparently resulting from the merging of the former **(Chapter 2, Fig. 1b, c)**. This elongation process was compared to the sphere-to-rod transition, sometimes observed with surfactant micelles, for which uniaxial growing of micelles occurred once the critical transition concentration (CTC) is overcome.[10] The structure and

dimensions of the obtained nanoworms were remarkably confirmed by molecular dynamics simulations **(Chapter 2, Fig. 1c-f)**, which also revealed the role of the π-π stacking properties of the Dox moiety[11,12]. This stacking was experimentally confirmed at SQ-Dox concentrations as low as 5 µM, well below the concentration of the SQ-Dox bioconjugate in the NPs suspensions **(Chapter 2, Fig. S5)**. The surface topology of the SQ-Dox cylinders was then fully described, highlighting various populations of stacks with different implications in the self-assembling behavior of SQ-Dox **(Chapter 2, Fig. 2, S6, S7)**.

3. Rheology of SQ-Dox cylinders

Geng *et al*. have demonstrated that up to a critical length, the longer worm-like particles had a more prolonged circulation time in the blood stream.[6] We couldn't accurately determine this value for SQ-Dox, neither by cryo-TEM due to the entanglement of particles on the pictures, nor by SAXS due to the resolution of the technique. However, rheology techniques, through the analysis of the storage and elastic moduli G'(ω) and G''(ω), respectively, may allow to access this parameter.[13] Furthermore, it is known that the zero-shear viscosity drastically increases when worm-like particles are formed[14], so rheology was also used to precisely determine the CTC.

The viscosity of SQ-Dox NPs suspension with varying concentration was monitored using an AR-G2 cone-plan rheometer (40 mm diameter, 1 ° cone angle, TA Instruments). However, the curves obtained after monitoring of G'(ω) and G''(ω) for SQ-Dox NPs prepared at 4 mM were not characteristic of worm-like systems and didn't allow the calculation of the length of SQ-Dox cylinders. During these experiments, several other limitations were encountered. First, the viscosity of the samples was very low, of the same order of magnitude than pure water, even at SQ-Dox concentrations for which cryo-TEM clearly showed elongated NPs. Due to this low viscosity, the values obtained for low shear rates lacked precision and didn't exhibit the characteristic plateau of worm-like micelles, used to extrapolate the zero-shear viscosity. Additionally, viscosity measurements

were not reproducible on the same sample. This could be the result of the degradation of the SQ-Dox cylinders. Consequently, we couldn't use either rheology to determine the CTC of SQ-Dox.

II. Effect of the addition of salts

We then managed to form elongated SQ-Dox NPs by increasing the bioconjugate concentration but it was not possible to obtain the loop-train shape initially observed by Maksimenko *et al*.[5] We made the hypothesis that those structures could derive from a superior degree of packing of SQ-Dox. Alternatively to the augmentation of the SQ-Dox concentration, other common methods to trigger the elongation of cylindrical particles based on ionic surfactants consist in the addition of electrolytes to screen the repulsive interactions between the surfactant molecules.[15] Therefore, we have used this approach in an attempt to screen also the repulsions between SQ-Dox cylinders and to trigger a possible aggregation into loop-train particles. Practically, two anionic counterions were considered: monovalent Cl^- and divalent SO_4^{2-}.

1. Action of monovalent anion

The addition of NaCl to a suspension of SQ-Dox NPs has led to an impressive increase in the amount of cylinders, displaying the same structures than the few cylinders previously seen in water **(Chapter 2, Fig. 3)**. SAXS experiments revealed that the larger aggregates, with diameter ~12 nm, could derive from side-by-side aggregation of thin cylinders, through the formation of inter-particle a-a and a-p stacking pairs through a "zipper-like" mechanism. The combination of AFM with MD simulations could highlight the helical conformation of such aggregates. Those techniques also evidenced the helical twisting of those aggregates **(Chapter 2, Fig. 3b, S9)**. And the ability of Cl^- to screen the repulsive interactions, first between SQ-Dox molecules, then between SQ-Dox NPs has been confirmed. Increasing NaCl concentration in the medium didn't alter the supramolecular core-

shell organization of SQ-Dox but seems to fasten both the stacking of Dox headgroups to help the elongation of NPs, and the stacking of Dox cylinders.

2. Action of divalent anion

Interestingly, the addition of a divalent salt (Na_2SO_4) to the SQ-Dox NPs suspension triggered a transition from cylinders to rigid bilayer nanotubes, as those two types of aggregates coexisted at low Na_2SO_4 concentrations (**Fig. 3a**, **Chapter 2, Fig. 5**). The mechanism for this transition remains still unclear but probably derives from the ability of divalent salts to form intermolecular bridges, helping a tight packing of SQ-Dox molecules, especially because SO_4^{2-} anions are known to favor pronounced self-association of Dox headgroups.[16] The Langmuir isotherms of SQ-Dox monolayer with addition of salts in the sub-phase tended to confirm this hypothesis. While isotherms and compression modulus K obtained for water and NaCl were very similar (**Fig. 3b, c, Table 1**), those obtained with Na_2SO_4 were clearly different. For this reason, we could not use the slope of the isotherms to determine the mean molecular area but we compared instead the areas obtained at a surface pressure of 30 mN.m^{-1}, representative of the pressure inside cell membranes. At such pressure, the molecular area of SQ-Dox was slightly lower in the presence of Na_2SO_4 and so was the corresponding compressibility modulus K value (**Table 1**). Altogether, these results were relevant with the stronger packing promoted by the dianions.

Sub-phase	$A_{30 \text{ mN.m}}^{-1}$ (Å²)	K_{max} (mN.m^{-1})
H_2O	47.7	~ 92.4
NaCl (1 mM)	47.2	~ 93.3
Na_2SO_4 (1 mM)	43.1	~ 61.3

Table 1: Molecular area of SQ-Dox at 30 mN.m^{-1} and maximum value of compressibility modulus K depending on the sub-phase nature.

The mechanism of formation of the SQ-Dox bilayer nanotubes could be considered as follows: by analogy with Yang *et al.*'s study[17], SO_4^{2-} form SQ-Dox dimers, further stacking together by means of both π-π interactions between Dox headgroups and squalene-squalene interactions, allowing the growth of aggregates in two dimensions. The bilayer could then be completed by association of two monolayers through hydrophobic interactions between squalene chains. Then, some nanotubes appear to be filled with simple SQ-Dox cylinders **(Chapter 2, Fig. S10)** and this was made possible by additional SO_4^{2-} bridges between Dox heads from the cylinder and the nanotube.
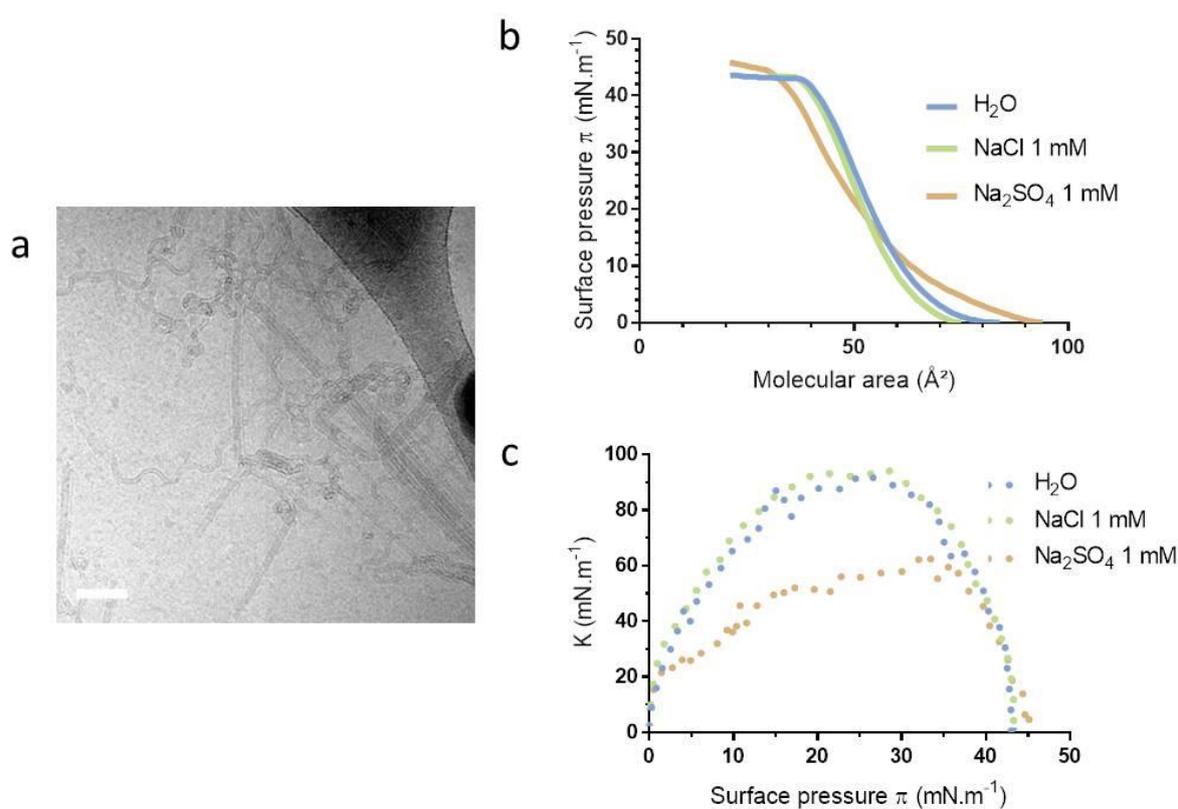

Fig. 3: a. Cryo-TEM picture of SQ-Dox NPs prepared at 2 mM with addition of 0.1 mM Na_2SO_4. **b.c.** SQ-Dox monolayer properties with water, NaCl (1 mM) or Na_2SO_4 (1 mM) in the sub-phase. **b.** Surface-pressure molecular area compression isotherm. **c.** Compressibility modulus K as a function of the pressure.

Based on all these findings, the presumed self-assembly mechanism of SQ-Dox has been summed up in **Fig. 4**.
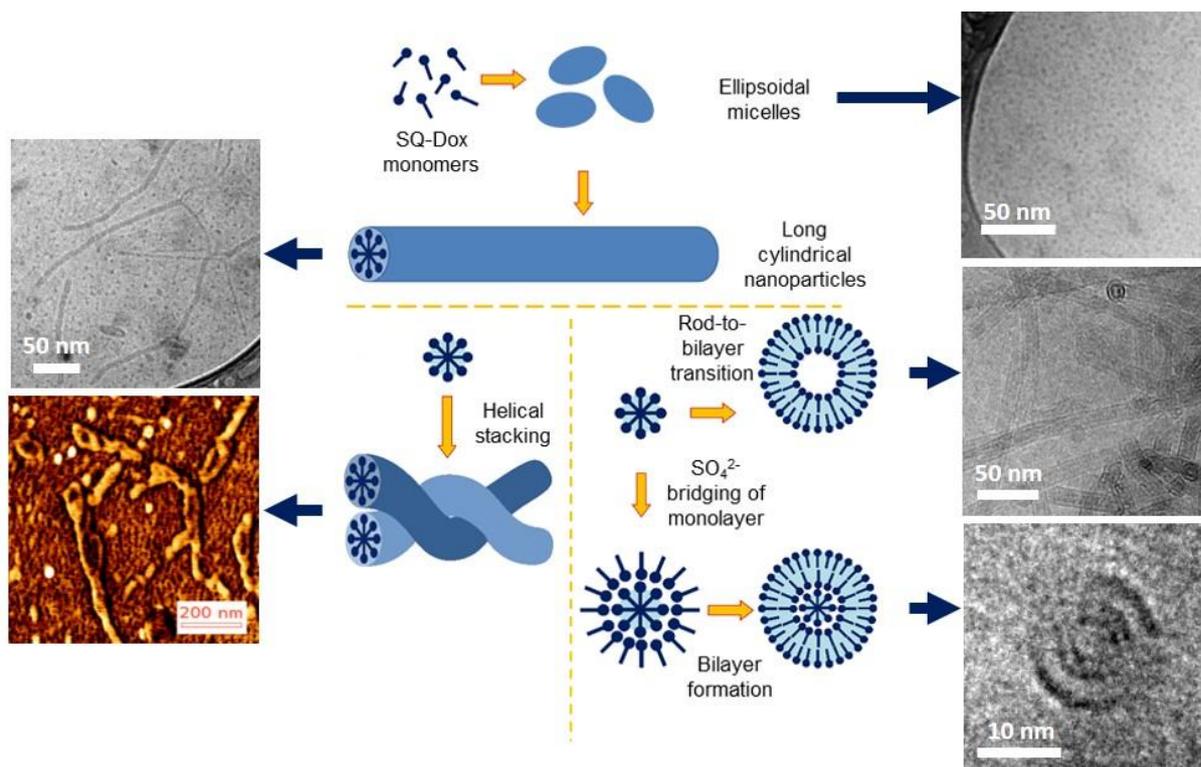
Fig. 4: Self-assembly mechanism of SQ-Dox.

3. Salt action as a possible issue in biological environments

As shown in this thesis, it is now quite possible to control the shape of SQ-Dox NPs by simple means: concentration of SQ-Dox and nature and concentration of salts. Comparing their relative therapeutic efficacy could confirm the link between SQ-Dox anticancer efficacy and preferred shape of assembly. However, our study shows that the structure of NPs could be drastically altered after injection into complex medium such as blood with important salts concentration. In other words, the NPs in the tube and in the body are not the same. And it is likely that short SQ-Dox ellipsoids in water will lose their shape and elongate after intravenous administration. But once the SQ-Dox elongated particles are formed, they seem rather stable, as they can still be found in suspension after dilution **(Chapter 2, Fig S1b, c)**, or dialysis of the added salts **(Fig. 5)**.
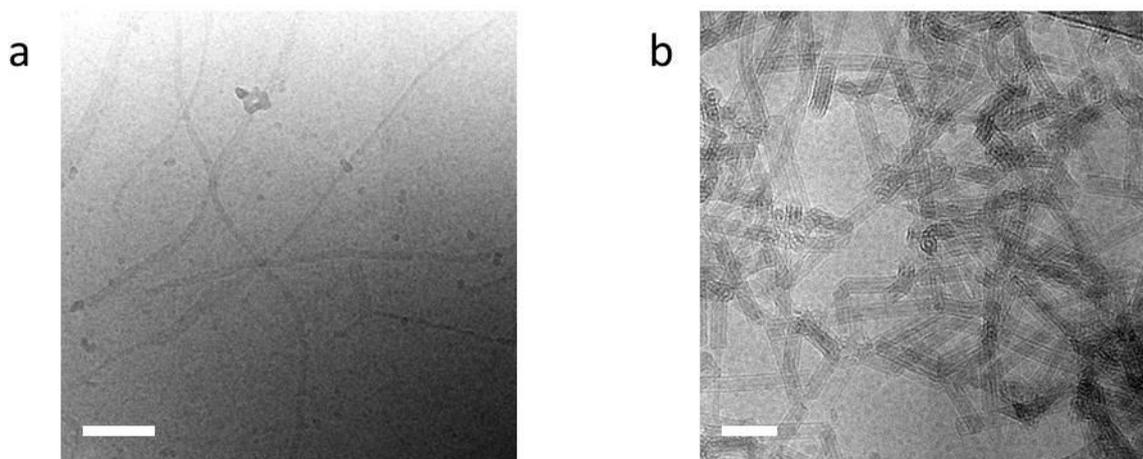
Fig 5: Cryo-TEM pictures of SQ-Dox NPs prepared at 2 mM after dialysis of the added salts (dialysis membrane 100-500 kDa MWCO). SQ-Dox NPs prepared with **a.** NaCl 2 mM (scale bar, 100 nm). **b.** Na_2SO_4 0.4 mM (scale bar, 50 nm).

III. π-π stacking as a key property, but not the only one?

It has been demonstrated in this thesis that the elongated shape of SQ-Dox derived from the π-π stacking properties of Dox. However, if this feature seems to be crucial, it is not enough to ensure the formation of cylindrical NPs, as other squalene-based bioconjugates with stacking properties didn't assemble into such elongated shapes. Indeed, in this study, we have focused on the ammonium salt of SQ-Dox. But other preliminary experiments have shown that the non-ionic amine form of SQ-Dox assembled into spherical NPs **(Fig. 6)**. And other π-π forming squalene bioconjugates such as squalenoyl-paclitaxel[18] or squalenoyl-adenosine (SQ-Ad)[3] also formed spheres, instead of elongated structures. And those two bioconjugates are non-ionic molecules in physiological conditions. Thus, the presence of a charge on the headgroup could be another condition necessary for squalene-based cylinders to be obtained. This would deserve further investigation.
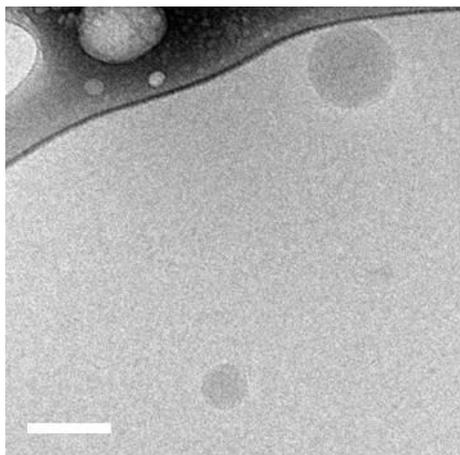
Fig. 6: Cryo-TEM picture of basic SQ-Dox (scale bar, 100 nm).

Interestingly, Baglioni's group managed to obtain adenosine-based cylindrical particles, depending on the length of the chain conjugated to the drug[19,20]. In their study, these authors grafted phosphatidylcholines of different lengths onto the primary alcohol group of adenosine to obtain 1,2-dioctanoyl-sn-glycero-3-phosphatidyladenosine (diC$_8$PA) or 1,2-dilauroyl-sn-glycero-3-phosphatidyladenosine (DLPA) as ammonium salts. As for SQ-Dox, in these examples, the amine function was protonated at physiological pH, while in the case of Ad-Sq, the squalene chain is grafted onto the amine group, hence hindering its ionization. And DiC$_8$PA formed spherical micelles, while DLPA formed cylindrical ones. Altogether, these observations highlight the influence of both the chain length and position on the shape of the nanoassemblies.

IV. Towards a screening tool?

We have identified the π-π stacking property of the parent drug as a key parameter to form elongated NPs. However, this condition is not enough as other examples of the literature suggest that the charge of the headgroup, as well as the hydrophobic chain length and position may be involved. In the case of SQ-Dox, MD simulations were in excellent agreement with the experimental results, giving crucial details about the supramolecular organization inside the SQ-Dox NPs. Consequently, MD could further be considered as an interesting tool to screen potential candidates for the design of NPs with specific shapes.

V. Conclusion and perspectives

The initial aim of this thesis was to understand the mechanism behind the self-assembly of SQ-Dox bioconjugates into elongated structures. We were able to demonstrate the following points:

- the self-assembly mechanism of SQ-Dox has been elucidated,

- the shape of SQ-Dox particles could be modified by the addition of salts of different nature,

- the π-π stacking ability of parent drug has been identified as a necessary parameter to form cylindrical NPs, but it is not the only one, as other bioconjugates with similar properties do not systemically behave in the same way.

However, additional investigations remain to be done, before to generalize this concept to other bioconjugates. In particular, the following studies should be considered:

- the screening of new bioconjugates based on other π-π drugs (camptothecin, coumarin, *etc*) and different alkyl chains to more precisely predict the shape of the obtained nanomedicine, depending on the molecular characteristics,

- the evaluation of the therapeutic efficacy of the different shapes of SQ-Dox NPs to validate the previously assumed relationship between structure and anticancer efficacy.

VI. References

(1)   Couvreur, P.; Stella, B.; Reddy, L. H.; Hillaireau, H.; Dubernet, C.; Desmaële, D.; Lepêtre-Mouelhi, S.; Rocco, F.; Dereuddre-Bosquet, N.; Clayette, P.; Rosilio, V.; Marsaud, V.; Renoir, J.-J.; Cattel, L. Squalenoyl Nanomedicines as Potential Therapeutics. *Nano Letters* **2006**, *6* (11), 2544–2548.

(2)   Kotelevets, L.; Chastre, E.; Caron, J.; Mougin, J.; Bastian, G.; Pineau, A.; Walker, F.; Lehy, T.; Desmaële, D.; Couvreur, P. A Squalene-Based Nanomedicine for Oral Treatment of Colon Cancer. *Cancer Research* **2017**, *77* (11), 2964–2975.

(3)   Gaudin, A.; Yemisci, M.; Eroglu, H.; Lepetre-Mouelhi, S.; Turkoglu, O. F.; Dönmez-Demir, B.; Caban, S.; Sargon, M. F.; Garcia-Argote, S.; Pieters, G.; Loreau, O.; Rousseau, B.; Tagit, O.; Hildebrandt, N.; Le Dantec, Y.; Mougin, J.; Valetti, S.; Chacun, H.; Nicolas, V.; Desmaële, D.; *et al*. Squalenoyl Adenosine Nanoparticles Provide Neuroprotection after Stroke and Spinal Cord Injury. *Nature Nanotechnology* **2014**, *9* (12), 1054–1062.

(4)   Feng, J.; Lepetre-Mouelhi, S.; Gautier, A.; Mura, S.; Cailleau, C.; Coudore, F.; Hamon, M.; Couvreur, P. A New Painkiller Nanomedicine to Bypass the Blood-Brain Barrier and the Use of Morphine. *Sci. Adv.* **2019**, *5* (2), eaau5148.

(5)   Maksimenko, A.; Dosio, F.; Mougin, J.; Ferrero, A.; Wack, S.; Reddy, L. H.; Weyn, A.-A.; Lepeltier, E.; Bourgaux, C.; Stella, B.; Cattel, L.; Couvreur, P. A Unique Squalenoylated and Nonpegylated Doxorubicin Nanomedicine with Systemic Long-Circulating Properties and Anticancer Activity. *Proceedings of the National Academy of Sciences* **2014**, *111* (2), E217–E226.

(6)   Geng, Y.; Dalhaimer, P.; Cai, S.; Tsai, R.; Tewari, M.; Minko, T.; Discher, D. E. Shape Effects of Filaments versus Spherical Particles in Flow and Drug Delivery. *Nature Nanotechnology* **2007**, *2* (4), 249–255.

(7)   Champion, J. A.; Mitragotri, S. Role of Target Geometry in Phagocytosis. *Proceedings of the National Academy of Sciences* **2006**, *103* (13), 4930–4934.

(8)   Champion, J. A.; Mitragotri, S. Shape Induced Inhibition of Phagocytosis of Polymer Particles. *Pharmaceutical Research* **2009**, *26* (1), 244–249.

(9)   Israelachvili, J.; Ladyzhinski, I. The Physico-Chemical Basis of Self-Assembling Structures. In *Forces, Growth and Form in Soft Condensed Matter: At the Interface between Physics and Biology*; Skjeltorp, A. T., Belushkin, A. V., Eds.; Kluwer Academic Publishers: Dordrecht, 2005; Vol. 160, pp 1–28.

(10)   Ben-Shaul, A.; May, S. Molecular Packing in Cylindrical Micelles. In *Giant Micelles*; Kaler, E., Zana, R., Eds.; CRC Press, 2007; Vol. 20074445, pp 41–79.

(11)   Menozzi, M.; Valentini, L.; Vannini, E.; Arcamone, F. Self-Association of Doxorubicin and Related Compounds in Aqueous Solution. *Journal of Pharmaceutical Sciences* **1984**, *73* (6), 766–770.

(12)   Agrawal, P.; Barthwal, S. K.; Barthwal, R. Studies on Self-Aggregation of Anthracycline Drugs by Restrained Molecular Dynamics Approach Using Nuclear Magnetic Resonance Spectroscopy Supported by Absorption, Fluorescence, Diffusion Ordered Spectroscopy and Mass Spectrometry. *European Journal of Medicinal Chemistry* **2009**, *44* (4), 1437–1451.

(13)   Zhao, M.; Zhang, Y.; Zou, C.; Dai, C.; Gao, M.; Li, Y.; Lv, W.; Jiang, J.; Wu, Y. Can More Nanoparticles Induce Larger Viscosities of Nanoparticle-Enhanced Wormlike Micellar System (NEWMS)? *Materials* **2017**, *10* (9), 1096.

(14)   Nagarajan, R.; Shah, K. M.; Hammond, S. Viscometric Detection of Sphere to Cylinder Transition and Polydispersity in Aqueous Micellar Solutions. *Colloids and Surfaces* **1982**, *4* (2), 147–162.

(15)   Porte, G.; Appell, J. Growth and Size Distributions of Cetylpyridinium Bromide Micelles in High Ionic Strength Aqueous Solutions. *The Journal of Physical Chemistry* **1981**, *85* (17), 2511–2519.

(16)   Salay, L. C.; Schreier, S. Effect of a Kosmotropic Ion on Doxorubicin Self-Assembly and Interaction with Biomimetic Systems. In *Surface and Colloid Science*; Springer Berlin Heidelberg: Berlin, Heidelberg, 2004; pp 156–158.

(17)   Yang, C.; Wu, D.; Zhao, W.; Ye, W.; Xu, Z.; Zhang, F.; Feng, X. Anion-Induced Self-Assembly of Positively Charged Polycyclic Aromatic Hydrocarbons towards Nanostructures with Controllable Two-Dimensional Morphologies. *CrystEngComm* **2016**, *18* (6), 877–880.

(18)   Caron, J.; Maksimenko, A.; Wack, S.; Lepeltier, E.; Bourgaux, C.; Morvan, E.; Leblanc, K.; Couvreur, P.; Desmaële, D. Improving the Antitumor Activity of Squalenoyl-Paclitaxel Conjugate Nanoassemblies by Manipulating the Linker between Paclitaxel and Squalene. *Advanced Healthcare Materials* **2013**, *2* (1), 172–185.

(19)   Berti, D.; Baldelli Bombelli, F.; Fortini, M.; Baglioni, P. Amphiphilic Self-Assemblies Decorated by Nucleobases. *The Journal of Physical Chemistry B* **2007**, *111* (40), 11734–11744.

(20)   Baldelli Bombelli, F.; Berti, D.; Milani, S.; Lagi, M.; Barbaro, P.; Karlsson, G.; Brandt, A.; Baglioni, P. Collective Headgroup Conformational Transition in Twisted Micellar Superstructures. *Soft Matter* **2008**, *4* (5).

Publications

2019 :

- **Mougin, J**.; Yesylevskyy, S. O.; Bourgaux, C.; Chapron, D.; Michel, J.-P.; Dosio, F.; Stella, B.; Ramseyer, C.; Couvreur, P. Stacking as a Key Property for Creating Nanoparticles with Tunable Shape: The Case of Squalenoyl-Doxorubicin, *ACS Nano* **2019,** *13* (11), 12870-12879.

- Vinciguerra, D.; Jacobs, M.; Denis, S.; **Mougin, J**.; Guillaneuf, Y.; Lazzari, G.; Zhu, C.; Mura, S.; Couvreur, P.; Nicolas, J. Heterotelechelic Polymer Prodrug Nanoparticles: Adaptability to Different Drug Combinations and Influence of the Dual Functionalization on the Cytotoxicity*, Journal of Controlled Release* **2019**, *295*, 223-236.

- Rouquette, M.; Lepetre-Mouelhi, S.; Dufrançais, O.; Yang, X.; **Mougin, J.;** Pieters, G.; Garcia-Argote, S.; IJzerman A. P.; Couvreur, P. Squalene-Adenosine Nanoparticles: Ligands or Prodrug?, *Journal of Pharmacology and Experimental Therapeutics* **2019**, *369* (1), 144-151.

- Vinciguerra, D. ; Degrassi, A.; Mancini, L.; Mura, S.; **Mougin, J.;** Couvreur, P.; Nicolas, J. Drug-Initiated Synthesis of Heterotelechelic Polymer Prodrug Nanoparticles for in Vivo Imaging and Cancer Cell Targeting, *Biomacromolecules* **2019**, *20* (7), 2464-2476.

2018 :

- Bao, Y.; Guégain, E.; **Mougin J.**; Nicolas, J. Self-stabilized, Hydrophobic or PEGylated Paclitaxel Polymer Prodrug Nanoparticles for Cancer Therapy, *Polymer Chemistry* **2018**, *9* (6), 687-698.

- Vinciguerra, D.; Denis, S.; **Mougin, J.**; Jacobs, M.; Guillaneuf, Y.; Mura, S.; Couvreur, P.; Nicolas, J. A Facile Route to Heterotelechelic Polymer Prodrug Nanoparticles for Imaging, Drug Delivery and Combination Therapy, *Journal of Controlled Release* **2018**, *286*, 425-438.

2017 :

- Sobot, D., Mura, S., Yesylevskyy, S. O.; Dalbin, L.; Cayre, F.; Bort, G.; **Mougin, J.**; Desmaële, D.; Lepetre-Mouelhi, S.; Pieters, G.; Andreiuk, B.; Klymchenko, A. S.; Paul, J.-P.; Ramseyer, C.; Couvreur, P. Conjugation of Squalene to Gemcitabine as Unique Approach Exploiting Endogenous Lipoproteins for Drug Delivery. *Nature Communications* **2017**, *8*, 15678.

- Kotelevets, L.; Chastre, E.; Caron, J.; **Mougin, J.**; Bastian, G.; Pineau, A.; Walker, F.; Lehy, T.; Desmaële, D.; Couvreur, P. A Squalene-Based Nanomedicine for Oral Treatment of Colon Cancer, *Cancer Research* **2017**, *77* (11), 2964-2975.

2016 :

- Mura, S.; Buchy, E.; Askin, G.; Cayre, F.; **Mougin, J.**; Gouazou, S.; Sobot, D.; Valetti, S.; Stella, B.; Desmaële, D.; Couvreur, P. *In Vitro* Investigation of Multidrug Nanoparticles for Combined Therapy with Gemcitabine and a Tyrosine Kinase Inhibitor: Together Is Not Better, *Biochimie* **2016**, *130*, 4-13.

2015 :

- Gaudin, A.; Lepetre-Mouelhi, S.; **Mougin, J.**; Parrod, M.; Pieters, G.; Garcia-Argote, S.; Loreau, O.; Goncalves, J.; Chacun, H.; Courbebaisse, Y.; Clayette, P.; Desmaële, D.; Rousseau, B.; Andrieux, K.; Couvreur, P. Pharmacokinetics, Biodistribution and Metabolism of Squalenoyl Adenosine Nanoparticles in Mice Using Dual Radio-Labeling and Radio-HPLC Analysis, *Journal of Controlled Release* **2015**, *212*, 50-58.

- Abed, N.; Saïd-Hassane, F.; Zouhiri, F.; **Mougin, J.**; Nicolas, V.; Desmaële, D.; Gref, R.; Couvreur, P. An Efficient System for Intracellular Delivery of Beta-Lactam Antibiotics to Overcome Bacterial Resistance, *Scientific Reports* **2015**, *5* (1), 13500.

128

- Gaudin, A.; Tagit, O.; Sobot, D.; Lepetre-Mouelhi, S.; **Mougin, J.**; Martens, T. F.; Braeckmans, K.; Nicolas, V.; Desmaële, D.; de Smedt, S. C.; Hildebrandt, N.; Couvreur, P.; Andrieux, K. Transport Mechanisms of Squalenoyl-Adenosine Nanoparticles Across the Blood–Brain Barrier, *Chemistry of Materials* **2015**, *27* (10), 3636-3647.

- Maksimenko, A.; Caron, J.; **Mougin, J.**; Desmaële, D.; Couvreur, P. Gemcitabine-Based Therapy for Pancreatic Cancer Using the Squalenoyl Nucleoside Monophosphate Nanoassemblies, *International Journal of Pharmaceutics* **2015**, *482* (1-2), 38-46.

- Buchy, E.; Valetti, S.; Mura, S.; **Mougin, J.**; Troufflard, C.; Couvreur, P.; Desmaële, D. Synthesis and Cytotoxic Activity of Self-Assembling Squalene Conjugates of 3-[(Pyrrol-2-yl)methylidene]-2,3-dihydro-1H-indol-2-one Anticancer Agents: Self-Assembling Squalene Conjugates of Anticancer Agents, *European Journal of Organic Chemistry* **2015**, 20*15* (1), 202-212.

2014 :

- Gaudin, A.; Yemisci, M.; Eroglu, H.; Lepetre-Mouelhi, S.; Turkoglu, O. F.; Dönmez-Demir, B.; Caban, S.; Sargon, M. F.; Garcia-Argote, S.; Pieters, G.; Loreau, O.; Rousseau, B.; Tagit, O.; Hildebrandt, N.; Le Dantec, Y.; **Mougin, J.**; Valetti, S.; Chacun, H.; Nicolas, V.; Desmaële, D.; Andrieux, K.; Capan, Y.; Dalkara, T.; Couvreur, P. Squalenoyl Adenosine Nanoparticles Provide Neuroprotection After Stroke and Spinal Cord Injury, *Nature Nanotechnology* **2014**, *9* (12), 1054-1062.

- Mackiewicz, N.; Nicolas, J.; Handké, N.; Noiray, M.; **Mougin, J.**; Daveu, C.; Lakkireddy, H. R.; Bazile, D.; Couvreur, P. Precise Engineering of Multifunctional PEGylated Polyester Nanoparticles for Cancer Cell Targeting and Imaging, *Chemistry of Materials* **2014**, *26* (5), 1834-1847.

- Maksimenko, A.; Alami, M.; Zouhiri, F.; Brion, J.-D.; Pruvost, A.; **Mougin, J.**; Hamze, A.; Boissenot, T.; Provot, O.; Desmaële, D.; Couvreur, P. Therapeutic Modalities of Squalenoyl

Nanocomposites in Colon Cancer: An Ongoing Search for Improved Efficacy, *ACS Nano* **2014**, *8* (3), 2018-2032.

- Caron, J.; Maksimenko, A.; **Mougin, J.**; Couvreur, P.; Desmaële, D. Combined Antitumoral Therapy with Nanoassemblies of Bolaform Polyisoprenoyl Paclitaxel/Gemcitabine Prodrugs, *Polymer Chemistry* **2014**, *5* (5), 1662-1673.

- Maksimenko, A.; Dosio, F.; **Mougin, J.**; Ferrero, A.; Wack, S.; Reddy, L. H.; Weyn, A.-A.; Lepeltier, E.; Bourgaux, C.; Stella, B.; Cattel, L.; Couvreur, P. A Unique Squalenoylated and Nonpegylated Doxorubicin Nanomedicine with Systemic Long-Circulating Properties and Anticancer Activity. *Proceedings of the National Academy of Sciences* **2014**, *111* (2), E217–E226.

2013 :

- Mura, S.; Zouhiri, F.; Lerondel, S.; Maksimenko, A.; **Mougin, J.**; Gueutin, C.; Brambilla, D.; Caron, J.; Sliwinski, E.; LePape, A.; Desmaële, D.; Couvreur, P. Novel Isoprenoyl Nanoassembled Prodrug for Paclitaxel Delivery, *Bioconjugate Chemistry* **2013**, *24* (11), 1840-1849.

- Maksimenko, A.; **Mougin, J.**; Mura, S.; Sliwinski, E.; Lepeltier, E.; Bourgaux, C.; Lepetre, S.; Zouhiri, F.; Desmaële, D.; Couvreur, P. Polyisoprenoyl Gemcitabine Conjugates Self Assemble as Nanoparticles, Useful for Cancer Therapy, *Cancer Letters* **2013**, *334* (2), 346-353.

- Harrisson, S.; Nicolas, J.; Maksimenko, A.; Bui, D. T.; **Mougin, J.**; Couvreur, P. Nanoparticles with In Vivo Anticancer Activity from Polymer Prodrug Amphiphiles Prepared by Living Radical Polymerization, *Angewandte Chemie-International Edition* **2013**, *52* (6), 1678-1682.

Titre : Contribution à l'étude physico-chimique de nanomédicaments squalénés pour le traitement du cancer

Mots clés : Nanomédecine; Squalène, Doxorubicine, Bioconjugué, Cancer, Délivrance de médicaments

Résumé : De précédents travaux menés au sein de l'équipe du Pr. Patrick Couvreur (Institut Galien Paris-Sud) ont permis de développer des nanoparticules thérapeutiques formées par un bioconjugué issu du couplage entre un agent anti-cancéreux, la doxorubicine chlorhydrate, et un lipide naturel et biocompatible, le squalène. Par comparaison avec la doxorubicine libre, ces nanomédicaments présentent une activité anticancéreuse accrue, un temps de circulation plasmatique prolongé et une toxicité cardiaque fortement diminuée, alors que celle-ci représente l'une des principales limitations à l'utilisation de la doxorubicine en clinique.

Ces améliorations ont été attribuées à la structure particulière, de type « boucle-train », de ces nanoparticules qui en prolongeant le temps de demi-vie plasmatique de la doxorubicine échappent à la capture massive par les macrophages du foie et de la rate pour se concentrer dans la tumeur.
L'objectif de la thèse a consisté à comprendre les mécanismes régissant la formation de telles nanostructures allongées en utilisant des techniques de caractérisation physico-chimiques (cryo-MET, diffraction des RX, etc) ainsi que de la modélisation moléculaire.

Title : Contribution to physico-chemical studies of squalenoylated nanomedicines for cancer treatment

Keywords : Nanomedicine, Squalene, Doxorubicin, Bioconjugate, Cancer, Drug delivery

Abstract : Previous research in Pr. Patrick Couvreur's team (Institut Galien Paris-Sud) has designed a therapeutic nanomedicine made of doxorubicin chlorhydrate conjugated to squalene, a natural and biocompatible lipid. Compared to free doxorubicin, this nanomedicine presented an increased anticancer activity, a prolonged plasmatic circulation time and a strongly reduced cardiac toxicity, one of the most important limitations of doxorubicin use in clinical studies.
These improvements have been attributed to the

particular "loop-train" elongated structure of these nanoparticles which, by increasing the plasmatic half-life of Dox, may avoid massive uptake by liver and spleen macrophages to accumulate in tumor.
But the mechanism allowing the formation of these elongated structures remained completely unknown, and this has been extensively investigated in the current thesis by using physico-chemical techniques (cryo-TEM, X-ray scattering, etc) as well as molecular modelling.